Characterizing a Quantum Memory Incorporating an Entangled Light Source

Charlotte K. Duda

A thesis submitted for the degree of
Masters of Philosophy of
The Australian National University

September 2019

Declaration

This thesis is an account of research undertaken between March 2017 and October 2018 at the Laser Physics Centre, Research School of Physics and Engineering, The Australian National University, Canberra, Australia.
Except where acknowledged in the customary manner, the material presented in this thesis is, to the best of my knowledge, original and has not been submitted in whole or in part for a degree in any university.

Charlotte K. Duda

September 2019

Acknowledgments

First and foremost, I would like to thank Kate for all the time and energy she put into my project. This work would not have been possible without her experimental expertise and rigorous critique of my thesis. Thank you Matt for maintaining a dialogue with me up until the deadline while remaining calm and patient. I'm very thankful to have worked in an environment where my supervisors remained empathetic and never pushed me to birth a pre-mature body of work. Thank you Rose, Morgan, Jamie, and Matt.B for proofreading my thesis as well as offering some level of necessary emotional support at one time or another. Thanks John, Craig, and Luke for supplying liquid helium and helping me out with technical issues. Lastly, thank you Sweet Bones café for being a constant during my tumultuous living arrangement with the city of Canberra. I appreciate how none of your staff care I exist even though I've been a loyal customer on-and-off for five years.

Abstract

It has been proposed that secure communication over large distances can be achieved using quantum repeater protocols. Two key components which are required for a repeater are an entangled light source and a quantum memory. The approach investigated here, is to use a protocol which incorporates both a memory and entangled light source using rephased amplified spontaneous emission (RASE). To be a viable repeater, RASE must achieve second long storage times, and efficiencies exceeding 90%. The focus of this thesis was to investigate the mechanisms limiting the efficiency of RASE.

In this work, RASE was performed in the rare-earth ion-doped crystal Pr^{3+}:Y_2SiO_5, and the coherence was stored on the ground hyperfine transition for 5 μs. Rare-earth ion-doped crystals are an ideal platform for RASE because they offer long optical and hyperfine coherence times. The hyperfine transitions are of particular interest, because the memory storage times required for repeater can be engineered.

RASE works by inverting an ensemble of two-level atoms to create the optical gain necessary for amplified spontaneous emission (ASE). Detection of ASE heralds the ensemble into a collective state which is entangled with the emitted field. Because the ensemble is inhomogeneously broadened, the collective state will then begin to dephase. The state can be rephased, after a tunable delay time, and the entanglement readout as a second optical field (RASE).

In this work, the metric chosen to confirm entanglement was the inseparability criterion. In previous work, the two emitted fields of light were proven to be entangled with significant confidence, however, the rephasing efficiency was limited to 3% [1]. The explanation for this was a mismatch between the first and second pass of the beam through the crystal, which was the consequence of a retroreflective mirror being positioned incorrectly. In this thesis, the beam mismatch, caused by the position of the mirror, was shown to not affect the RASE experiment. Instead, the RASE experiment is more likely to be affected by a spatial mode mismatch which is caused by the distortion of the control pulses.

The effect of these distortions was observed in the efficiency measurement of RASE. According to the theory, the efficiency of RASE should consistently improve with optical depth. Experimentally, however, in the regime where the two fields were entangled, the efficiency was maximized at 8.3% when the optical depth was 0.8. The performance then began to

deteriorate when the optical depth exceeded 1. This result, therefore, informs how the RASE experiment should be designed in the future. Specifically, care should be taken to correct for the effects of any spatial mode distortions, in order for RASE to operate at the threshold efficiency required for a quantum repeater.

Contents

Chapter 1

Background

1.1 Motivation

Digital cryptography used to be restricted to military and government operations [2] but is now used every day, from securing banking transactions [3] to personal messaging [4]. Cryptographic techniques work by using an encryption algorithm to scramble plaintext unintelligible to an unauthorized person. Although the algorithm is usually widely available, this method remains effective due to the secrecy of a cryptographic key.

A 'key' is a piece of information that is fed into an encryption algorithm to perform the encryption and decryption steps. When both steps are done with the same key, this is called 'symmetric key cryptography' [5]. Ensuring that only authorized persons hold a copy of the key is known as a key distribution problem.

The most straightforward way to distribute a secure key is for two parties to meet in person. However, even then, it would be impossible to know if a copy of the key existed. This dilemma led to the development of asymmetric key cryptography [6], which uses non-identical keys. In asymmetric key cryptography [7] each key performs a unique function, with a widely-disclosed public key used for encryption and an undisclosed private key used for decryption.

Asymmetric key cryptography is effective because working out the private key from a public key is computationally intensive, as the functions used for the encryption algorithm are easy to compute in one direction but challenging in the other. These are known as 'one-way functions', an example of which is finding the large product of two prime numbers versus finding two prime factors of that large number. The cost of this security is that asymmetric key cryptography requires more computational power than symmetric key cryptography. This means asymmetric cryptography is much better suited to securely distributing short symmetric keys, and not lengthy plaintext.

The RSA (Rivest-Shamir-Adleman) is one well-known example of an asymmetric encryption algorithm [8]. One of the earliest descriptions of the RSA appeared in a 1977 issue of the Scientific American, where its presenters posed a 125-digit factorization problem to the public [9]. One co-inventor estimated that factoring the 125-digit number would require at least 40 quadrillion years. In fact, it was cracked 20 years later, in the space of six months, using a distributed network of computers [10]. This scenario illustrates a key challenge in the field of cryptography. To keep up with ever-increasing growth in computer power, larger, more computationally expensive asymmetric keys are required to distribute short symmetric keys.

In contrast, the field of quantum cryptography offers cryptographic keys which are provably secure by the laws of nature, and immune to the growth in computer power. Unlike the classical analog, when information is encoded onto a quantum object, or 'qubit', any measurement of the object will alter it irreversibly (see §1.2). If a sequence of qubits is exchanged, any interception will manifest as errors in the sequence. A secure key is then created in the absence of errors and can be used to encrypt plain text over an insecure channel. Conventional cryptographic algorithms can be used with quantum keys, and therefore quantum cryptography is better described as 'quantum key distribution' (see §1.3).

There is a strong motivation to use telecom-compatible photons as qubits to leverage existing fiber technology. However, bound by the no-cloning theorem of quantum mechanics, standard amplification techniques cannot be used to overcome telecommunication loss for a quantum signal. This limits the direct distribution range of quantum keys to intracity distances on the order of hundreds of kilometers. To fully leverage this technology, the key range should extend to distances on the order of thousands of kilometers, connecting isolated cities. One way to achieve this is with a repeater protocol, which breaks up a usually intransmissible distance into a series of shorter, low-loss links (see §1.5). The photon can then be teleported across these links using the quantum mechanical property of entanglement [11]. This approach is successful because the time taken to communicate scales much better than for direct transmission.

The simplest case of a quantum repeater requires two components: an entangled photon pair source, and a quantum memory, which are both outlined in §1.4. This thesis evaluates a repeater protocol which integrates these two components using rephased amplified spontaneous emission (RASE) [12]. This integrated approach makes RASE an ideal test-bed for the refinement and demonstration of quantum repeater technology.

1.2 Harnessing the Quantum Properties of Light

Quantum mechanics offers a unique set of tools which allow the creation and distribution of a provably secure cryptographic key. The security is a product of the statistical nature of quantum objects. This nature can be described by the object's wave-function ψ, whose time evolution is given by the Schrödinger equation. The linearity of this equation means the sum of multiple quantum states can create an equally valid quantum state, a superposition of states. For example, using Dirac notation, a quantum superposition state $|\psi\rangle$ of two basis states $|0\rangle$ and $|1\rangle$ can be written

$$|\psi\rangle = a|0\rangle + b|1\rangle, \tag{1.1}$$

where a and b are coefficients of the two basis states. Unlike with classical mechanics, when an observable of state $|\psi\rangle$ is measured, the state will be destroyed. The observed state can either be $|0\rangle$ or $|1\rangle$, and the probability of observing these are $|a|^2$ and $|b|^2$ respectively. This measurement is irreversible and, therefore, any interception of a key based on a quantum object will be perceptible.

Another property at the heart of quantum mechanics is entanglement. This is when a superposition state extends over two or more objects. In this case, measurement of one object will influence the other, even when the two are spatially separated. Therefore, observables of entangled objects are found to be correlated.

Entanglement can easily be considered one of the stranger aspects of quantum mechanics. In fact, early observations of quantum entanglement lead to great concern as to whether our interpretation of quantum mechanics was complete. In 1935 the EPR (Einstein-Podolsky-Rosen) paradox [13] was proposed, which suggested that some hidden parameters were missing from the description. It wasn't until 29 years later, that John S. Bell reasoned that the predictions of quantum mechanics could not be due to any theory of local hidden variables [14]. This lead to the development of Bell tests to experimentally confirm this, with loophole free Bell tests being performed very recently [15]. These recent results seem to suggest that entanglement is, in fact, a fundamental aspect of quantum mechanics. This fundamental property of quantum mechanics is exactly what allows a quantum key to be distributed over distances which would usually intransmissible.

1.3 How to Distribute a Quantum Key

Several protocols have been proposed to create and distribute quantum keys [16, 17, 18]. The first was the BB84 protocol, named after its founders Charles Bennett and Giles Brassard [16]. This led to the first experimental demonstration of a distributed quantum key in 1992, performed by its inventors, where the key was distributed over 30 cm of air [19]. That same year, the protocol was also performed over 1 km of optical fiber in Geneva [20].

1.3.1 The BB84 Protocol

In the BB84 protocol information is encoded in the polarization of a single photon of light, creating a qubit, which is analogous to a classical bit of information. The individual photons are then distributed to remote parties via a quantum channel, which could be free-space or an optical fiber. The sender and receiver use four polarization states which create two bases, for example, horizontal/vertical and -45°/+45°. Each polarization translates to a bit-value, for instance, horizontal and -45° could translate to a 1-bit value, while vertical and +45° could translate to a 0-bit value.

The protocol can be outlined with the classical archetypes Alice, the sender; and Bob, the receiver. Alice sends a photon whose polarization is randomly selected, and recorded by her. Bob then randomly selects one of two bases to measure the photon in and records his results. Alice and Bob then communicate the sequence of bases they used over a classical channel. Measurements performed with different bases are then discarded, creating a sifted key.

In the absence of any interference along the quantum channel, Alice's and Bob's sifted key should be identical. This is confirmed by communicating a small subset of their results over a classical channel. If no errors are identified, the undisclosed measurements can be used as Alice and Bob's private key. On the other hand, if errors are present then the key may of been intercepted. In this way, a provably secure key can be distributed using the properties of quantum mechanics. For a more detailed discussion of the BB84 protocol see review [21].

1.3.2 The Reality of Direct Transmission

Since the proposal of the original BB84 protocol, quantum key distribution technologies are now commercially available, being offered by companies such as ID Quantique and QuintessenceLabs. However, the range the technology can operate over is severely limited, with 307 km being the largest experimentally verified distance in fiber [22]. Even in the low-loss C-band, used in telecommunication, a loss of 0.2 dB/km becomes significant over large distances. For example, a single photon source with a 10 GHz repetition rate will successfully transmit a photon through 10,000 km of fiber at a rate of 1 Hz; which is one photon every 300 years [23].

Quantum repeater protocols are used to distribute a quantum key over distances which are usually intransmissible with direct transmission (see §1.5) . They work by breaking up the total transmission line into a series of short links of low-loss, connected together at nodes of the repeater. The key is then incrementally distributed between adjacent nodes using entanglement operations until the two ends of the transmission line have been connected. The goal of the procedure is to preserve the non-classical nature of the photon for the entirety of the distribution process.

In order for the repeater to maintain the non-classical nature of the photon, the most simplistic approach requires two components: a source and memory. Because integrating these components has proven challenging, an intermediate solution called a 'trusted node network' has been developed. This approach has had high profile success, but sacrifices the security of the key.

1.3.3 Trusted Node Networks

Trusted node networks use classical techniques to overcome the issue of transmission loss and extend the distribution range of a 'pseudo-quantum' key. The protocol is performed with a similar infrastructure to a quantum repeater, breaking a large, high-loss distance into a series of short, low-loss links. Storage and amplification of the key occurs at points connecting the links, called 'trusted nodes'. The key can then be transmitted over the complete transmission line by each node creating a cryptographic key with the previous node, and the next node along the way. This daisy-chaining of keys allows an extension of the range a quantum key can be transmitted over, beyond what is possible with direct transmission.

Distribution of a quantum key with a trusted node network has been performed both terrestrially [24, 25] and in low-earth orbit. For the latter case, the satellite performs the role of the repeater node, transmitting to the first ground station when passing over, then re-transmitted when passing over the second ground station. Great success has been demonstrated with this method. The Chinese satellite, Micius, for example, was used to distribute pseudo-quantum keys between locations separated by 7,600 km [26].

The Micius satellite is one example of how a pseudo-quantum key can be created between locations separated by large distances, otherwise intransmissible with direct transmission. However, the security of the key is compromised to achieve the increased range. In the distribution phase, the cryptographic key is treated non-classically, the same as for a quantum repeater. However, within each network node the key is stored classically.

Unlike a quantum repeater, any interception during the storage phase will not manifest as detectable errors in the final key. This means that at each node the key is vulnerable to undetectable interception, hence a certain level of *trust* is associated with the network's use.

A truly secure quantum repeater network can only exist if the intermediate nodes maintain the non-classical nature of the key. In the simplest case, this requires an entangled photon pair source and quantum memory at each repeater node [27, 28].

1.4 The Components of a Quantum Repeater

A quantum repeater network will be able to distribute a purely quantum key over a large distance of high-loss by breaking it up into a series of smaller links of low loss. Nodes which preserve the non-classical nature of the key connect these links and allow the key to incrementally distributed across the complete transmission line.

1.4.1 An Entangled Photon Pair Source

An ideal single photon source would be deterministic, or on-demand, and have zero probability of multi-photon emissions. If the probability of multi-photon emissions is non-zero the security of the key may be comprised through a photon-number-splitting attack [29, 30]. In reality, it's very difficult to create single photons deterministically.

Single emitters in cavities have been shown to perform well as deterministic single photon sources, achieving efficiencies as high as 60% [31]. Another solution is to trigger photon pairs probabilistically, one photon can then be used to herald the presence of the other.

Spontaneous parametric down-conversion (SPDC) [32] takes this approach, illustrated in Figure 1.1. SPDC creates an entangled photon pair by starting with a single pump photon. The pump photon is then converted to a pair of lower energy photons, called the signal and idler, with a $\chi^{(2)}$ non-linear process. For quantum information purposes, however, the probability of creating a pair of photons using SPDC is typically lower than 1%, to reduce the likelihood of creating multiple photon pairs.

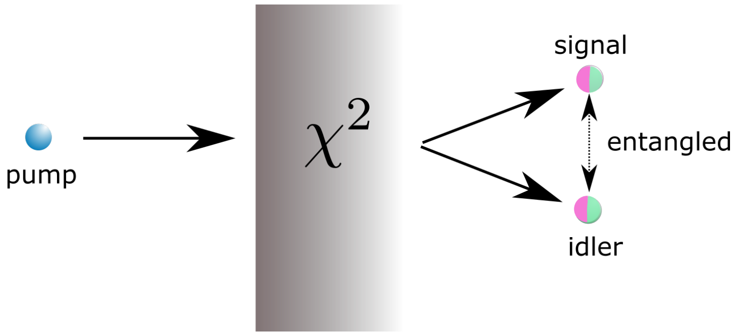

Figure 1.1: Illustration of spontaneous parametric down conversion (SPDC), where an entangled signal and idler photon pair is created from a single pump photon interacting with a non-linear $\chi^{(2)}$ medium.

Atomic ensembles can also be used in a similar way to generate entangled photon pairs. One such protocol is the Duan-Lukin-Cirac-Zoller (DLCZ) protocol, which was first proposed by Duan *et al.* in 2001 [33]. It has been heavily developed and improved upon since then [34, 35, 36, 37], but the simplest version uses two metastable ground states, $|g_1\rangle$ and $|g_2\rangle$, and an excited state $|e\rangle$.

In the DLCZ protocol an atomic ensemble of N atoms is prepared in $|g_1\rangle$, shown in Figure 1.2. A short write pulse is (usually) applied off-resonant to the $|g_1\rangle \leftrightarrow |e\rangle$ transition. This drives a single atom into the second ground state $|g_2\rangle$ with some small probability.

In this Raman-scattering process a single Stokes photon is emitted. Detection of the Stokes photon in the far field heralds the state of the ensemble with exactly one quanta of excitation in state $|g_2\rangle$. Since no information is known about which atom emitted, the state of the ensemble becomes a superposition of any atom having emitted. This is an example of 'entanglement-via-indistinguishability. The superposition state contains N-1 atoms in the first ground state $|g_1\rangle$ and 1 atom in the second ground state $|g_2\rangle$, written as

$$|\psi\rangle = \frac{1}{\sqrt{N}}\sum_{j=1}^{N} e^{i(\mathbf{k}_w - \mathbf{k}_s)\mathbf{x}_j} |g1_1, g1_2, ...g2_j, ...g1_N\rangle, \tag{1.2}$$

where $\mathbf{k}$ is the wavevector, with the subscript w denoting the write pulse and s referring to the Stokes photon, and $\mathbf{x}_j$ corresponds to the position of the j^{th} atom in the ensemble.

The collective excitation can then be read out by applying a resonant read pulse on the $|g_2\rangle \leftrightarrow |e\rangle$ transition. The state of the ensemble then collectively decays back into the ground state $|g_1\rangle$, emitting an anti-Stokes photon. The direction of the anti-Stokes photon will be uniquely correlated with the Stokes photon when the phase matching condition

$$\mathbf{k}_w - \mathbf{k}_s = \mathbf{k}_r - \mathbf{k}_a \tag{1.3}$$

is satisfied, where the wavevector subscript a denotes the anti-Stokes photon and r refers to the read pulse.

Altogether, the DLCZ scheme can be used to generate two time-separated entangled photons, where the second is recalled deterministically with a read pulse. This is in contrast to SPDC where the two entangled photons are generated simultaneously, and the detection of one heralds the presence of the other.

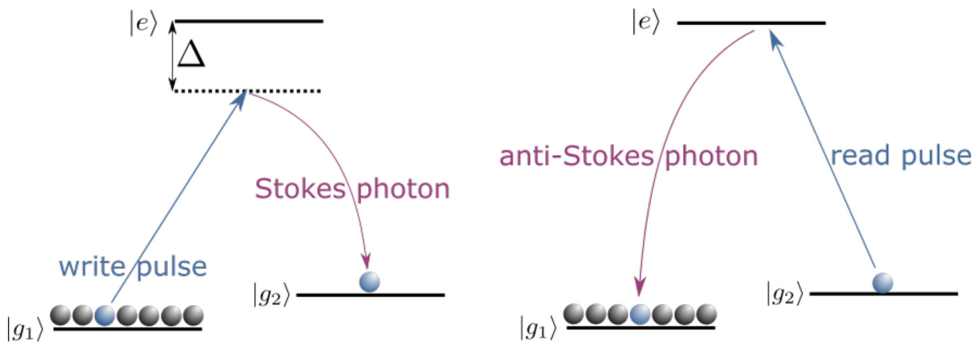

Figure 1.2: Illustration of the DLCZ protocol, where a write pulse is applied off-resonantly with the $|g_1\rangle \leftrightarrow |e\rangle$ transition, and leads to the emission of a Stokes photon. Applying a read pulse which is on-resonant with the $|g_2\rangle \leftrightarrow |e\rangle$ transition generates an anti-Stokes which is entangled with the Stokes photon.

1.4.2 A Quantum Memory

A quantum memory is capable of storing an arbitrary quantum state and recalling it after a programmable length of time without altering the state in any way. However, as a result of the no-cloning theorem, a quantum memory cannot operate in the same way as a classical memory, where the input state is copied. This means a quantum memory can only produce a perfect copy of the input state if the original input state is destroyed. Therefore, a photon can only be stored by reversibly mapping its properties onto a material.

Quantum states have been stored and recalled in single atoms [38] and atomic ensembles [39], with their quantum properties preserved throughout the process. In general, greater efficiencies can be achieved using an ensemble of atoms [23].

There are many memory protocols outlining how photons can be reversibly mapped onto ensembles [40]. These include, but are not limited to, electromagnetically induced transparency (EIT) [41], gradient echo memories (GEM) [42] , atomic frequency combs (AFC) [43], hybrid photon echo rephasing (HYPER) [44] and revival of silenced echo (ROSE) [45]. The memory protocol investigated in this work is rephased amplified spontaneous emission (RASE), outlined in Chapter 3.

1.4.3 Integrating the Components of a Quantum Repeater

A heralded single photon source such as SPDC could be made deterministic by storing one photon in an external memory. The detection of the other photon would then herald that the memory is loaded, and the stored photon could be recalled later, on demand.

This approach requires the single photon to have the same wavelength and bandwidth as the memory, which presents a significant challenge. Standard down converted photons have bandwidths on the order of hundreds of gigahertz, while atomic memories have a storage bandwidth on the order of megahertz. Cavity enhanced SPDC has been used to sufficiently reduce the photon bandwidth, and store signal photons in external memories [46]. However, this adds another layer of complexity to the repeater protocol.

A promising alternative is to use a DLCZ style system, which builds a memory into an entangled photon pair source, such that they are intrinsically compatible. This approach provides a simplistic framework for the development of a quantum repeater.

1.5 A Quantum Repeater

For a quantum key to be useful it must be distributed over large distances. This is a challenge because standard telecommunication techniques cannot be used to amplify quantum signals as a consequence of the no-cloning theorem. For direct transmission, the communication rate decays exponentially with distance because of loss, severely limiting the key distribution range [47].

One solution is to break up the total transmission line into a series of shorter links of distance L_0, where the probability of transmission across each link has significantly increased. Trusted node networks use this approach but store the key classically at each repeater node, compromising its security. A quantum repeater maintains the non-classical nature of the key at every stage, ensuring the provable security of the final key. This is accomplished by having an entangled photon pair source and quantum memory at each node of the repeater.

1.5.1 Single Mode

The concept of a quantum repeater was proposed by Briegel *et al.* in 1998 [48], and outlined how quantum entanglement could be used as a resource to distribute a single quantum of information over a typically intransmissible distance. The first step in the protocol is entanglement generation, shown in Figure 1.3 (a). This step begins by simultaneously triggering the entangled photon pair source of two neighboring nodes, which creates entanglement between them.

An emission event from the source is a probabilistic process, where the likelihood of either source emitting is small, and both emitting is negligible. When one source does emit one photon of the pair is sent to a 50/50 beamsplitter placed between the nodes, while the other is sent to the local quantum memory and stored. Detection of a single photon after the beamsplitter, therefore, means that its partner is stored in the memory.

The detected photon is measured 'at a distance' such that the origin of the photon is unknown [49, 50]. A detector click, therefore, communicates that either source A or B has emitted. As the origin of the photon is unknown, so is the location of its partner, and the stored photon could just as likely be contained in memory A as in memory B. This means a single quantum of excitation is now distributed across both memories, leaving them 'entangled-via-indistinguishability'. At this point, the state of the system can be written as

$$|\psi_{AB}\rangle = \frac{1}{\sqrt{2}}(|1_A\rangle|0_B\rangle + |0_A\rangle|1_B\rangle e^{i\phi_{AB}}), \tag{1.4}$$

where $|1_N\rangle$ and $|0_N\rangle$ correspond to one photon and zero photons, respectively, stored in node N, and ϕ_{AB} is a phase factor that takes into account a difference in transmission distance.

As the probability of source emission is very low, the two sources must be repeatedly triggered until a detector click is observed, heralding when entanglement has successfully been generated. This means that the entanglement generation step is the most time consuming stage in the quantum repeater protocol. The local memory at each node is required to maintain entanglement, until, with time, entanglement has been created between other node pairs. The second step of the protocol, entanglement swapping [51], can then proceed.

The entanglement swapping step acts to distribute entanglement between non-neighboring repeater nodes. This is illustrated with the two entangled node pairs A-B and C-D in Figure 1.3 (b). The step is performed by simultaneously triggering local memories of nodes B and C to read-out. If a photon is held in either memory this read-out step will send it to the detector.

Whether this step is successful depends on what is stored in the memories of nodes B and C. There are three possible outcomes: zero, one, or two photons are detected. If the outcome is zero or two photons, the step is unsuccessful and entanglement generation must be repeated. If only a single photon is detected the step is successful, because one photon must still present in memory of either node A or D. This photon could just as likely be in either A or D because no information is known about whether memory B or C emitted. This leaves the two non-neighboring memories entangled-via-indistinguishability, with a single quantum of excitation distributed between them.

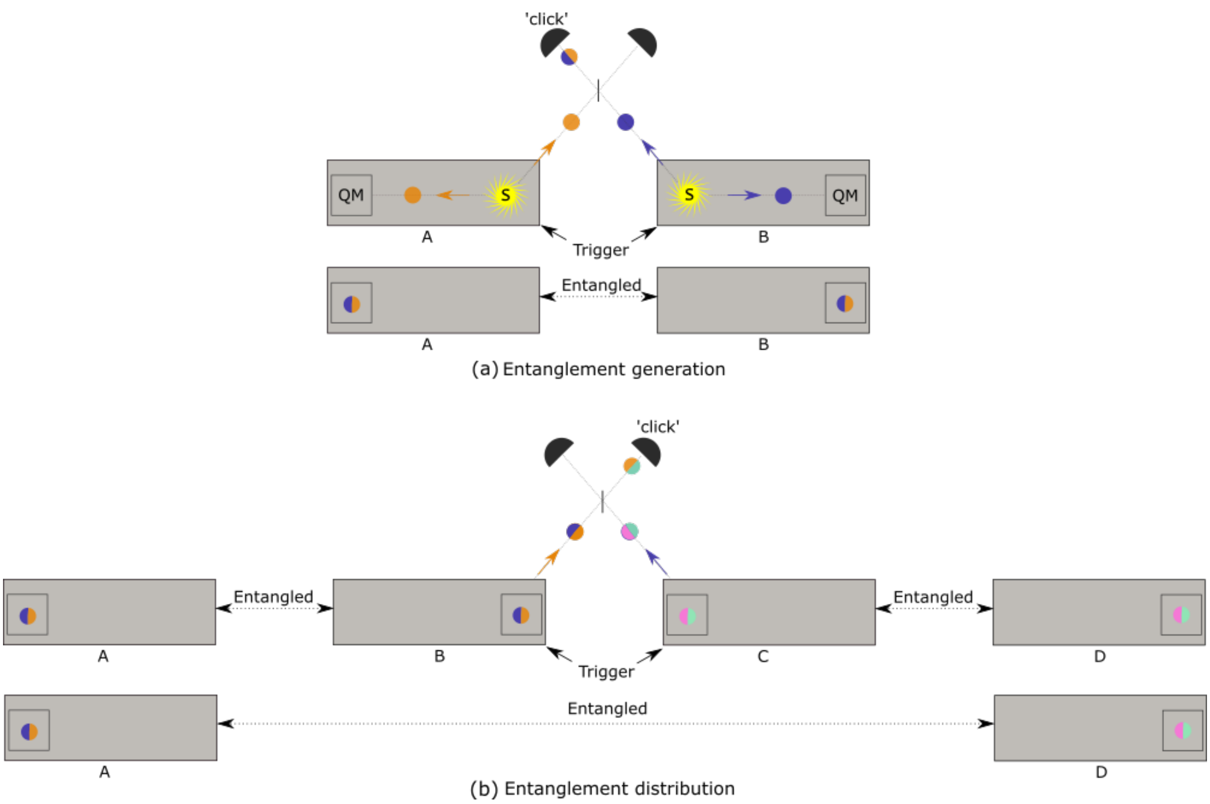

Figure 1.3: A possible quantum repeater protocol where each node contains an entangled photon pair source (S) and quantum memory (QM). (a) The photon pair sources of neighboring nodes, A and B, are triggered. This sends one photon to the local memory, for storage, and the other to be measured. The detection of a photon heralds that either memory A or B is loaded. Because the origin of the photon is unknown, the stored quantum is shared between both memories and an entangled state is created. (b) The memories of neighboring nodes B and C are simultaneously triggered, sending the emitted photons to be measured. The origin of the detected photon is again, unknown, distributing the entanglement across non-neighboring nodes A and D.

By performing further entanglement swapping steps the distribution range of the quantum of information can be extended even further, eventually connecting the two end nodes of the total transmission line.

Altogether, a quantum repeater protocol like this is a powerful means of distributing quantum information. This is because the time taken to establish entanglement scales polynomially with distance. In the case of long transmission distances, using direct transmission the time required to establish a key scales exponentially with distance [52].

1.5.2 Multimode

The entanglement generation step in the repeater protocol is probabilistic and requires a single photon to be detected to herald when entanglement has been generated between neighboring memories. With a single mode repeater, illustrated in Figure 1.3, the low transmission rate means the probability of successful entanglement P_0 is low. After each trigger, a wait time of $\frac{L_0}{c}$ exists before the measurement outcome is known. This is approximately the time it takes for the photon to travel to the beamsplitter, plus the time it takes for the result to be communicated back to the memory. Therefore, a large amount of time is spent on trial and error entanglement.

The success probability of the entanglement generating step can be increased using a multimode repeater. A temporally multimode repeater is illustrated in Figure 1.4 (a), however, repeaters can also be spectrally [53] and spatially [54] multimode. A photon pair source with a repetition rate much higher than $\frac{c}{L_0}$ is triggered such that N-photon pairs are emitted from each source in the wait time. This increases the probability of successful entanglement by NP_0 [55].

In part *a* the m^{th} photon is successfully detected, indicating that its partner was stored in either memory A or B. In order for the m^{th} photon to be retrievable, the memory must also be multi-mode. This requires that the local memory can recall N-photons while preserving their distinguishability.

In part (b) nodes C and D were successfully entangled with the detection of a different temporal mode, corresponding to the n^{th} photon. Therefore, the entanglement swapping step requires the m^{th} mode of B and the n^{th} mode of C must be recalled simultaneously.

Altogether, the total distribution time for a single mode repeater t_0, can be reduced to $\frac{t_0}{N}$ with multiplexing [23].

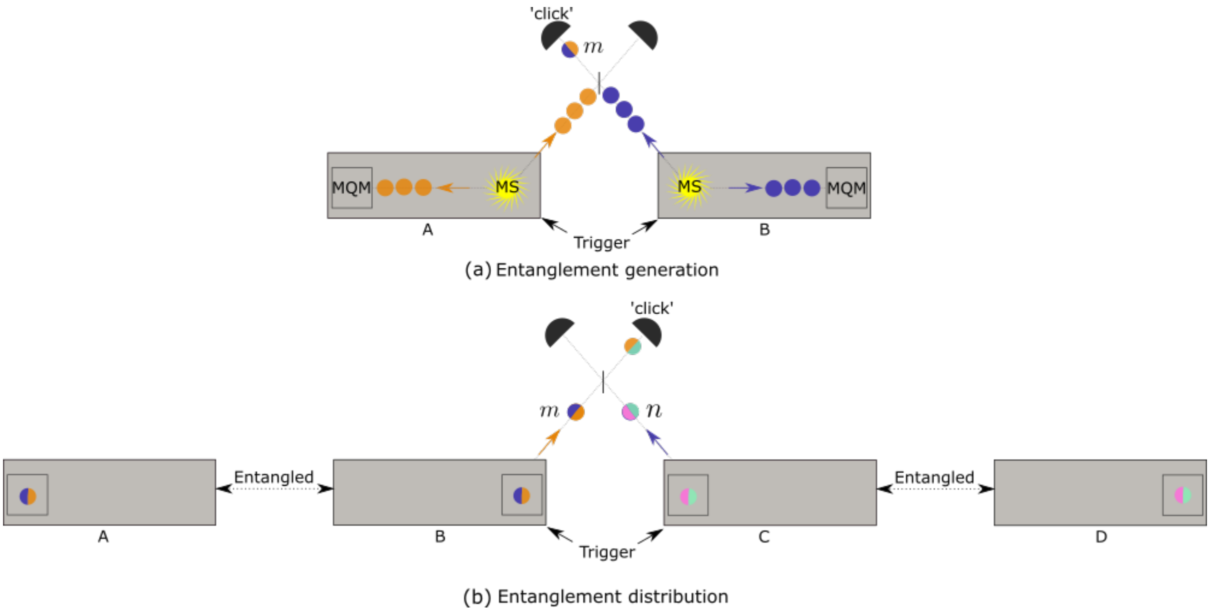

Figure 1.4: Illustration of a temporally multimode quantum repeater, where each node has an multimode entangled pair source (MS) and multimode quantum memory (MQM). (a) Neighboring node sources are repetitively triggered at a rate higher than $\frac{c}{L_0}$ sending N-photon pairs to the local memory of each node and to the detector to be measured. If the m^{th} photon is successfully detected, the other photon of the pair is stored in either A or B. (b) Entanglement swapping must then simultaneously recall different successful modes from neighboring links.

1.6 Progress to Date

Specific performance requirements must be met for order a practical quantum repeater to be built. Firstly, the memory component must interface with the current fiber network. The simplest way to achieve this is using an integrated source-memory protocol which operates in one of the low-loss telecom bands for optical fibre at 1,310 and 1,550 nm. This thesis evaluates an integrated source-memory protocol, which can operate as a single node of a repeater, called rephased amplified spontaneous emission (RASE) [12]. The protocol is performed in the rare-earth ion-doped crystal praseodymium-doped yttrium orthosilicate using techniques which are transferable to a telecom compatible erbium-doped crystal [56].

In addition to being telecom compatible, a useful memory must also operate with storage times comparable to the current global telecommunication time, which is 70 ms. Rare-earth systems have great potential for quantum communication because long storage times can be achieved when a coherent state is stored on the long-lived hyperfine transitions. Milos *et al.* recently demonstrated one second long coherence times in a telecom-compatible erbium-doped crystal [56]. Even longer coherence times are possible using magnetic field techniques such as zero first order Zeeman (ZEFOZ) shift, where hyperfine coherence times as long as six hours have been demonstrated in a europium-doped crystal [57]. Another approach, which should be mentioned, is to store and recall a quantum state using a delay line, i.e. the storage time has been pre-programmed. A delay line which uses fast switching inside a loop is similar to a memory, however, a large amount of loss limits the storage time to nanoseconds [58, 59].

To achieve the high-data rates required to distribute a quantum key, an integrated memory-source protocol, like RASE, must meet several other requirements. Firstly, the memory must create and store information efficiently. The efficiency requirement of the memory is typically considered greater than 90%, where this value accounts for all sources of loss including memory inefficiencies, fiber-coupling losses and detector inefficiencies [23]. At present, efficiencies as high as 69% have been demonstrated using the optical transitions of a praseodymium-doped quantum memory [60] and detectors efficiencies have been demonstrated as high as 95% [61]. Lastly, both the source and memory must be multimode to reduce the time spent on trial and error entanglement and, therefore, the demands on storage time.

Recently, significant progress has been made towards meeting the above requirements using several different source-memory protocol approaches, performed in either a praseodymium or europium-doped crystal. Ferguson *et al.* preserved two modes with perfect distinguishability using the RASE protocol, while incorporating storage on a hyperfine transition for 5 μs [1]. One of the benefits of RASE is that it is easy to multiplex temporally because it is based on photon echo rephasing techniques. In comparison, the standard DLCZ protocol is more difficult to multiplex. One solution is to use a DLCZ-AFC type system. Using this approach, Laplane *et al.* demonstrated the storage of 12 modes while incorporating hyperfine storage for 1 ms [62]. Similarly, Seri *et al.* demonstrated a telecom-compatible memory which stored 7 modes with a 25 μs hyperfine storage time [63]. However, for both RASE and DLCZ-AFC the efficiency of the memory has been limited to roughly a percent. Significant progress has also been demonstrated using DLCZ-GEM [39] and GEM [64] memory protocols but they have not been demonstrated in rare-earth systems.

The significant advantage RASE has over DLCZ-type systems is that it is expected to be highly efficient [65]. However, this was not observed in the work of Ferguson *et al.*, where the efficiency was limited to 3%. The primary goal of this thesis was to investigate why the efficiency of RASE is much lower than expected.

Chapter 2

The Pr:YSO Crystal and Photon Echo Techniques

The rare earths are a group of metals consisting of the 17 lanthanides as well as scandium and yttrium, that have unique magnetic, chemical and luminescent properties. These properties make them natural building blocks for many exciting emerging technologies. The clean energy sector, for example, is heavily dependent on rare earth alloys, which can behave as strong permanent magnets, used in electric vehicles and wind turbines [66]. In communication rare-earth *ions* are of interest because of their unique luminescent properties. Erbium, for example, conveniently emits in the the low-loss 1550 nm fiber telecom band.

Rare-earth ions are also of great use in quantum communication, as quantum memories of light, when doped into a crystal host. Their key feature is the ability to store information for the times scales required for large scale quantum networks (see §2.2).

This chapter outlines the rare-earth ion-doped crystal used in this work, which was trivalent praseodymium doped yttrium orthosilicate, Pr^{3+}:Y_2SiO_5 or Pr:YSO. The optical and hyperfine transitions of interest for Pr:YSO are introduced in §2.1, followed by a discussion of the broadening mechanisms which influence them in §2.2. The spectroscopic techniques used to prepare rare-earth ion crystals for information storage are outlined in §2.3, and the optical echo techniques which allow information storage and recall in §2.4.

2.1 Spectral Properties

Long storage times are possible using rare-earth ion-doped crystals because of the relatively quiet environment offered by the material. Rare-earth ions in solids typically exist in a 3+ oxidation state, with an electronic configuration of [Kr]$4d^{10}5s^{2}5p^{6}4f^{n}$, where n ranges from 0 to 14. The unique properties of rare-earth ions can be attributed to the localized behavior of their optically active 4*f* electrons. The partially filled 4*f* subshell lies closer to the atomic nucleus than the 5*s* and 5*p* subshells, illustrated in Figure 2.1. These surrounding subshells behave as an effective Faraday cage, shielding the rare-earth ion's active electrons from the crystal environment. Insensitivity to the host environment means the energy spectra in solid state is close to that of a free ion. This greatly simplifies the Hamiltonian of the solid state rare-earth ion, where interactions from the host crystal can be treated as a perturbation to the free rare-earth ion Hamiltonian.

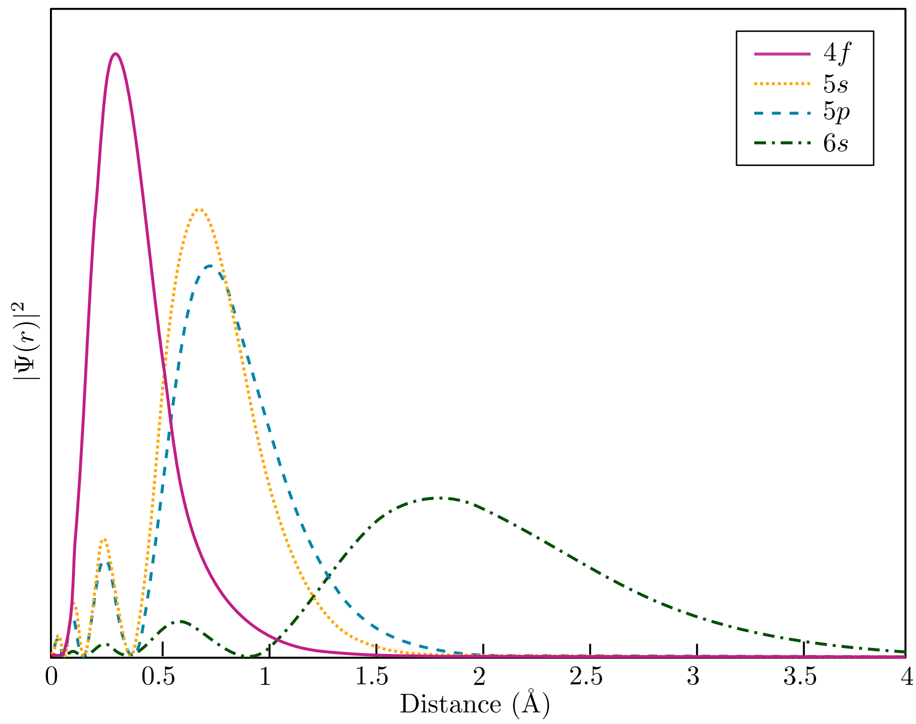

Figure 2.1: Radial distribution of the outer orbitals of Gd^+, reproduced from [67], originally from [68].

The free ion Hamiltonian is constructed from a series of interactions. When only the central part of the Coulomb repulsive force is considered all *n*=4 energy levels are degenerate. Beyond this central field approximation the orbital degeneracy is lifted, resolving the *n*=4 subshells. The degeneracy in the *f* subshell is then further lifted by the spin-orbit interaction. This mixes states with different spin angular momentum S and orbital angular momentum L but the same total angular momentum J = L + S. Because of this mixing L and S no longer suffice as good quantum numbers, and the (2J + 1)-degenerate free ion multiplets are labeled with Russell-Saunders symbols of the form $^{2S+1}L_J$.

Interactions with the host crystal are treated as perturbations on the free-ion structure, either partially or wholly lifting the (2J + 1) degeneracy. In the case of Pr:YSO the degeneracy is fully lifted, resolving electronic singlet states separated by $\sim$ 10 THz [69]. This is known as the *crystal field* structure, and is shown in Figure 2.2.

The transition from the lowest $^3H_4$ electronic singlet state to the lowest $^1D_2$ electronic singlet state is utilized in this work. This is because the optical lifetime of the excited states is inversely proportional to the sum of the radiative and non-radiative decay rates. For quantum devices we require the lifetime to be extended out as long as possible, meaning the the non-radiative component must be minimized. This component is most significant when the energy gap between the levels is small, and therefore, the transition from the lowest crystal field multiplet is selected.

The frequency of the $^3H_4 \rightarrow^1 D_2$ transition depends on the crystal structure. This transition is weakly allowed due to the low symmetry of the site occupied by the Pr^{3+} ions. In Pr:YSO the Pr^{3+} ions substitute for Y^{3+} ions, which occupy one of two crystallographic sites, both with C_1 (no) symmetry, called site 1 and site 2 [69]. It has been observed that site 1 is occupied with significant preference [70], and therefore the only site considered in this work. For site 1 the $^3H_4 \rightarrow^1 D_2$ transition occurs at λ =605.977 nm in vacuum.

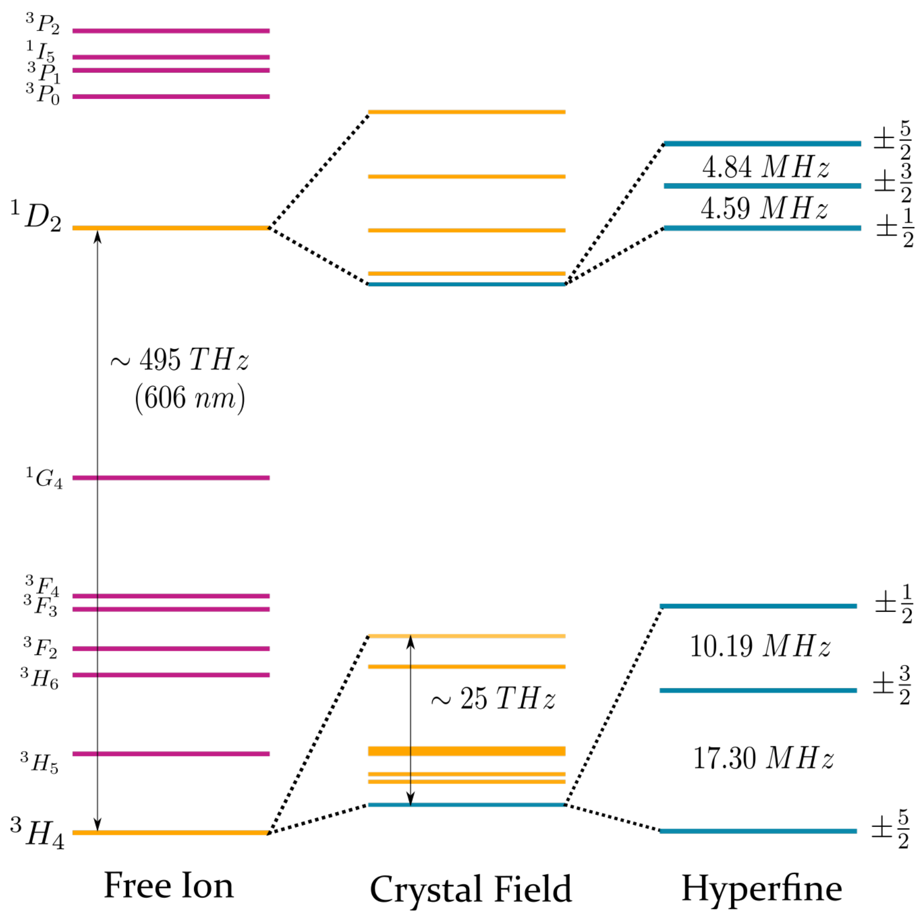

Figure 2.2: Energy levels of the free-ion, crystal field and hyperfine structure at zero magnetic field in the 4f electrons in Pr:YSO. The relative spacings of the free-ion levels calculated from [71]. The crystal field and hyperfine splittings were measured in [69]. The hyperfine ordering was given in [72], where the hyperfine levels are labeled with the dominant spin quantum number m_s.

These electronic states are then further split by a combination of nuclear and magnetic interactions. For Pr^{3+} with a nuclear spin of I = 5/2, three doubly degenerate hyperfine states are created for both the ground $^3H_4$ and ground $^1D_2$ electronic singlet states in zero magnetic field. The hyperfine levels are split on the order of 10 MHz [70], and labeled with the dominant spin quantum number m_s=$\pm\frac{1}{2}$, $\pm\frac{3}{2}$ and $\pm\frac{5}{2}$. The degeneracy of these levels can be lifted by applying an external magnetic field.

For the case of Pr:YSO, the hyperfine levels cannot be described by a pure spin quantum number as the m_s eigenstates are slightly mixed by the crystal field. This mixing means that transitions that are not like-to-like are weakly allowed, and in total nine optical transitions can occur for Pr:YSO at zero magnetic field. The strength of mixing determines the relative oscillator strength of the optical transitions, which describes the probability of absorption or emission, and is summarized in Table 2.1. This table shows mixing is largest between $\pm\frac{1}{2}$ and $\pm\frac{3}{2}$ (highlighted in orange), while transitions $\pm\frac{5}{2}$ are preferentially like-to-like (highlighted in pink).

		$^1D_2$		
		$\pm\frac{1}{2}$	$\pm\frac{3}{2}$	$\pm\frac{5}{2}$
	$\pm\frac{1}{2}$	0.55	0.38	0.07
$^3H_4$	$\pm\frac{3}{2}$	0.40	0.60	0.01
	$\pm\frac{5}{2}$	0.05	0.02	0.93

Table 2.1: The relative oscillator strengths of Pr:YSO optical transitions between the ground $^3H_4$ and excited $^1D_2$ electronic singlet states in zero magnetic field. Transitions with the largest mixing are highlighted in orange, while the preferentially like-to-like transition is highlighted in pink. All values have an uncertainty of ± 0.01. [72]

These oscillator strengths had to be considered in the development of the repeater protocol investigated in this work, the rephased amplified spontaneous emission scheme. The aim of this thesis was to replicate the results seen by Ferguson [73], in which, transitions with similar oscillator strengths were selected. However, the recall efficiency can be maximized by working on transitions with different oscillator strengths in different parts of the protocol [65, 74]

2.2 Broadening Mechanisms

The precisely defined transitions shown in Figure 2.2 will be broadened by dynamic and static mechanisms which occur inside the crystal. 'Homogeneous' broadening describes the broadening of a single ion, while 'inhomogeneous' broadening describes the broadening of an ensemble.

2.2.1 Homogeneous Linewidth

The broadening of a transition for an individual ion is described by the homogeneous linewidth Γ_h. How long a quantum state can be preserved for is characterized by the 'coherence time' T_2, which is related to the homogeneous linewidth by

$$\Gamma_h = \frac{1}{\pi T_2} = \frac{1}{2\pi T_1} + \Gamma_\phi, \tag{2.1}$$

where T_1 is the transition lifetime and Γ_ϕ describes contributions from pure dephasing processes. The upper limit on T_2 is when $T_2 = 2T_1$. This is called the lifetime limit, however, because of the Γ_ϕ term the observed T_2 is usually much smaller. The primary mechanisms that influence Γ_ϕ are interactions with other rare-earth ions and ions of the host crystal.

At room temperature phonon coupling is the dominant contributor to the homogeneous linewidth. In Pr:YSO these vibronic interactions become negligible when the sample is cooled close to 4 K, which is the temperature regime used in these experiments.

Instantaneous spectral diffusion (ISD) is another source of dephasing in Pr:YSO, and occurs between rare-earth ions. In Pr^{3+} doped crystals the dominant source of ISD is non-equilibrium phonons [75, 76]. These phonons are resonant with neighboring ion transitions, and upon absorption lead to dephasing. Therefore, ISD is reduced to a manageable level in this work, compared to other sources of decoherence, using a low concentration of dopant ions.

Once ISD is controlled, the dominant contributor to Γ_ϕ becomes a magnetic dipolar interaction. This occurs between the dopant and the nuclear-spin flips of the host ions, and can be minimized by selecting a host crystal that offers a relatively quiet magnetic environment. For the YSO crystal used in this work, yttrium ions possess the dominant magnetic moment. The magnetic dipole moment is small, -0.13 μ_N [70], where μ_N is the nuclear magneton, but enough to cause a constant exchange of yttrium nuclear spins. This produces a dynamic magnetic field which modulates the optical transition frequency of the dopant and contributes to dephasing.

Selecting a dopant ion with a larger magnetic moment than the host will act to detune the dynamic yttrium ions, reducing the rate of spin exchange in the host. The Pr^{3+} dopant used in this work has a magnetic moment of 4.3 μ_N [77], which creates a small local magnetic field where the dynamic action of the yttrium ions is frozen.

The magnetic dipole interaction will affect both the hyperfine and optical coherence times, but the effects are different. This is because of a sizable difference in transition lifetimes. The lifetime of the optical transition is 164 μs for a dopant concentration of 0.02% at 1.4 K [69], while the lifetime of the hyperfine transitions is 200 s for a dopant concentration of 0.1% at 1.6 K [78]. These values place a fundamental limit on the coherence times which can be achieved with the material, as outlined by Eq. (2.1).

For the optical transition, the magnetic dipole contributions to the dephasing term Γ_ϕ are negligible when compared to the lifetime term. Therefore, the optical coherence times can approach the lifetime limit, being observed as long as 193 μs for a dopant concentration of 0.1% in zero magnetic field at 1.7 K [79]. The hyperfine coherence times, on the other hand, are far from the lifetime limit. This is because the contribution from Γ_ϕ dominates over the lifetime term, resulting in a measured hyperfine coherence time of 0.5 ms for a dopant concentration of 0.05% in zero magnetic field at 5 K [80].

The coherence times attainable on the hyperfine transitions can be extended using several techniques. The most straightforward is the application of an external magnetic field to induce a larger magnetic moment on Pr^{3+}.

Another technique is zero first order Zeeman shift (ZEFOZ) [81]. This technique makes the transition frequency insensitive to small fluctuations in the magnetic field, and is achieved by using a magnetic field in which the frequency of one of the hyperfine transitions is at a turning point in all three directions. ZEFOZ has been used to extend the hyperfine coherence time in Pr:YSO to 1.4 s [82].

A third technique is dynamic decoherence control (DDC) [83], which involves repeatedly driving the transition of interest with a series of resonant π pulses. At a ZEFOZ point this actively rephases any decoherence which occurs on a slower timescale than the applied pulse sequence. Using ZEFOZ and DDC together hyperfine coherence times of 30 s [84] and 42 s [85] have been measured.

For a long range quantum repeater, storage times on the order of 1 second are required (see §1.6). Therefore, a practical repeater scheme would need to transfer information from the optical to the longer lived hyperfine transitions. The lifetime and coherence times for the optical and hyperfine ground state transitions in Pr:YSO are summarized in Table 2.3.

	Optical	Hyperfine ground state
T_1	164 μs [69]	200 s [78]
T_2	193 μs [79]	0.5 ms [80]
		1.4 s* [82]
		42 s** [85]

Table 2.2: Lifetime (T_1), and coherence time (T_2) values for optical and hyperfine transitions of Pr:YSO at zero field. *hyperfine coherence time using ZEFOZ technique. **hyperfine coherence time using ZEFOZ + DDC

2.2.2 Inhomogeneous Broadening

The inhomogeneous linewidth Γ_i is the linewidth of an ensemble of dopant ions, it arises because each ion experiences a slightly different local environment within the crystal. This shifts the center frequency of their transitions relative to each other, creating the broad inhomogeneous line of the ensemble, shown in Figure 2.3. This environmental variation over the crystal is due to *static* perturbations, which arise from crystal impurities and crystal strain. For example, in a doped crystal a size mismatch between dopant and the host ions they replace [86].

The inhomogeneous linewidths for the transitions of interest in Pr:YSO at zero magnetic field are well documented. For the optical ${}^3H_4 \rightarrow {}^1D_2$ transition the linewidth has been measured to be 3 GHz with for a dopant concentration of 0.005% [87]. While the inhomogeneous linewidths of the hyperfine ground state transitions are much narrower, on the order of 10 kHz for a dopant concentration of 0.02 % [69].

	Optical	Hyperfine ground state
Γ_h	1.65 kHz [79]	$\mathcal{O}$(1 kHz) [80]
Γ_i	3 GHz [87]	$\mathcal{O}$(10 kHz) [69]

Table 2.3: Comparsion of the homogeneous and inhomogeneous linewidths for the optical and hyperfine ground states of the ${}^3H_4 \rightarrow {}^1D_2$ transition in Pr:YSO.

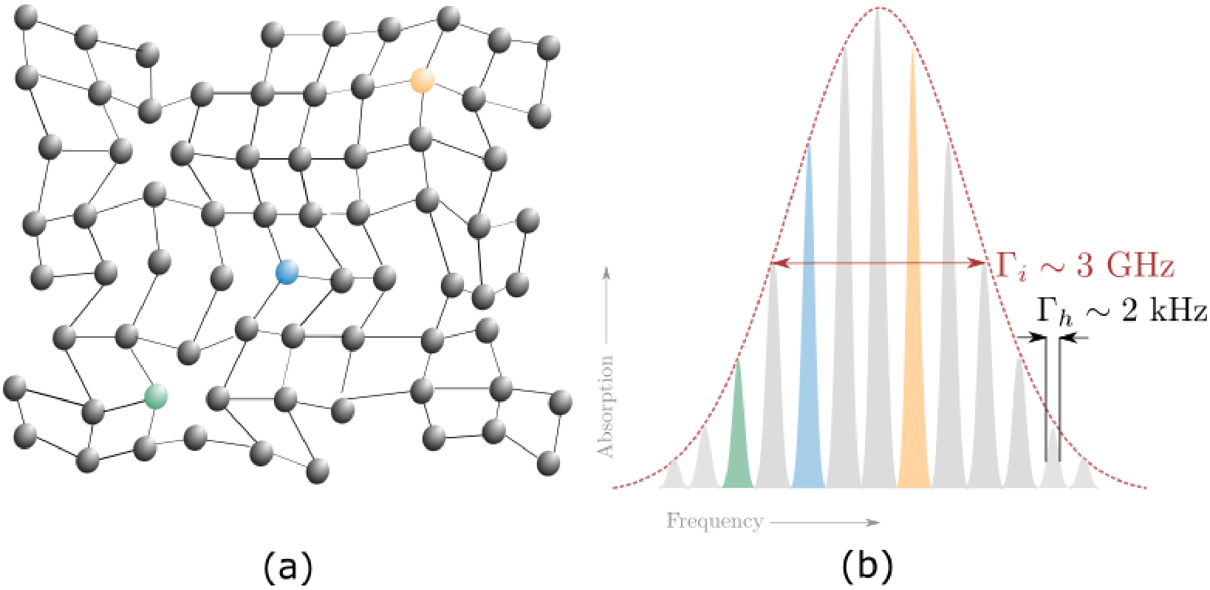

Figure 2.3: Illustration of how (a) lattice defects in the crystal cause Pr ions to experience slightly different local fields, creating the (b) inhomogeneous linewidth of the ensemble. Quoted linewidth values are for the optical $^3H_4 \rightarrow ^1 D_2$ transition in Pr:YSO with a dopant concentration of 0.005% [79] [87]. Note that the absorption profile of the broadened ensemble is Gaussian because less atoms exist in the wings of the profile, not because the oscillator strength has changed.

2.3 Spectral Holeburning

The main result from §2.2 was that for a rare-earth crystal to be an effective quantum memory of light, the hyperfine transitions must be leveraged. Therefore, each optical transition between the ground and excited state hyperfine level must be addressable with a unique laser frequency. This will occur if the splitting of the hyperfine levels is greater than the broadening of the optical $^3H_4 \rightarrow ^1 D_2$ transition. For Pr:YSO this is not the case, the hyperfine splittings are on the order of 10 MHz, illustrated in Figure 2.2, which are much smaller the 3 GHz inhomogeneous optical linewidth. This leaves all the optical transitions between the hyperfine levels effectively obscured under the large optical inhomogeneous line. In this work, spectral holeburning is used to pump ions of interest into a non-resonant state, creating narrow features in the broad optical inhomogeneous line.

To illustrate this technique, its easiest to consider a simplified case where each optical hyperfine transition can be addressed with a laser pulse, i.e the transitions are broadened *and* resolved. The holeburning procedure for this case is illustrated for an ensemble of four-level atoms in Figure 2.4. In (a) the ground states $|g_1\rangle$ and $|g_2\rangle$ are equally populated, and a spectrally narrow laser ν is resonant with the $|g_2\rangle \rightarrow |e_1\rangle$ transition. The ions in the $|g_2\rangle$ state are excited, then decay back into either state $|g_1\rangle$ or $|g_2\rangle$, shown (b). Repeating this process, the ions which decayed back into the $|g_2\rangle$ state are re-excited, and the ions that decayed into the $|g_1\rangle$ state are no longer resonant with the laser. Over many iterations, the $|g_2\rangle$ state will be completely cleared, and all ions of the ensemble will occupy a non-resonant storage state, shown in (c).

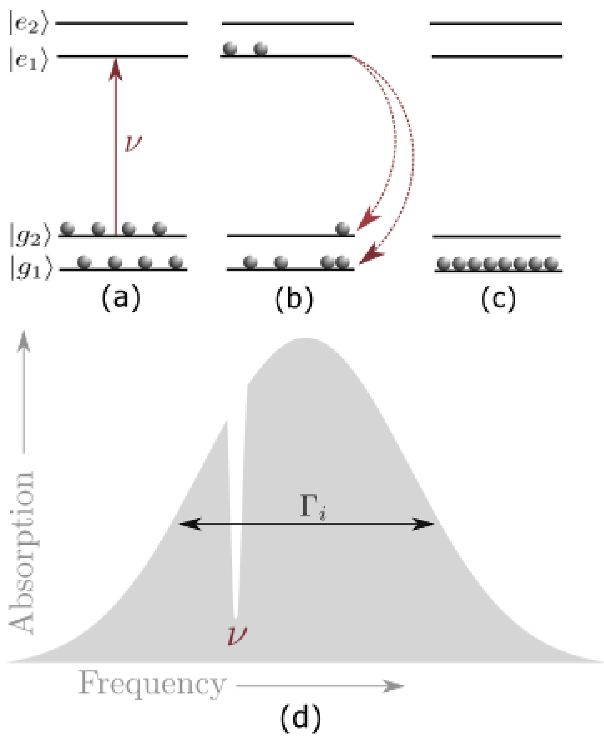

Figure 2.4: Illustration of spectral holeburning for a four-level ensemble of atoms, where each optical transition between the ground and excited hyperfine levels can be addressed with a unique laser frequency, i.e. the transitions are *resolved*. (a) A laser is applied at frequency ν and the ions are pumped out of $|g_2\rangle$. (b) the ions which decayed back into $|g_2\rangle$ are re-excited, while the ions which decayed into $|g_1\rangle$ are non-resonant. (c) Over many pumping iterations, $|g_2\rangle$ will be completely cleared into the non-resonant ground state. (d) The loss of absorption at frequency ν creates a spectrally transmissive window or 'hole' in the optical inhomogeneous line. This diagram ignores side-holes and anti-holes.

Using the optical pumping technique, outlined in Figure 2.4, absorption by the ensemble at the frequency ν will be reduced. This reduced absorption is observed as a spectral hole in the broad optical inhomogeneous line, shown in (d). Along with this, other spectral features will be created.

Absorption on the $|g_2\rangle \to |e_2\rangle$ transition will also be reduced, creating a side-hole, while absorption on the $|g_1\rangle \to |e_1\rangle$ and $|g_1\rangle \to |e_2\rangle$ transitions will be enhanced, creating 'anti-holes'.

The lifetime of these features are given by the cross-relaxation time, which for Pr:YSO is on the order of minutes. This allows the spectral holes to stay evacuated for the entirety of the

RASE experiment, which has a run time of ∼100 ms.

However, for the case of Pr:YSO the hyperfine optical transitions are broadened and *not* resolved. Therefore, a laser will not be resonant with a single transition but multiple transitions.

This is illustrated for an ensemble of four-level ions in Figure 2.5 (a), where a laser ν can be resonant with four different subgroups in the ensemble. This corresponds to the spectral structure shown in (b), where 9 different features have been created.

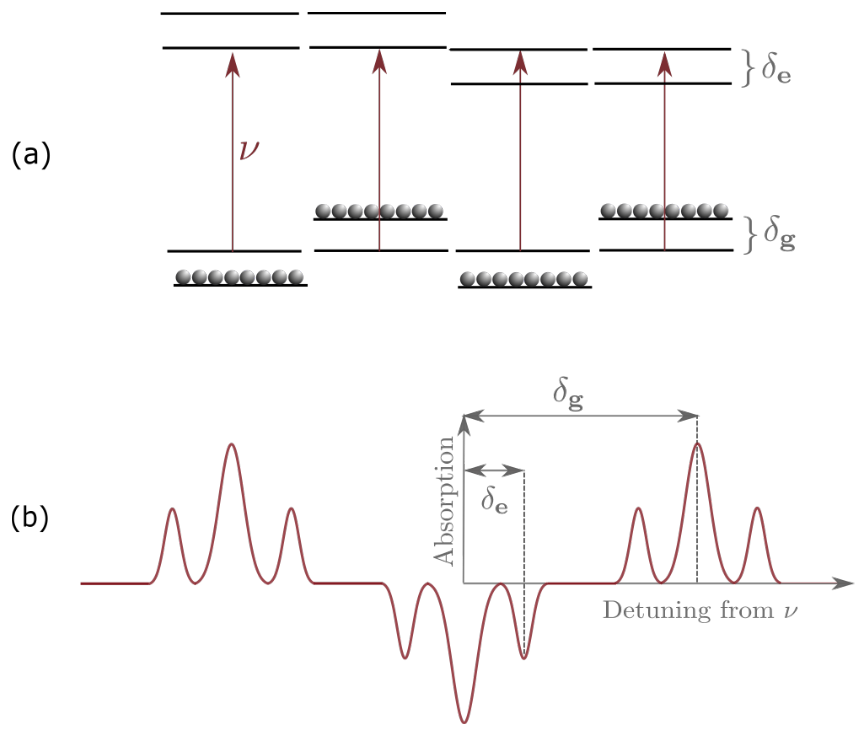

Figure 2.5: Illustration of (a) how a laser can be resonant with four different subgroups which correspond to slightly different optical transitions in an ensemble of four-level ions. (b) The absorptive profile created in the optical inhomogeneous line, after the holeburning process, with holes (below the horizontal axes) and anti-holes (above the horizontal axes). For simplicity the structure assumes the absorption profile is initially flat.

For Pr:YSO this behavior is even more complicated. At zero magnetic field the three ground and excited hyperfine levels will cause 9 resonant subgroups to exist. This results in a 49 feature spectral structure where the relative size of the features depends on the transition oscillator strengths (see §2.1). For this work we chose to remove this complication, selecting only a single subgroup of ions to perform RASE experiment on (see §4.3).

In order for spectral holeburning to be an effective technique, the large absorptive background of the optical inhomogeneous line must be removed. This can be done by sweeping the laser over several megahertz, creating broad transmissive window in inhomogeneous line. Inside this broad transmissive window, anti-holes of controllable bandwidth can then be burnt back. This burn-back method is effective at creating the small bandwidth features needed for the experiments done in this work. The drawback is the time required to create them, taking 10-100 ms, which limits the repetition rate of an experiment to < 100 Hz.

2.4 Photon Echo Techniques

The RASE protocol uses photon echo techniques which allow light to be stored and recalled, on demand, at a later time [88]. In this section the standard two-level echo protocol is illustrated, which is useful for classical information storage [89], however, it is not useful for quantum information storage. This is because is difficult to discriminate quantum information from the strong control fields. The four-level echo addresses this issue, and is outlined in this section.

2.4.1 Bloch Sphere Representation

The state of an ensemble of two-level atoms can be represented with a Bloch sphere, illustrated in Figure 2.6. The Bloch vector **k** describes the state of an ensemble by its position on the surface of the sphere, if no decoherence or dephasing has occurred. When positioned on the $-z$ or $+z$ pole the vector describes the ensemble in a purely ground $|g\rangle$ or purely excited state $|e\rangle$, respectively. An arbitrary superposition state between these two points is expressed as

$$|\psi\rangle = \sin\left(\frac{\theta}{2}\right)|g\rangle + e^{i\phi}\cos\left(\frac{\theta}{2}\right)|e\rangle, \tag{2.2}$$

where $\theta \in [0, \pi]$ and $\phi \in [0, 2\pi]$. When the vector lies on the equator of sphere this represents a 50/50 superposition of states $|g\rangle$ and $|e\rangle$, with the azimuthal angle ϕ defining the phase relationship of the superposition.

To relate the physical behavior of the material to the Bloch sphere model a fictitious electric spin vector is created for each atom, which is related to its electric dipole moment $\boldsymbol{\mu}$. When all these spins are in phase with each other, the ensemble state can be represented by the single Bloch vector **k**. A torque can be applied on the Bloch vector to rotate it around the x-axis by applying a steady light field at the Rabi frequency

$$\chi = \frac{\boldsymbol{\mu} \cdot \boldsymbol{E}}{\hbar}, \tag{2.3}$$

where $\boldsymbol{E}$ is the amplitude of the applied electric field. The ensemble can be driven into a superposition of states $|g\rangle$ and $|e\rangle$ by applying a field of light at the Rabi frequency for a short amount of time. Once in a superposition of states, the spin vectors of the ensemble will begin to dephase. Each spin of the ensemble will begin to rotate about the z-axis at a rate defined by the unique transition frequency of the atom.

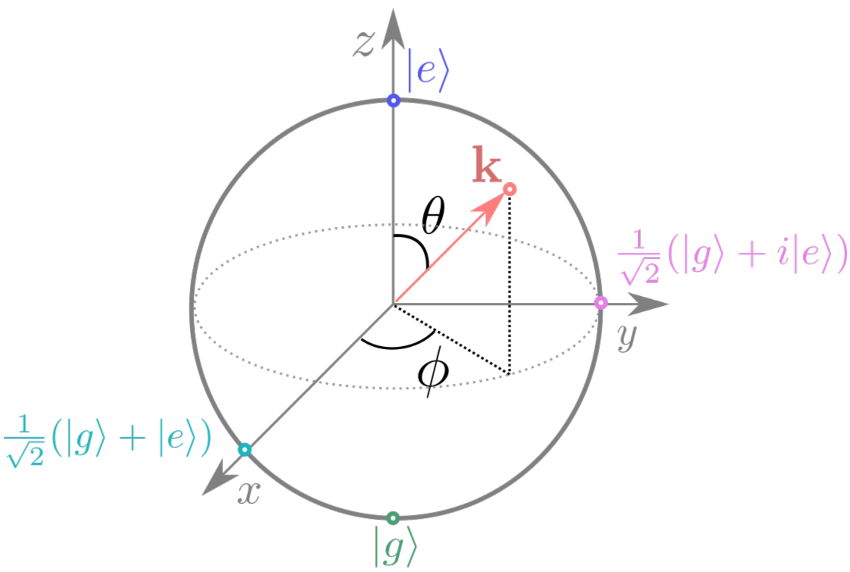

Figure 2.6: Bloch sphere representation of the state of an ensemble of two-level atoms, where the position of the Bloch vector **k** on the surface of the sphere describes the state.

For simplicity the Bloch sphere is typically viewed in a rotating reference frame. In this frame the spin vector which is directly on resonance with the applied light field will remain stationary, while other vectors will begin to rotate at their detuned frequencies. When the Rabi frequency is much greater than these detunings the rotation of the Bloch vector around the x-axis is given by χt, where t is the pulse duration time. Photon echo sequences use *control pulses* to rotate the Bloch vector by a controlled angle. When the Bloch vector is tipped by 90° this is known as a $\frac{\pi}{2}$ pulse, and when the tipping angle is 180° this is known as a π pulse.

2.4.2 Two-level Photon Echo

The two-level echo pulse sequence and the corresponding progression of spin vectors on the Bloch sphere is illustrated in Figure 2.7. The ensemble is prepared in ground state $|g\rangle$ and a $\frac{\pi}{2}$ pulse is used to create a 50/50 superposition states $|g\rangle$ and $|e\rangle$, shown in (a). When the control pulse is shut off, the beginning a free induction decay (FID) is observed. At this point all spin vectors are in phase and a large electric field is detected. All atomic radiation adds together constructively, and therefore the emitted light is coherent.

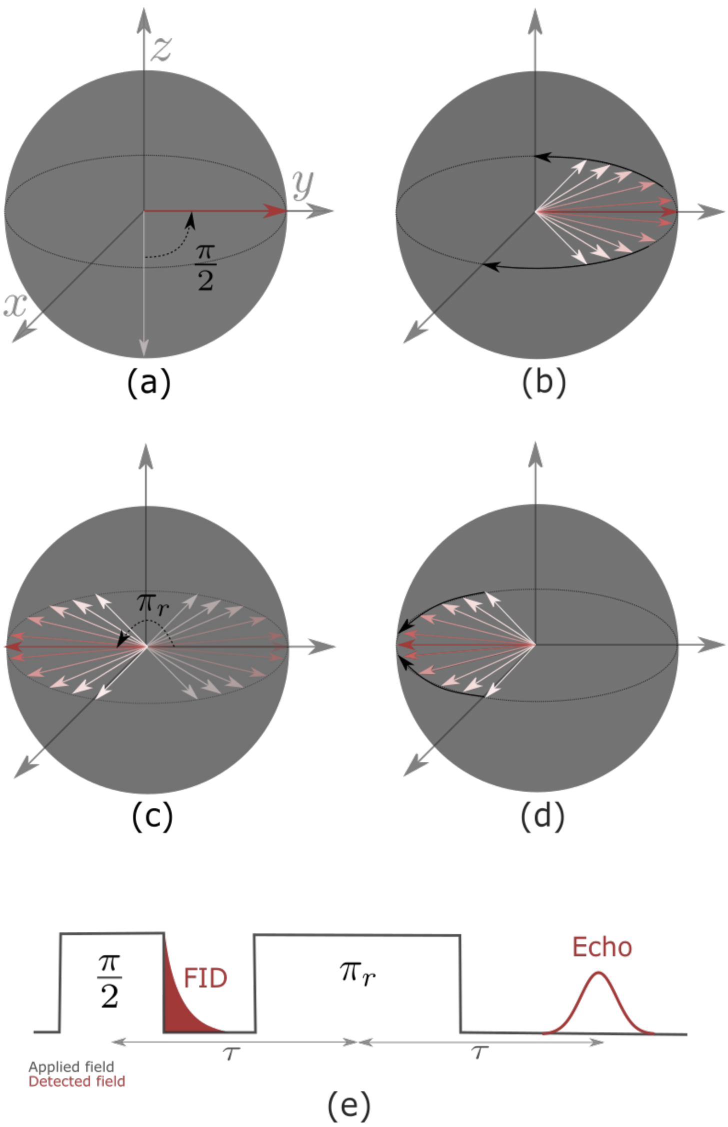

Figure 2.7: The Bloch sphere illustration of a two-level photon echo. (a) A $\frac{\pi}{2}$ pulse is used to create a 50/50 superposition of states $|g\rangle$ and $|e\rangle$, and beginning of a detectable FID signal. (b) The amplitude of the detected FID reduces over time as the spins begin to dephase. (c) A rephasing pulse π_r is applied at a time τ after the $\frac{\pi}{2}$ pulse, rotating the spins 180° about the x-axis. (d) The rephased spins are detected as an optical echo a time τ after the rephasing pulse was applied. (e) The corresponding temporal pulse sequence.

Over time the spin vectors will begin to dephase, illustrated as a 'fanning out' of the individual spins around the Bloch sphere equator in (b). This is observed as a decay in the FID signal, as atomic radiation begins to add together destructively. The length of this decay is proportional to the inverse of the ensemble's inhomogeneous linewidth (see §2.2), provided the entire ensemble has been addressed with the $\frac{\pi}{2}$ pulse, and observed long after the control field is shut off. This means if a narrow feature has been prepared using spectral holeburning, the decay will occur more slowly.

When the FID does become zero all spins will be completely out of phase, however, the individual spins still continue to precess. A rephasing π_r pulse is applied after a delay time τ, which rotates the vectors around the x-axis. The effect is that the spin vectors, still still traveling in the same direction as before, are now rephasing towards the $-y$ pole of the sphere, displayed in (c). The spins will arrive back in phase after a time τ and an echo of the original FID will be emitted.

When the total delay time 2τ is increased the intensity of the emitted echo I will decay at a rate given by coherence time T_2,

$$|\mathrm{I}(2\tau)| \propto e^{-\frac{4\tau}{T_2}}. \tag{2.4}$$

The efficiency of the emitted echo will also depend on the spatial relationship with the two control pulses. The echo will be maximally efficient when the following phase matching condition is satisfied

$$\mathbf{k}_{echo} + \mathbf{k}_{\frac{\pi}{2}} = 2\mathbf{k}_{\pi_r}. \tag{2.5}$$

This means an optimal echo will be emitted in the same direction as the control pulses. Therefore, the two-level photon echo protocol does not allow the detection of the final echo in a different spatial mode from the control pulses.

2.4.3 Using the Two-level Echo as a Basis for a Quantum Memory

The two-level echo performs well as a classical memory [89] but a quantum memory has different requirements (see §1.4). Most quantum memory protocols which use rare-earth ion-doped crystals, the material used in this work, rely on the rephasing techniques used in the two-level echo protocol [90, 43, 44, 45, 47].

The two-level echo protocol, modified to perform as quantum memory, is illustrated in Figure 2.8. Unlike the classical two-level echo illustration in Figure 2.7, two Bloch spheres are shown: one with the individual spin vectors, and one with the projection of the total Bloch vector $\mathbf{k}$ on the xy-plane. For a quantum memory a weak *input* state, at the single photon level, replaces the $\frac{\pi}{2}$ pulse used in the standard two level echo, shown in (a). The effect is the Bloch vector is only rotated by a small angle from the -z pole of the Bloch sphere. At this point the projection of the total Bloch vector on the xy-plane will be largest, and an FID will be observed. The total Bloch vector will then decay with the FID and eventually become zero, shown in (b).

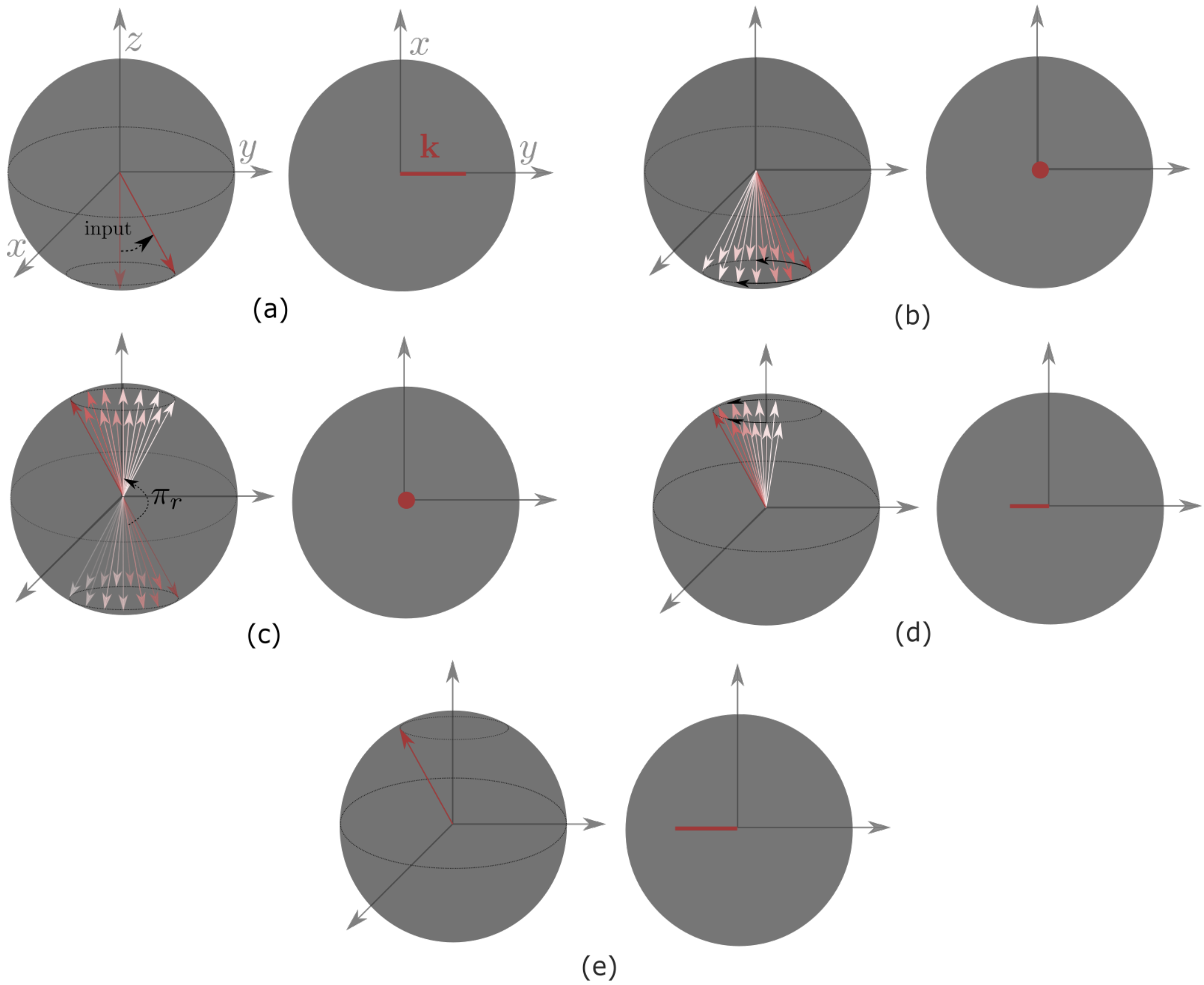

Figure 2.8: Bloch sphere illustration of a quantum memory which is based on the two-level echo protocol. Two spheres are shown: one with the individual spin vectors (LHS), and one with the projection of the total Bloch vector **k** on the xy-plane (RHS). (a) A weak input state is used instead of a $\frac{\pi}{2}$ pulse to rotate the Bloch vector by a small angle from the $-z$ pole. At this point the projection of the total Bloch vector of the xy-plane is maximum. (b) The projection of the total Bloch vector on the xy-plane reduces to zero as the spins begin to dephase. (c) The projection remains zero after the spins are inverted with a rephasing π_r pulse. (d,e) The magnitude of the projection begins to grow as the spins rephase towards the -y pole of the Bloch sphere.

The rephasing π_r pulse is applied which *inverts* the ensemble into a predominantly excited state, shown in (c). After this inversion the projection of the total Bloch vector on the xy-plane remains zero because the spins remain completely dephased. As rephasing occurs the projection then grows in magnitude towards to -y pole, shown in (d) and (e).

The key difference from the classical two-level echo is that after the rephasing pulse is applied the ensemble is no longer in a 50/50 superposition state of the ground and excited state. Instead, the ensemble is in a predominantly excited state. Because the input state was very small, the effect is that an amplification medium with high gain is created. The medium amplifies the vacuum state within the crystal and creates amplified spontaneous emission (ASE). Because the final optical echo is detected on the same transition, ASE is a source of unwanted noise and means the two-level echo does not make a good quantum memory in practice [91].

The rephased amplified spontaneous emission scheme (RASE) [47] is the memory protocol investigated in this work. The two-level RASE protocol (outlined in §3.1) is an adaption of the two-level echo as quantum memory which turns ASE as a resource, instead of a source of unwanted noise. This is achieved by inverting the ensemble into an excited state at the beginning of the protocol. The large optical gain means ASE is detected a short time later, which heralds a collective atomic state over the ensemble. The collective state then immediately begins to dephase, which is corrected with a rephasing π pulse. The rephased collective state is then read out in a second optical field called rephased amplified spontaneous emission.

Because ASE is no longer a source of unwanted noise, the two-level RASE protocol should be a successful adaptation of the two-level echo as a quantum memory. However, in practice some residual noise will always follow the strong control pulses in the form of a FID. An FID will be detected when the projection of the total Bloch vector on the xy-plane is non-zero. In Figure 2.8 (c) this projection was zero after the rephasing π_r pulse. However, because the amplitude profile of the rephasing pulses are Gaussian (see §6.1.3), some spins will experience a pulse area less than or greater than π_r. As a result, the projection of the total Bloch vector on the xy-plane, after the rephasing pulse, will never be zero. An FID will always be observed at the same frequency and time as the small RASE signal, obscuring its detection.

The ASE signal will also be obscured by any FID which follows the inverting pulse, which will occur at the same frequency and time as the small quantum signal. This is because some population will inevitably be left in the ground state, and the total Bloch vector will be displaced from the $+z$ pole by some small angle.

Altogether, the reality of imperfect control pulses means the two-level echo protocol is an unsuitable basis for RASE. Instead, RASE must be based on a four-level echo protocol, which is motivated by the desire to spectrally resolve the small ASE and RASE signals from the unavoidable FID which will follow the strong control fields.

2.4.4 Four-level Photon Echo

A more suitable basis for a quantum memory, when compared to the two-level echo, is the four level echo [74]. When adapted for a quantum memory, the frequency of each control pulses can be selected such that they are different from the small quantum signals.

Beyond the two level case the Bloch sphere representation in no longer an effective tool for understanding the protocol, therefore, an energy level based explanation is shown in Figure 2.9. A $\frac{\pi}{2}$ pulse is applied on the $|g_1\rangle \leftrightarrow |e_1\rangle$ transition, creating a 50/50 superposition of states $|g_1\rangle$ and $|e_1\rangle$. After a time τ_a the coherence initialized between $|g_1\rangle$ and $|e_1\rangle$ is the shifted between the two ground states, $|g_1\rangle$ and $|g_2\rangle$, with the application of a rephasing π_{r_1} pulse on the $|g_2\rangle \leftrightarrow |e_1\rangle$ transition. After a delay of τ_b a second rephasing π_{r_2} pulse is applied on the $|g_1\rangle \leftrightarrow |e_2\rangle$ transition, which shifts the coherence between states $|g_2\rangle$ and $|e_2\rangle$. After an additional time τ_a an optical echo will be observed on the $|e_2\rangle \leftrightarrow |g_2\rangle$ transition.

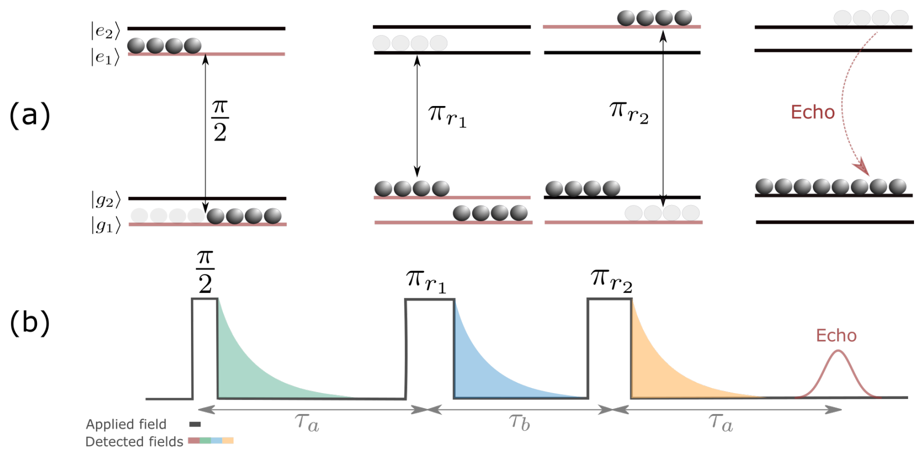

Figure 2.9: Illustration of the four-level echo protocol using an (a) energy level representation. Application of a $\frac{\pi}{2}$ pulse initializes coherence between $|g_1\rangle$ and $|e_1\rangle$. The first rephasing pulse π_{r_1} then shifts this coherence between the two ground hyperfine states $|g_1\rangle$ and $|g_2\rangle$. The second rephasing pulse π_{r_2} then shifts this coherence between $|g_2\rangle$ and $|e_2\rangle$. The final optical echo is then observed on the $|e_2\rangle \leftrightarrow |g_2\rangle$ transition. (b) The corresponding temporal pulse sequence where the optical echo is detected at a different frequency from any free induction decay (FID) which follows the strong control pulses (see §2.4.3).

Using a four-level protocol corrects many of the drawbacks inherent to the two-level. Firstly, the phase matching condition for an optimally efficient echo is now

$$\mathbf{k}_{echo} + \mathbf{k}_{\frac{\pi}{2}} = \mathbf{k}_{\pi_{r_1}} + \mathbf{k}_{\pi_{r_2}}, \tag{2.6}$$

where the relationship can be satisfied with counter-propagating rephasing π pulses. This allows the echo to be spatially distinct for the bright control fields, adding an extra layer of flexibility to the experiment.

There is also no need to create perfect π pulses to reduce FID-decay noise. This is because all control pulses are applied on different transitions from the final optical echo. The small quantum signals of the rephased amplified spontaneous emission scheme will therefore be spectrally distinct from this unavoidable noise source.

The drawback of using four levels instead of two is that additional inhomogeneity will be introduced. A consequence of using two rephasing π pulses on different transitions is that only the effects of inhomogeneity common to their transitions will be rephased. Therefore, additional decoherence will be introduced if the affects of the inhomogeneity are unrelated. This means that the four-level optical decay time will always be less than the two-level coherence time. However, there is an additional benefit that makes the total storage time longer.

A hyperfine storage phase is created over time τ_b, when the coherence is shifted between the ground states $|g_1\rangle$ and $|g_2\rangle$. For Pr:YSO this sets a much longer lifetime limit on the coherence times attainable, because the lifetime of the hyperfine transitions is 200 s compared to 164 μs for the optical (see Table 2.3).

Further decoherence will be introduced by the effects of inhomogeneity during the hyperfine storage phase when $\tau_b > 0$, will not be rephased by the two optical rephasing pulses. It was proposed by Beavan *et. al* [74] that π_{RF}-pulses could be applied on the ground hyperfine transition to correct this. This was demonstrated by Berrington [92], who extended the hyperfine coherence time from $\sim$ 48 μs [73] to 1.2 ms using hyperfine rephasing pulses in zero magnetic field. Using a combination of ZEFOZ and DDC techniques the hyperfine coherence times achievable should be on the order of 10 s (see Table 2.3).

Therefore, using the four-level echo protocol as a basis for the rephased amplified spontaneous emission protocol holds great promise. Firstly, a storage phase on a ground state hyperfine transition has been integrated into the protocol. This allows coherence times on the order of tens of seconds to be engineered using a combination of ZEFOZ and DDC techniques, the same order of magnitude as required for a large-scale quantum repeater (see §1.6). Secondly, the experiment can be performed such that the small quantum signals are spatially distinct from the bright control pulses. Thirdly, the small quantum signals are also spectrally distinct from the bright driving fields, and any unavoidable FID noise.

2.4.5 Summary

The unique properties of rare-earth ion-doped crystals make them an ideal candidate for quantum communication technologies. The hyperfine transitions are of particular interest, where the coherence times required for large-scale quantum communication can be engineered. The repeater protocol investigated in this work is based on rephased amplified spontaneous emission (RASE), which requires storage times on the order of seconds in order to operate long-range (see §1.6) .

One challenge to performing RASE in rare-earth ion-doped crystals is the broadening of the optical transitions. In Pr:YSO the broadening of the optical $^3H_4 \rightarrow ^1 D_2$ transition renders the optical transitions between the ground and excited hyperfine levels unaddressable. This issue can be resolved by using spectral holeburning techniques, to engineer narrow absorptive features in the broad optical inhomogeneous line.

Using photon echo techniques the coherence properties of rare-earth ion-doped crystals to be fully leveraged, by removing the effects of static inhomogeneous broadening. The two-level photon echo was shown to be an effective method to store and recall classical information. However, when repurposed as a quantum memory, the small quantum signals were indistinct from any unavoidable noise following the bright control feilds.

The solution was to apply the bright control fields on different transitions from the echo, and use four levels instead of two. An added benefit on using four-levels was the integration of a storage phase on one of the long-lived ground hyperfine transitions of Pr:YSO. On this transition coherence times of the order of tens of seconds can be engineered using a combination of ZEFOZ and DDC techniques, which satisfies the storage time requirement necessary for long distance quantum communication.

Chapter 3

The RASE Protocol

A quantum repeater is an essential device for long-range quantum communication. In its simplest form, it requires two components: a quantum memory and an entangled light source. Using rephased spontaneous emission (RASE) [12] is an elegant way to integrate these two components, and take full advantage of the coherence properties of rare-earth ion-doped crystals. In this chapter, RASE is introduced using two-level system in §3.1, and the drawbacks are discussed. Many of these drawbacks are then rectified using the four level protocol, with illustrated in §3.2.

The discriminating feature of a quantum repeater, when compared to a trusted node network (see §1.3), is that the distributed information can be stored non-classically. A quantum repeater which is based on RASE, stores information on the collective state of an ensemble of rare-earth ions. Because the coherence times in rare-earth crystals are long, information about the ensemble can be readout as two entangled fields of light. In this work, the inseparability criterion (see §3.3) is the metric chosen to assess whether theses two fields are non-classically correlated, i.e. entangled.

In order for RASE to be a viable quantum repeater, the the two entangled fields should be rephased with an efficiency exceeding 90%. In §3.4 the efficiency of RASE is predicted with optical gain. The result shows that to reach the threshold efficiency for a quantum repeater, RASE must operate at an optical depth exceeding 2.5. Previous work was limited to an efficiency of 3% at an optical depth of 2.3 [73]. The explanation for this was a spatial mode mismatch between the first and second pass of the beams through the crystal. This was the direct consequence of a mirror not being positioned correctly below the crystal, discussed in §3.5.

3.1 Two-level RASE

In §2.4 the two-level echo was shown be unsuitable basis for a quantum memory. This was because the final echo occurs on a transition with large optical gain and, therefore, amplified spontaneous emission (ASE) is a source of unwanted noise.

The two-level RASE protocol is an adaption of the standard two-level echo memory, where instead, ASE is used as a resource. The two-level RASE protocol is illustrated in Figure 3.1. Unlike the two-level echo, the ensemble is shifted into the the excited state $|e\rangle$ using an inverting pulse *inv*. The collective state of the inverted ensemble can be expressed as a tensor product of N atoms being in the excited state

$$|\psi\rangle = \prod_{n=1}^{N} |e_n\rangle = |e_1, e_2, ...e_N\rangle. \tag{3.1}$$

Amplified spontaneous emission, as a consequence of the high gain on the $|g\rangle \leftrightarrow |e\rangle$ transition, is then detected (see Section 2.4.3). This heralds the ensemble into a superposition state of any atom having decayed, and is an example of 'entanglement via indistinguishability' (see §1.4.1). The collective atomic state of the ensemble can now be written as

$$|\psi\rangle = \frac{1}{\sqrt{N}} \sum_{n=1}^{N} e^{-i\mathbf{k}\cdot\mathbf{x}_n} |e_1, e_2, ...g_n...e_N\rangle, \tag{3.2}$$

where $\mathbf{k}$ is the wave-vector of the spontaneously emitted photon, and $\mathbf{x}_n$ is the position of the n^{th} atom in the ensemble. This collective state will also be entangled with the spontaneously emitted field [73].

Because the ensemble is inhomogeneously broadened, the collective state will then begin to dephase. Similar to the photon echo (see §2.4.2), the state can be rephased by applying a rephasing pulse π_r, a time τ, after the ASE event. Because the coherence times in Pr:YSO are long (see Table 2.3), the collective state of the ensemble can be readout in the rephased optical field (RASE). In addition, both emitted fields will be entangled with each other [12, 93].

The rephasing of the ASE field will be maximally efficient when the following phase matching condition is met

$$\mathbf{k}_{RASE} = 2\mathbf{k}_{\pi_r} - \mathbf{k}_{ASE}. \tag{3.3}$$

Therefore, for two-level RASE, the ASE and RASE signals will be maximized when they

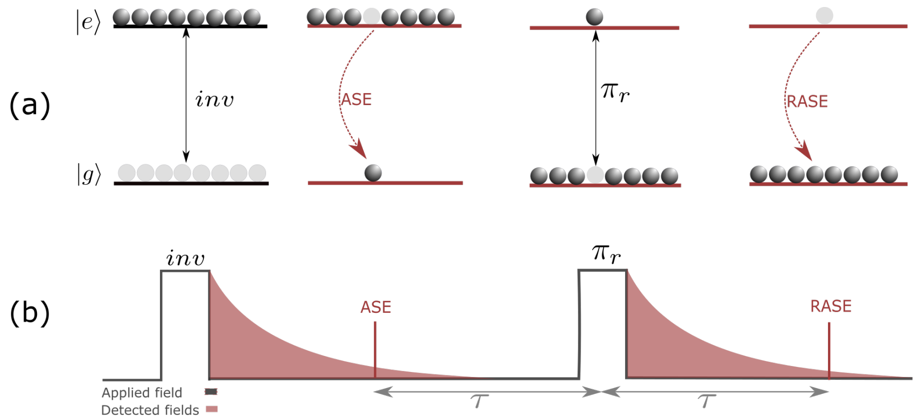

Figure 3.1: Illustration of the two level RASE protocol using (a) an energy level representation. The ensemble is shifted from the ground state $|g\rangle$ to the excited state $|e\rangle$ with an inverting pulse *inv*. A rephasing pulse π_r is applied, a time τ, after the detection of the amplified spontaneous emission (ASE) event. The rephased field (RASE) is then observed at a time τ after the rephasing pulse. (b) The corresponding temporal pulse sequence where ASE and RASE are detected at the same frequency as any free-induction decay (FID) that follows the bright control pulses (see §2.4.3).

are detected collinear to the rephasing pulse. This is the same result as the two level echo (see §2.4.2).

In theory, the RASE protocol should perform optimally with only two levels, however, experimentally the protocol is difficult to implement. This is because, following the bright control pulses, a free-induction decay (FID) will always be observed, illustrated in Figure 3.1. This decay will be spectrally indistinct from the small ASE and RASE signals (see §2.4.2). However, if the FID is short compared to T_2 it is possible to distinguish between the fields temporally [93]. Another solution is to use four levels, where each control pulse is applied at a different frequency from the emitted signals.

3.2 Four-level RASE

Four-level RASE is an adaption of the four-level echo, introduced in §2.4.4, for a quantum memory. The energy level representation and control pulse sequence for the protocol shown in Figure 3.2. Firstly, the population is initialized in the 'storage state' $|g_0\rangle$ (see §4.3). The inversion pulse is applied on the $|g_0\rangle \leftrightarrow |e_1\rangle$ transition, which shifts the population into the state $|e_1\rangle$. The result is that ASE is detected on a different transition form the inverting pulse. Detection of the ASE event then heralds the ensemble into a superposition of states $|g_1\rangle$ and $|e_1\rangle$ (see §3.1).

The first rephasing pulse π_{r_1} is applied on $|g_2\rangle \leftrightarrow |e_1\rangle$ transition at a time τ_a after the ASE event. This shifts the coherence between the two ground states $|g_1\rangle$ and $|g_2\rangle$. The second rephasing pulse π_{r_2} is applied at a time τ_b later, which acts to shift the coherence between the states $|g_2\rangle$ and $|e_2\rangle$. The cumulative effect of these two rephasing pulses is that the ensemble evolves and RASE is detected on the $|g_2\rangle \leftrightarrow |e_2\rangle$ transition.

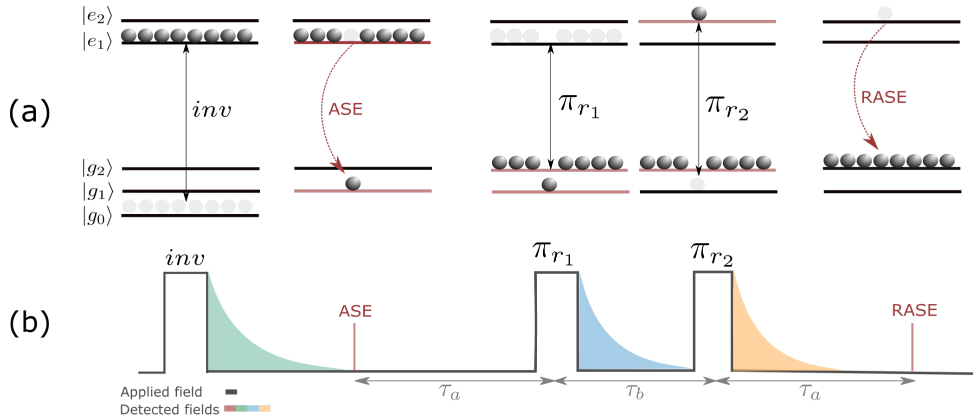

Figure 3.2: Illustration of the four level RASE protocol using (a) an energy level representation. The inverting pulse *inv* is applied on the $|g_0\rangle \leftrightarrow |e_1\rangle$ transition, and the first rephasing pulse π_{r_1} is applied on the $|g_2\rangle \leftrightarrow |e_1\rangle$ transition at a time τ_a after the ASE event is detected on the $|g_1\rangle \leftrightarrow |e_1\rangle$ transition. A second rephasing pulse π_{r_2} is applied on the $|g_1\rangle \leftrightarrow |e_2\rangle$ transition at a time τ_b after the first rephasing pulse. At a time τ_a after the second rephasing pulse RASE is detected on the $|g_2\rangle \leftrightarrow |e_2\rangle$ transition. (b) The corresponding temporal pulse sequence where ASE and RASE are detected at a different frequency from any free-induction decay (FID) following the bright control pulses (see §2.4.3).

Using four-level RASE, any free induction decay which follows the bright control fields will be at a different frequency from the spontaneously emitted fields, illustrated in Figure 3.2. Therefore, the noise issue inherent of the two-level system has been resolved by moving to four levels.

Furthermore, a maximally efficient RASE signal will be measured when the following phase matching condition is satisfied,

$$\mathbf{k}_{RASE} + \mathbf{k}_{ASE} = \mathbf{k}_{\pi_{r_1}} + \mathbf{k}_{\pi_{r_2}}. \tag{3.4}$$

This can be met with two counter-propagating rephasing pulses. This is the same result as the four level echo (see §2.4.4)). In this case, a maximally efficient RASE field will be detected in the opposite direction to the detected ASE field. This offers a greater level of flexibility when designing the experiment, as a maximally efficient RASE field can be spatially distinct from ASE and the two rephasing pulses.

Unlike the two-level system, the four-level protocol leverages the long coherence times available on the hyperfine transitions of rare-earth ions. During the delay time τ_b the coherence is shifted onto a ground hyperfine transition. This is the storage phase of the protocol where, in Pr:YSO, it is possible to engineer second-long coherence times. (see §2.2.1).

Altogether, four-level RASE can be used to create two entangled fields of light which are temporally, spectrally and spatially distinct from the bright control fields. In addition, RASE has an inbuilt storage phase, where the storage times required for a large-scale quantum communication can be engineered. These features position RASE as an ideal test-bed for the demonstration of quantum repeater technology.

3.3 The Inseparability Criterion

For the RASE protocol to be useful, it must be shown that the spontaneously emitted fields are entangled. This requires proving that the state which describes the entire system is 'inseparable' (see §1.2). Two common metrics used to verify this are the 'Inseparability criterion' [94] and the 'EPR criterion' [13].

The metric chosen for this work was the inseparability criterion. This was because, unlike the EPR criterion, the condition will hold no matter the level of loss in the experiment [95]. For an outline of the sources of loss in the RASE experiment refer to §4.5.

The inseparability criterion is a necessary and sufficient condition to verify inseparability for all Gaussian states. In this work ASE and RASE fields form a two-mode squeezed state [52]; which has a Gaussian distribution. A maximally entangled state can, therefore, be expressed as a co-eigenstate of a pair of EPR-type operators [13, 94]

$$\begin{aligned} \hat{u} &= \sqrt{b}\hat{x}_1 + \sqrt{1-b}\hat{x}_2, \\ \hat{v} &= \sqrt{b}\hat{p}_1 - \sqrt{1-b}\hat{p}_2, \end{aligned} \tag{3.5}$$

where $\hat{x}_i$ and $\hat{p}_i$ are the amplitude and phase quadratures of light (see §4.4), i=1,2 for the ASE and RASE fields respectively, and b $\in$ [0,1] is a weighting parameter. The $\hat{u}$ operator combines the two amplitude operators, while $\hat{v}$ combines the two phase operators. This means that when the weighting parameter is zero the operator pair is entirely dependent on the RASE field. Conversely, when the weighting parameter is equal to one the operator pair is entirely dependent on the ASE field.

The inseparability criterion then states, that for any separable quantum state ρ, the sum of the variance of the two EPR-type operators should be greater or equal to two. However, for an inseparable state, the variance is bounded below by zero

$$2 > \langle(\Delta\hat{u})^2\rangle_\rho + \langle(\Delta\hat{v})^2\rangle_\rho \geq 0. \tag{3.6}$$

The expression can be simplified by noting the variance in an operator $\langle(\Delta\hat{o})^2\rangle$ is equal to the difference between the expectation value of the operator squared $\langle\hat{o}^2\rangle$, and the square of its expectation value $\langle\hat{o}\rangle^2$:

$$\langle(\Delta\hat{o})^2\rangle = \langle\hat{o}^2\rangle - \langle\hat{o}\rangle^2. \tag{3.7}$$

Because the amplitude and phase of spontaneous emission should be completely random, the expectation value of the EPR-type operator will be zero. This is verified in the RASE experiment, for both the ASE and RASE fields (see §5.3 and §6.2). As a result, the total variance of $\hat{u}$ and $\hat{v}$ can be expressed as

$$\begin{aligned}\langle(\Delta\hat{u})^2\rangle &= \langle\hat{u}^2\rangle = b\langle\hat{x}_1^2\rangle + (1-b)\langle\hat{x}_2^2\rangle + 2\sqrt{b(1-b)}\langle\hat{x}_1\hat{x}_2\rangle,\\ \langle(\Delta\hat{v})^2\rangle &= \langle\hat{v}^2\rangle = b\langle\hat{p}_1^2\rangle + (1-b)\langle\hat{p}_2^2\rangle + 2\sqrt{b(1-b)}\langle-\hat{p}_1\hat{p}_2\rangle.\end{aligned} \tag{3.8}$$

The covariance terms, $\langle\hat{x}_1\hat{x}_2\rangle$ and $\langle-\hat{p}_1\hat{p}_2\rangle$, provide a measure of the cross-correlation between the ASE and RASE fields [73]. Therefore, a non-linear inseparability curve will indicate that either the amplitude and/or phase quadrature values of the emitted fields are correlated, i.e. either covariance terms are non-zero.

The inseparability curve can also be used as a precise way to characterize the level of classical noise in the RASE experiment. This can be inferred with a comparison between an experimental and theoretical inseparability curve. If the theoretical curve is less than the experimental result, this indicates that classical noise is being scattered into the RASE modes in the rephasing stage of the protocol.

3.4 Modeling the Inseparability Criterion

In §3.3 the quadrature values, of the emitted fields, were shown to be key ingredients to building an inseparability curve. Therefore, to create a theoretical curve the measured quadrature values must be predicted. These values will be equally affected by any sources of loss which are external to the crystal. Therefore, a 'loss model' [73] is introduced in §3.4.1, which predicts the measured values based on the known sources of loss in the RASE experiment (see §4.5).

A second model, called the 'optical depth model' [96], is introduced in §3.4.2, which is used to predict the gain dependency of the quadrature values. In conjunction, the two models can be used to predict the efficiency of RASE with gain.

3.4.1 The Loss Model

The loss model predicts the measured quadrature values, based on a fixed value for the total loss L, in the RASE experiment (see §4.5). A single beamsplitter with transmission $l = 1 - L$ is used to incorporate the total loss into the model, where l is the 'loss parameter'. With this approach, the measured amplitude $\hat{x}$ and phase $\hat{p}$ quadrature values become

$$\begin{aligned} \hat{x}_i &\rightarrow \sqrt{l}\hat{x}_i + \sqrt{(1-l)}\hat{a}_i, \\ \hat{p}_i &\rightarrow \sqrt{l}\hat{p}_i + \sqrt{(1-l)}\hat{a}_i, \end{aligned} \tag{3.9}$$

where i=1,2 for ASE and RASE fields respectively, and $\hat{a}$ is the vacuum state entering the unused port of the beamsplitter.

The loss model is illustrated for the ASE quadrature values in Figure 3.3 (a). To model the measured RASE quadratures values the rephasing efficiency η also needs to be taken into account. This is incorporated using a second beamsplitter with transmission η, shown in Figure 3.3 (b). For the rephasing process the state $\hat{s}$ entering the unused port is ideally the vacuum. However, this will be larger than the vacuum if extra noise is scattered in the rephasing process. If this is the case, classical noise will be scattered into the RASE modes, and the theoretical inseparability curve will be less than the experimental result.

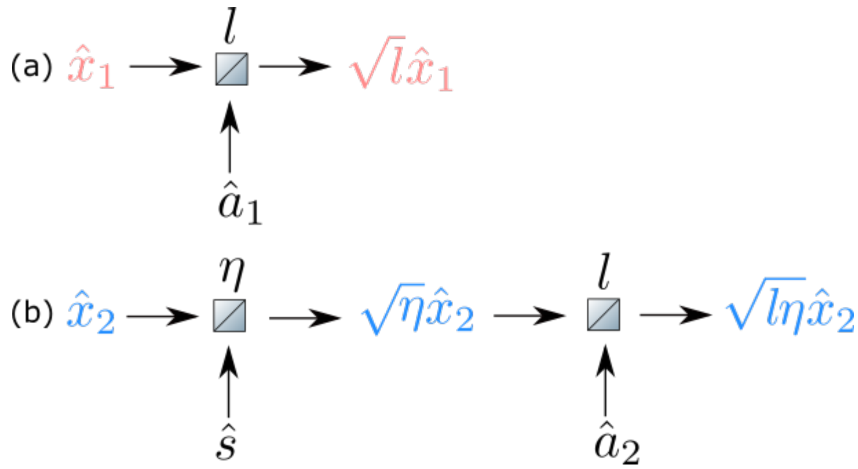

Figure 3.3: Illustration of the 'loss model' [73] used to predict the measured quadrature values of ASE and RASE, which will be affected by sources of loss in the RASE experiment (see §4.5). Only the transformation of the amplitude value (see Eq. (3.9)) is shown, and the vacuum term is not included. The affect of loss on the amplitude value of the (a) ASE field is modeled with a single beamsplitter of transmission l, where vacuum state $\hat{a}_1$ enters the unused port. The affect of loss on the amplitude value of the (b) RASE field is modeled with two beam splitters: one with tranmission l, where the vacuum state $\hat{a}_2$ enters the unused port; and one with transmission η, where $\hat{s}$ enters the unused port and is ideally the vacuum state.

In Figure 3.4 the inseparability criterion is modeled with a linearly increasing weighting parameter b. The position of the curve minimum indicates how strongly the ASE and RASE fields are non-classically correlated. When no sources of loss are present in the RASE experiment, and the rephasing efficiency is 100%, the curve minimum is positioned at zero. This is the best possible result to indicate the ASE and RASE fields are non-classically correlated. Furthermore, the strongest correlation exists when the fields are equally weighted, i.e. the minimum corresponds to a weighting parameter of 0.5.

When sources of loss in the experiment are accounted for, the minimum increases towards the classical boundary. In this case, both signals have been reduced by 89 % (see §4.5), and the non-classical correlation is weaker. Because both fields are equally affected by the loss, the strongest correlation still occurs when the fields are equally weighted. Therefore, the curve remains symmetric.

To model the experimental curve, the imperfect rephasing efficiency must be accounted for. In Chapter 7 the efficiency of RASE η, in the non-classical regime, was measured to be $\sim$8%. Incorporating the measured efficiency into the model, the minimum shifts towards b=0 and the curve becomes asymmetric. This is because the strongest correlation exists when more weight is given to the much smaller RASE field. The minimum also increases, as a smaller RASE field will reduce the non-classical correlation.

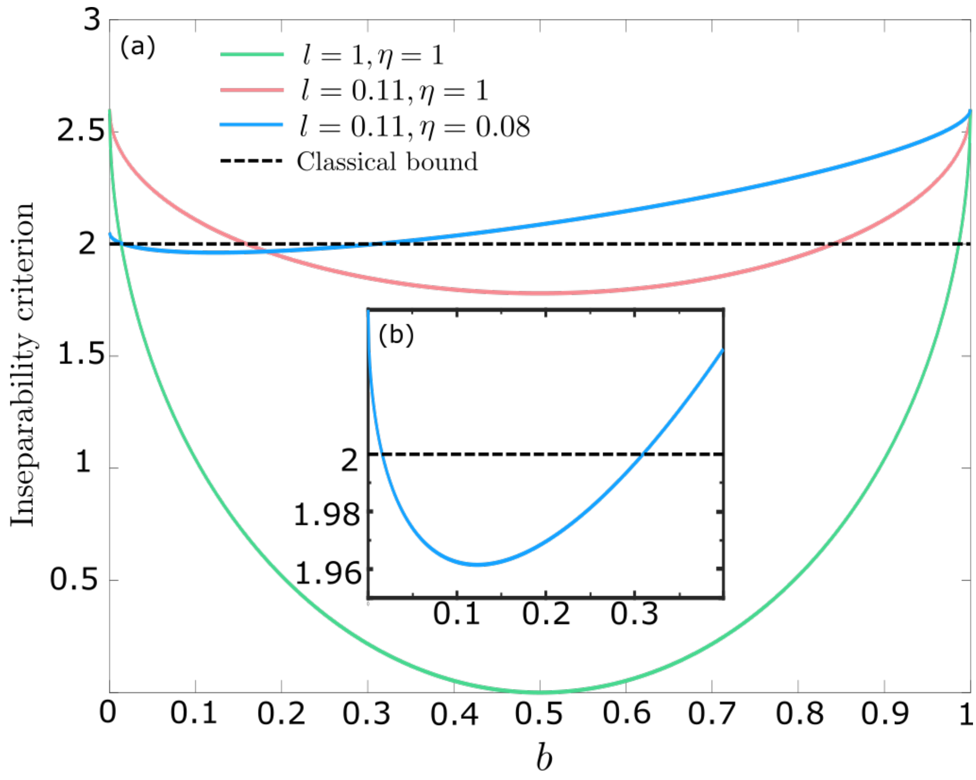

Figure 3.4: The inseparability criterion with weighting parameter b. The curves shown are for (a) no experimental loss and a perfect rephasing efficiency, l = 1 and η = 1; with experimental loss and perfect rephasing efficiency, l = 0.11 (see §4.5), η = 1; and (b) experimental loss and experimental efficiency, l = 0.11 and η = 0.08 (see Chapter 7).

3.4.2 The Optical Depth Model

A second model, called the 'optical depth model', was developed by Ledingham [96] to predict the gain, G, dependency of the spontaneously emitted fields. It uses fully quantized Maxwell-Bloch equations, to predict the variance in the ASE and RASE quadrature values for a two-level atomic system. Expressions for the variance in the amplitude $\hat{x}$ and phase $\hat{p}$ quadrature values, for both ASE and RASE fields, as a function of optical depth are

$$\begin{aligned}\langle \hat{x}_1^2 \rangle &= \langle \hat{p}_1^2 \rangle = 2e^{\alpha \mathrm{L}} - 1,\\ \langle \hat{x}_2^2 \rangle &= \langle \hat{p}_2^2 \rangle = 1 + 8\sinh^2\left(\frac{\alpha \mathrm{L}}{2}\right),\\ \langle \hat{x}_1 \hat{x}_2 \rangle &= -\langle \hat{p}_1 \hat{p}_2 \rangle = 2(1 - e^{\alpha L}),\end{aligned} \tag{3.10}$$

where optical depth αL is the natural logarithm of gain, and i=1,2 for the ASE and RASE fields respectively.

An expression for the gain dependency of the ASE variance, which accounts for loss, is found by combining Eq. (3.9) with Eq. (3.10). In §5.4 the gain dependency of the average ASE quadrature variance $\langle \hat{X}_1^2 \rangle$ is assessed, because the gain dependency of the two quadrature variances are the same ($\langle \hat{x}_1^2 \rangle = \langle \hat{p}_1^2 \rangle$). In the RASE experiment the vacuum variance was normalized to one, (see §5.3 and §6.2), and therefore, the gain dependency of the average variance can be expressed as

$$\langle \hat{X}_1^2 \rangle = l(2e^{\alpha \mathrm{L}} - 1) + (1 - l). \tag{3.11}$$

Using this relationship, the efficiency η of RASE can be modeled with optical depth. The rephasing efficiency is given by the ratio of signal quadrature variances after subtracting the vacuum variance,

$$\eta = \frac{\langle \hat{X}_2^2 \rangle - 1}{\langle \hat{X}_1^2 \rangle - 1}. \tag{3.12}$$

The efficiency will be independent of loss if it affects both fields equally. Therefore, the efficiency can approach 100 % when the optical depth is large enough, shown in Figure 3.5 (b).

In addition, the gain dependency of the inseparability curve minimum can be modeled. This is done by combining Eq. (3.10) with the analytical expression for the EPR-type operators in Eq. (3.8), giving

$$\begin{aligned} \langle (\Delta \hat{u})^2 \rangle + \langle (\Delta \hat{v})^2 \rangle = & 2b(2e^{\alpha L} - 1) \\ & + 2(1 - b)(1 + 8\sinh^2\left(\frac{\alpha \mathrm{L}}{2}\right)) \\ & + 8\sqrt{b(1 - b)}(1 - e^{\alpha L}). \end{aligned} \tag{3.13}$$

The experiment loss can be incorporated into this model in the same way as with Eq. (3.11). The gain dependency of the inseparability curve minimum is shown in Figure 3.5 (a). The position of the curve minimum is shown to decrease from classical boundary as the optical depth increases. This result suggests that the fields should be more non-classically correlated as the optical depth increases.

Modeling the efficiency of RASE with optical depth suggests that perfect rephasing should be possible when the optical density of the crystal is large enough. However, for an optically thick medium, some assumptions made in the modeling of the inseparability criterion begin to break down. The effects of gain dependent loss, for example, are not accounted for in the simplistic loss model (see §3.4.1).

One source of unavoidable gain dependent loss is the spatial distortion of the control pulses as the crystal becomes more optically thick. These distortions will affect the RASE field more significantly, compared to the ASE field, because the rephased field is dependent on a larger number of control pulses. The effect will be a deterioration in the efficiency of RASE with optical depth.

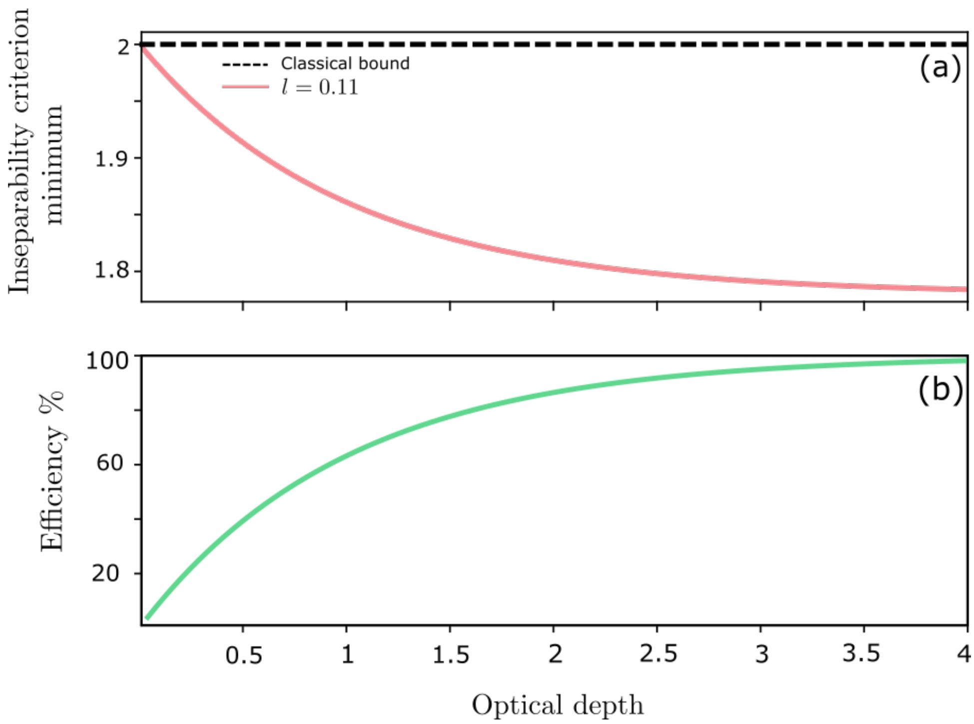

Figure 3.5: The theoretical (a) position on the inseparability curve minimum and (b) rephasing efficiency of RASE with optical depth, using l=0.11.

3.5 The Previous RASE Experiment

This thesis builds on the preliminary work done with RASE by Ferguson *et al.* [1] and Beavan *et al.* [47]. The pulse sequence used by Ferguson to measure four-level RASE is shown in Figure 3.6. The inversion pulse was applied on the $|0\rangle \leftrightarrow |3\rangle$ transition, and ASE was detected at frequency ω_{13}. The first and second rephasing pulses were applied on the $|2\rangle \leftrightarrow |3\rangle$ and $|1\rangle \leftrightarrow |4\rangle$ transitions respectively, and RASE was detected at a frequency ω_{24}.

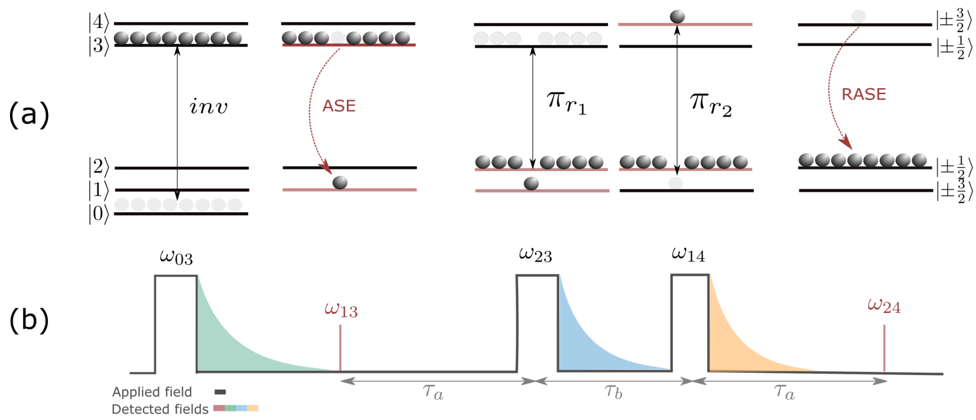

Figure 3.6: (a) Energy level representation of the four-level RASE pulse sequence used by Ferguson *et al.* [73]. The inversion pulse *inv* was applied on the $|0\rangle \leftrightarrow |1\rangle$ transition which corresponds to frequency ω_{01}, ASE was detected on the $|1\rangle \leftrightarrow |3\rangle$ transition, which corresponds to frequency ω_{13}, π_{r_1} was applied on the $|2\rangle \leftrightarrow |3\rangle$ transition, which corresponds to frequency ω_{23}, π_{r_2} was applied on the $|1\rangle \leftrightarrow |4\rangle$ transition, which corresponds to frequency ω_{14}, and RASE was detected on the $|2\rangle \leftrightarrow |4\rangle$ transition which corresponds to frequency ω_{24}. The Pr:YSO hyperfine levels are also labeled with their dominant spin quantum number m_s (see §2.1). (b) The corresponding temporal pulse sequence, where the free induction decay (FID) after the bright control pulses is shown.

In Ferguson's experiment, the two fields were detected using a heterodyne detection system. This approach allows the frequency components of the signal to be resolved, unlike with single photon detectors. Therefore, spatial filtering was not required and a co-propagating beam geometry was chosen. This greatly simplified the experiment design, and was not changed for this thesis (see Chapter 4 for details on the experiment setup).

Using this experiment design, Ferguson confirmed that ASE and RASE can be considered an inseparable state with a 98.6 % confidence level [1]. However, the gain dependency of the average ASE quadrature variance $\langle \hat{X}_1^2 \rangle$ did not agree with the theoretical model (see §3.4.2). The explanation given for this was a spatial mode mismatch between the beam on the first and second pass through the crystal.

The co-propagating beam geometry used by Ferguson is illustrated in Figure 3.7 (a). A lens is used to focus the beam on a mirror held below the crystal. If the mirror is positioned at the waist of the incoming beam, then the reflected beam will be spatially identical. In this case, the two beams will be matched inside the crystal. The two beams will be mismatched when the mirror is displaced from the waist of the incoming beam w_i, shown in (b). In this example, the mirror is displaced a distance Δm below the waist of the incoming beam, and therefore, the spatial mode sampled by the reflected beam is larger.

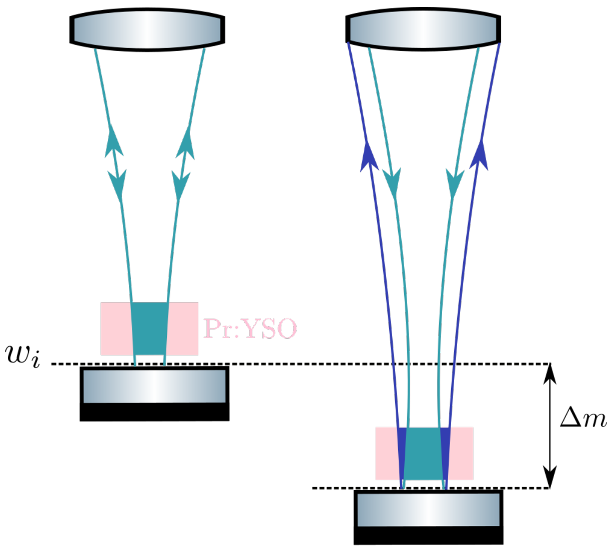

(a) Matched (b) Mismatched

Figure 3.7: Illustration of the co-propagating beam geometry used in Ferguson's RASE experiment, where the incoming beam was focused on the mirror below the crystal with a f = 15 cm lens. (a) When the waist of the incoming beam w_i is positioned on the mirror, the spatial mode sampled by the reflected beam is matched with the incoming beam. (b) When the mirror is displaced a distance Δm below the incoming beam waist, the spatial mode sampled by the reflected beam is mismatched from the incoming beam.

The theoretical gain dependency of the ASE quadrature variance is constructed from Eq. (3.11), which requires an estimation of the loss parameter l (see §3.4.1). In Ferguson's work, the sources of loss were two beamsplitters: 55/45 and 50/50 (R/T), which gave a loss parameter of 0.275. Detector inefficiencies and reflection losses were then incorporated on the 10% level. This reduced the loss parameter to 0.25, and therefore, 75% signal loss.

One source of loss, which was not accounted for in Ferguson's work, was the percentage overlap of the probe and local oscillator beam and at the detection system (see §4.4 for details). This overlap was measured to be 40% (see §4.5), and when taken into account reduced the loss parameter to a much smaller value of 0.11 (not accounting for reflection losses). In Figure 3.8 Ferguson's measurement of the ASE variance is compared to the two theoretical curves, i.e. using a loss parameter of 0.25 and 0.11 in Eq. (3.11). In both cases, the measured ASE variance was smaller than the theory predicted.

To calculate what fraction of the measured gain, G, the experimental ASE result corresponds to, the result was fitted to the form of the theoretical curve (Eq. (3.11)) with G as a free parameter

$$\langle \hat{X}_1^2 \rangle = l(2e^{G\times\alpha L} - 1) + (1 - l). \tag{3.14}$$

Using l = 0.11, the best fit was found with G = 0.5± 0.02. Therefore, the measured result corresponds to a gain which is 50 % of what the theory predicts. This result is physically impossible, and suggests that the discrepancy can't be the result of a spatial mode mismatch. This is verified in Chapter 5 by comparing the gain dependency for a matched and mismatched beam condition.

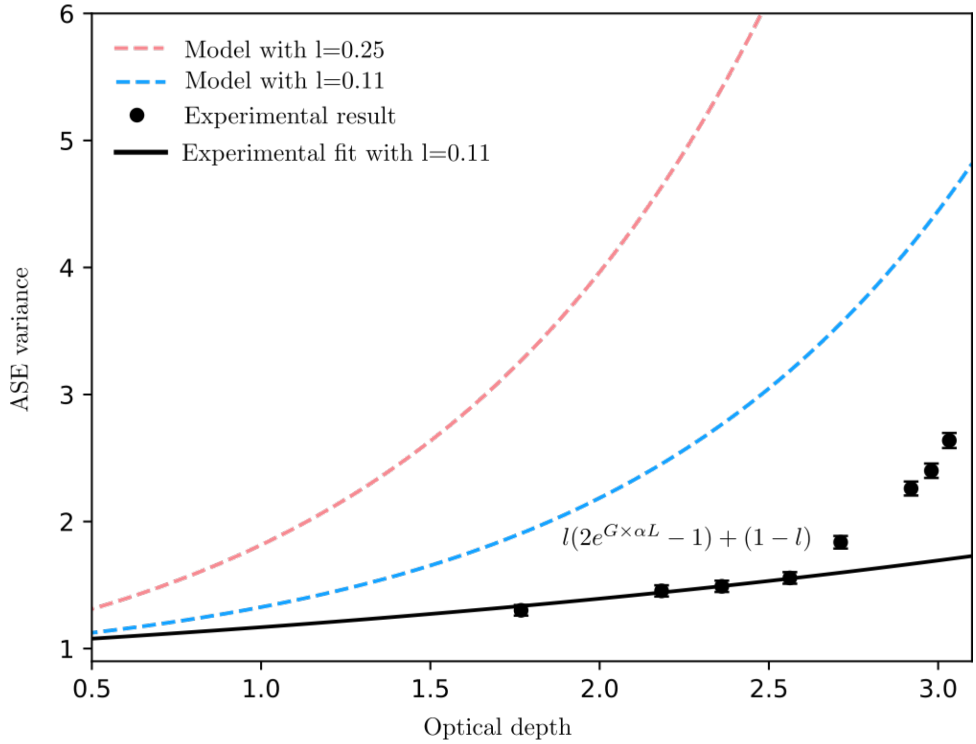

Figure 3.8: Experimental gain dependency of the average ASE quadrature variance $\langle \hat{X}_1^2 \rangle$ measured by Ferguson [73]. In Ferguson's work the model (see Eq. (3.11)) was constructed with a loss parameter of 0.25, and the beam area overlap at the detection system was not accounted for as a source of loss. Accounting for the beam area overlap, which was measured to be 40%, the loss parameter was reduced to 0.11 (not including reflection losses). To calculate what fraction of the gain the ASE result corresponds, to the experimental result was fitted to the model with G as a free parameter and l=0.11 (see Eq. (3.14)).

3.6 Summary

In this chapter the rephased amplified spontaneous emission (RASE) protocol was introduced. The RASE protocol works by creating a collective atomic state across an ensemble of rare-earth ions. This state is heralded when amplified spontaneous emission (ASE) is detected. A rephased optical field (RASE) can then be retrieved after a controlled delay time using photon echo techniques.

The most straightforward implementation of RASE is with a two-level atomic system. However, the system is inherently noisy, because the small quantum fields are spectrally identical to the bright control pulses. This motivated the development of a RASE using a four-level system, where the small quantum fields are spectrally distinct from the control pulses.

In addition, using a four-level system, storage times on the order of 1 second can be engineered, which is the memory requirement for large-scale quantum communication (see §1.6). This was achieved by shifting the collective atomic state from the optical to a longer-lived ground hyperfine transition between the two rephasing pulses.

In this work, the inseparability criterion was the metric used to quantify entanglement between the emitted fields of light. This metric evaluates the cross-correlation between the amplitude and phase quadratures of light. When either is non-zero, a non-linear inseparability curve will be observed. When this correlation is non-classical, the curve minimum will be bound between zero and two.

To predict the efficiency of RASE two models were introduced: the loss model and optical depth model. In conjunction, they were used to show that RASE should meet the efficiency threshold of a quantum repeater, $>90\%$, when the optical depth exceeds 2.5.

Lastly, the work done by Ferguson, which is relevant to this thesis, was discussed. Most notably, Ferguson observed that the gain dependency of the ASE quadrature variance did not agree with the theory. The explanation for this was a spatial mode mismatch between the two passes of the beam through the crystal. To assess this claim, the spatial mode matching inside the crystal was precisely controlled in Chapter 5.

Experimental Setup

To achieve large-scale quantum communication, a quantum repeater is necessitated. In Chapter 3 an integrated quantum repeater protocol was introduced which is based on rephased amplified spontaneous emission (RASE). In this work RASE performed in the the rare-earth ion-doped crystal Pr^{3+}:Y_2SiO_5, where the storage times required for quantum repeater can be engineered (see §2.2.1).

In this chapter, the experiment setup used to perform RASE, as well as the four level echo experiment (see Chapter 6), is illustrated in Figure 4.1. To fully leverage the long coherence times available in rare-earth crystals, the crystal must be held close to liquid helium temperature (see §2.2). To accomplish this, the crystal was cooled using the 'bucket cryostat' system outlined in §4.2. The ${}^3H_4 \rightarrow^1 D_2$ optical transition is then addressed by sending a 606 nm laser to the cooled crystal.

For all measurements in this thesis, the magnetic field was zeroed using xyz-correction coils. To address each of the optical transitions between the ground and excited electronic states, the laser was frequency modulated using the experiment setup outlined in §4.2. However, even when the effects of optical broadening have been removed, multiple subgroups will be resonant with a single applied laser (see §2.3). To simplify the RASE experiment, the ensemble was prepared such that only a single subgroup is resonant with all optical transitions used in RASE (see §4.3).

The quadrature values of the emitted light were then measured to confirm entanglement (see §3.3). In this work the amplitude and phase quadratures are measured simultaneously using heterodyne detection, outlined in §4.4. Another focus of this thesis was understanding the affect classical noise has on the efficiency of RASE. A precise way to characterize the classical noise in the RASE experiment, is to compare the experimental and theoretical inseparability curves. To construct the theoretical curve, all sources of loss in the experiment must be accounted (see §4.5).

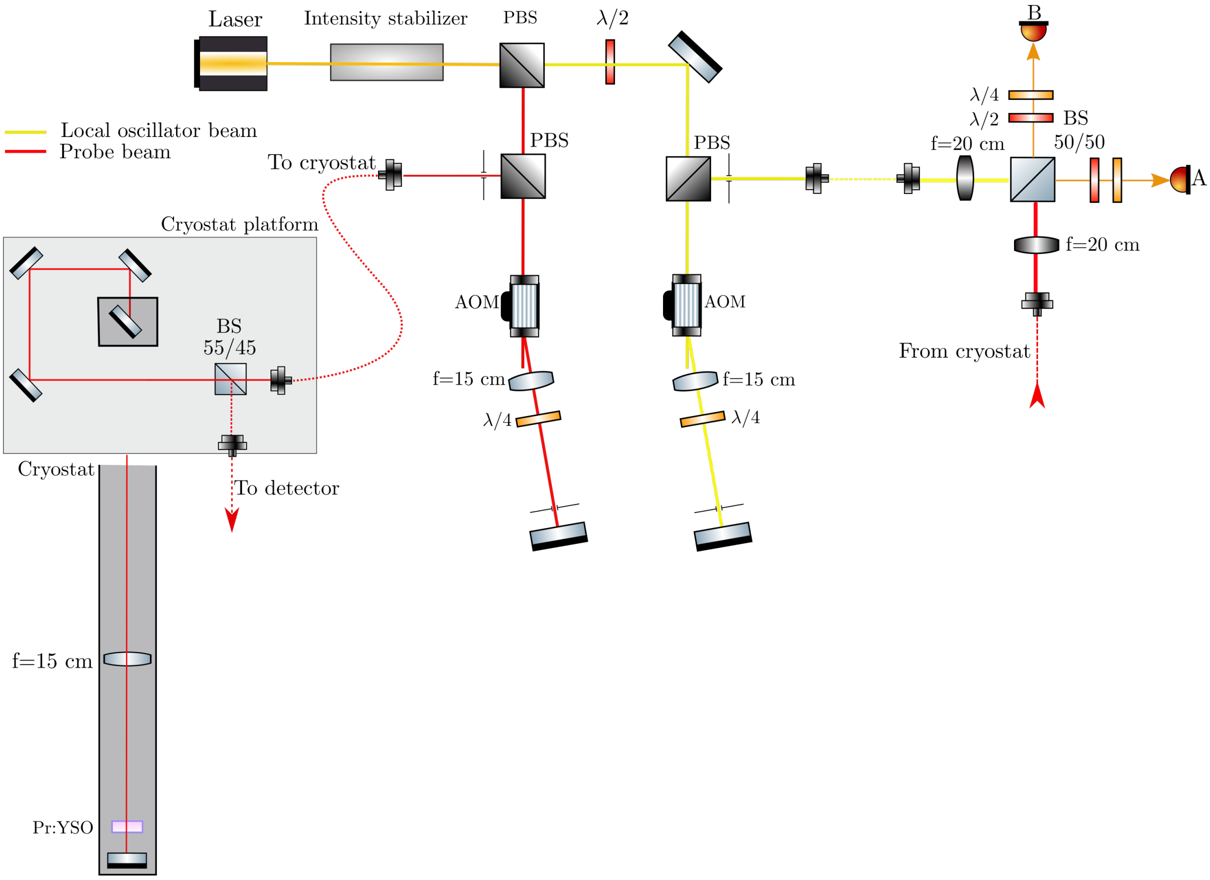

Figure 4.1: The experimental setup used for the RASE, and four level echo experiments, where $\frac{\lambda}{2}$ and $\frac{\lambda}{4}$ refer to half-wave plates and quarter-wave plates respectively. The laser was tuned to 606 nm and split into local oscillator (yellow), and probe (red) beam, which were both frequency modulated using an acousto-optic modulator (AOM). The local oscillator was sent to the detection system, while the probe was sent to the cryostat platform. The probe was then double-passed through the crystal, and fiber coupled to the detection system. The probe and local oscillator beams were phase stabilized with a pair of wave plates before being superimposed at the detection system.

4.1 Cryostat

The cryostat used in this thesis was developed by Ferguson with the specific requirements of the RASE experiment in mind [73]. Namely, the cryostat was thermally and mechanically stable for the large timescales, typically hours, required to perform the experiment.

The cryostat system is illustrated in Figure 4.2 (a), and is comprised of 3 layers: an outer vacuum space, intermediate liquid helium space and high purity gaseous helium sample space. The sample holder was held inside a sample rod, which could be removed when disassembling the experiment. The light was free-space coupled into the sample rod and focused onto a mirror below the crystal. The reflected beam then followed the same path to the top of the cryostat.

One aim of this thesis was to verify if a spatial mode mismatch, between the input and reflected beam, was a source of loss in the experiment. To investigate this, a spatial mode mismatch was engineered by adjusting the position of the mirror relative to the crystal (see §5.1). To achieve this, without disassembling the cryostat, the sample holder developed by M. Berrington [92] was modified to incorporate a piezo-driven vertical positioner or 'attocube', shown in (b). The mirror was mounted on top of the attocube, shown in (c), allowing the position from the crystal Δc to be adjusted.

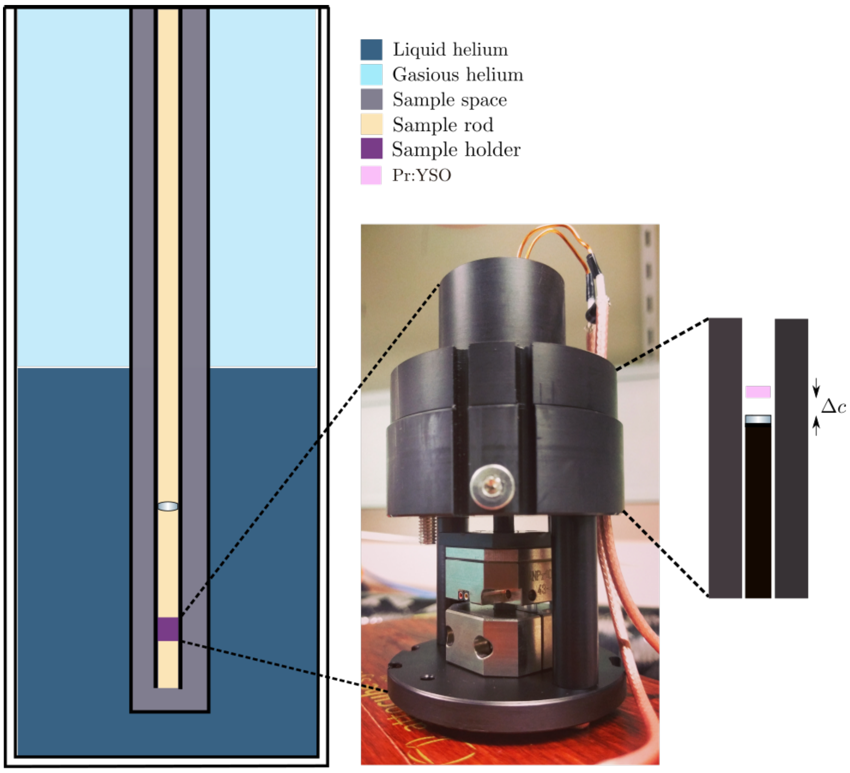

(a) (b) (c)

Figure 4.2: Illustration of the cryogenic system used for the RASE experiment. (a) Cross section of the 'bucket cryostat' used to cool the crystal, (b) the sample holder, which was developed by M. Berrington [92], modified to include an attocube, (c) the mirror below the crystal was mounted on top of the attocube, allowing the position from the crystal Δc to be adjusted without disassembling the cryostat.

4.2 Optics

A dye laser (Coherent 699), which was tuned to λ=605.977 nm and frequency stabilized to sub-kilohertz linewidth [97], was used in this work. The full path of the laser is shown in

Figure 4.1. First the beam was intensity stabilized, and was then separated into a probe and local oscillator beam with a polarizing beam splitter (PBS). The beams were then modulated by $\mathcal{O}$(10 MHz) with a double-pass through an acousto-optic modulator (AOM).

The local oscillator beam was then fiber-coupled and sent directly to the detector setup, while the probe was sent to the cryostat platform. At the cryostat platform the probe beam was split with a 55/45 (R/T) beamsplitter (BS), and the transmitted beam was sent to the crystal.

Inside the cryostat the probe beam was focused with a 15 cm lens onto the mirror below the crystal. When the mirror is positioned correctly, the beam will be reflected through the same area of the crystal. After interacting with the crystal, any signals emitted will be in the same spatial mode as the probe beam because the laser spot size is much larger than λ^3.

The probe beam then arrives back at the 55/45 (R/T) beamsplitter (BS), and the reflected beam is fiber coupled and sent to the detection system. At the detection system the local oscillator, and signal carrying probe beam, are superimposed on photodetectors A and B for balanced heterodyne detection (see §4.4).

4.3 Ensemble Preparation

In §2.3 spectral holeburning was introduced as method to optically address the transitions between the ground and excited hyperfine levels of Pr:YSO. This involved optically pumping the ions of interest into a non-resonant 'storage state'. However, in the Pr:YSO crystal nine resonant subgroups will exist for a single optical transition, between the ground and excited state hyperfine levels.

In the four level echo (see §6.1) and RASE experiment (see Figure 6.5), the control pulses are applied at three frequencies: ω_{13}, ω_{23} and ω_{14}. Only one subgroup will be resonant with all three frequencies, with the others becoming a source of unwanted noise. To remove this, a single subgroup was isolated before performing the two experiments

To isolate a single subgroup, all six unique hyperfine levels must be hit with a pumping sequence. This was done by applying a laser at ω_{23}, ω_{14} and ω_{05}, and sweeping ± 1 MHz, illustrated in Figure 4.3 (a). After multiple iterations, any unwanted subgroups will be pumped into a ground state which is off-resonant, or 'dark', with any of the laser frequencies used in the two experiments.

Once a single subgroup has been isolated, the hyperfine ground states will be equally populated. Before performing the RASE and four level echo experiment, the isolated subgroup was initialized in the state $|0\rangle$, shown Figure 4.3 (b). This was achieved by sweeping a laser ± 1 MHz, centered at ω_{23} and ω_{14}.

The inverting pulse *inv*, at the beginning of the RASE experiment, was then applied to the population initialized in state $|0\rangle$. In the four level echo experiment, the $\frac{\pi}{2}$ pulse was applied on a narrow feature initialized in state $|1\rangle$, shown in Figure 4.3 (c). This feature was created by applying a laser at ω_{05}, and sweeping $\pm$ 100 kHz. The decayed population was then pumped out of $|2\rangle$ by simultaneously applying a ± 1 MHz sweep centered at ω_{23}.

Altogether, ensemble preparation took $\sim$ 90 ms, and was repeated before each run of the experiment.

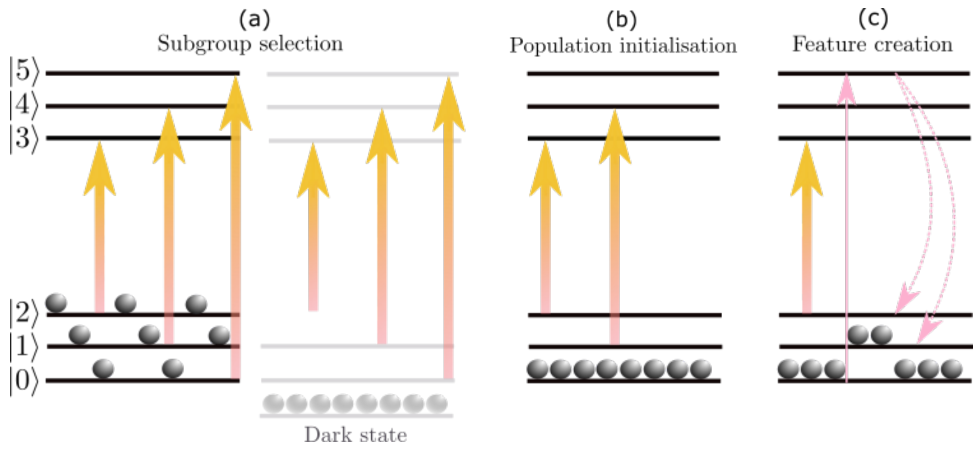

Figure 4.3: The ensemble preparation method for the four level echo and RASE experiments, where the thicker arrows indicate $\pm$ 1 MHz laser sweep. (a) A single subgroup was isolated, for both the four level echo and RASE experiments, using optical pumping (b) The isolated subgroup was initialized in the ground hyperfine state $|0\rangle$ for both the four level echo and RASE experiments. (c) A narrow feature was initialized in the second hyperfine ground state $|1\rangle$ for the four level echo experiment.

4.4 Detection

For the RASE experiment, we are interested in measuring fluctuations in the emitted fields at the quantum level. The amplitude of the light fields could be measured with a direct measurement of intensity. However, quantum fluctuations are typically much smaller than the noise sources on a simple photon detector. The solution is to use a balanced detection method, such as heterodyne or homodyne detection, to detect down at the quantum level.

For heterodyne detection the signal is observed as a beat between the probe and local oscillator beams, which are set to different frequencies. This is not the case for homodyne detection, where the probe and local oscillator frequencies are identical. The beat will scale linearly with the amplitude of the local oscillator, and for a sufficiently intense beam, it is possible to elevate the quantum fluctuations above the detector noise. This gives a measurement of the phase and amplitude quadratures of light, at the quantum level, which are required to use the inseparability criterion metric for entanglement (see §3.3). In the RASE experiment, where the two quantum fields are emitted at different frequencies (see §3.5), it was more convenient to hold the local oscillator at a constant frequency using heterodyne detection.

4.4.1 Homodyne Detection

The amplitude and phase quadratures of light can be measured at the quantum level using either heterodyne and homodyne detection. In this section homodyne detection is used to illustrate the general principle of both detection methods, however, a more complete description can be found in textbooks such as Hans-A. Bachor [98].

One way to illustrate homodyne detection, shown in Figure 4.4, is to describe the probe and local oscillator beams with annihilation operators $\hat{a}$ and $\hat{b}$, respectively. Both beams will contain coherent light and quantum fluctuations. When the local oscillator beam is bright enough, $\hat{b}$ can be considered a classical state. Therefore, $\hat{b}$ can be replaced with the complex amplitude of a coherent state β.

The output beams, which are described by operators $\hat{c}$ and $\hat{d}$, are a superposition of $\hat{a}$ and β, where the incoming and reflected beam will have a $\frac{\pi}{2}$ phase shift. This relative phase shift is absorbed into a ϕ term on the local oscillator field, $\beta \rightarrow |\beta|e^{i\phi}$. The relationship between the incoming and outgoing beam can be summarized as

$$\begin{bmatrix} \hat{d} \\ \hat{c} \end{bmatrix} = \frac{1}{\sqrt{2}} \begin{bmatrix} -e^{i\phi} & 1 \\ e^{i\phi} & 1 \end{bmatrix} \begin{bmatrix} |\beta| \\ \hat{a} \end{bmatrix}. \tag{4.1}$$

The quantity of interest is the difference in photocurrent from detectors A and B, i_{AB}. This subtraction will remove any classical fluctuations which are on the local oscillator beam, and allow measurements which are limited by the quantum fluctuations of the probe beam, otherwise known as 'shot-noise-limited' detection.

The current difference is proportional to the difference in photon number arriving at the detectors

$$\hat{i}_{AB} \propto \hat{n}_B - \hat{n}_A \tag{4.2}$$

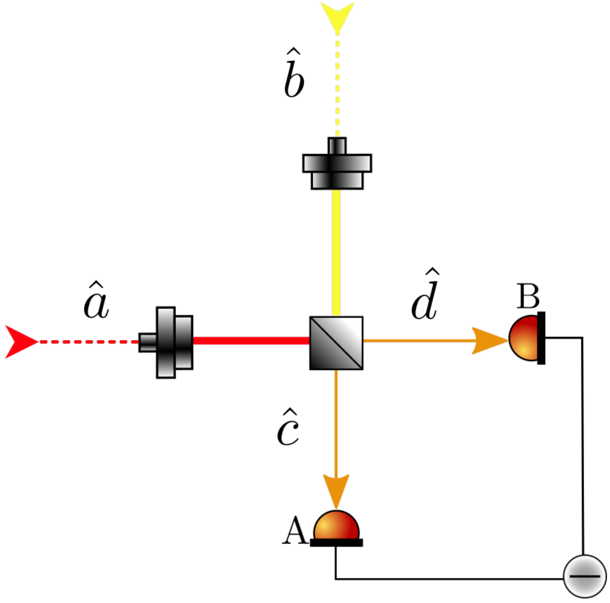

Figure 4.4: Illustration of balanced homodyne detection system. Where annihilation operators $\hat{a}$ and $\hat{b}$ represent the incoming probe and local oscillator beams respectively. The outgoing beams, which arrive on detectors A and B, are represented by annihilation operators $\hat{c}$ and $\hat{d}$ respectively. The subtracted photocurrent will be limited by the quantum fluctuations on the probe beam, allowing 'shot-noise-limited' detection.

where n_A and n_B are the number of photons hitting detectors A and B, respectively. In terms of the output beams, they can be expessed as

$$\begin{aligned}\hat{n}_A &= \hat{c}^\dagger \hat{c} \\ \hat{n}_B &= \hat{d}^\dagger \hat{d}\end{aligned} \tag{4.3}$$

The number of photons hitting the two detectors can be expressed in terms of the input beams using Eq. (4.1), which gives

$$\begin{aligned}\hat{n}_A &= \frac{1}{2}[(|\beta|e^{-i\phi} + \hat{a}^\dagger)(|\beta|e^{i\phi} + \hat{a})] \\ &= \frac{1}{2}[|\beta|^2 + |\beta|\hat{a}e^{-i\phi} + |\beta|\hat{a}^\dagger e^{i\phi} + \hat{a}^\dagger \hat{a}]\end{aligned} \tag{4.4}$$

$$\begin{aligned}\hat{n}_B &= \frac{1}{2}\left[(-|\beta|e^{-i\phi} + \hat{a}^\dagger)(-|\beta|e^{i\phi} + \hat{a})\right], \\ &= \frac{1}{2}[|\beta|^2 - |\beta|\hat{a}e^{-i\phi} - |\beta|\hat{a}^\dagger e^{i\phi} + \hat{a}^\dagger \hat{a}].\end{aligned} \tag{4.5}$$

When the photon numbers are subtracted, the cross-terms survive and the difference in current can be expressed as

$$\hat{i}_{AB} = |\beta|(\hat{a}e^{-i\phi} + \hat{a}^{\dagger}e^{i\phi}). \tag{4.6}$$

The subtracted current will, therefore, give measure of the phase and amplitude quadratures of light when

$$i_{AB} = |\beta| \begin{cases} \hat{p}, & \text{if } \phi = \frac{\pi}{2} \\ \hat{x}, & \text{if } \phi = \pi, \end{cases} \tag{4.7}$$

where the amplitude and phase quadratures are expressed as

$$\begin{aligned} \hat{x} &= \hat{a} + \hat{a}^{\dagger}, \\ \hat{p} &= -i(\hat{a} - \hat{a}^{\dagger}). \end{aligned} \tag{4.8}$$

Therefore, a measurement of the phase and amplitude quadrature can be made when the phase between the probe and local oscillator beams are $\frac{\pi}{2}$ and π, respectively. This derivation also highlights the key strength of balanced detection, showing how the quadrature values are amplified by the local oscillator beam.

4.4.2 Heterodyne Detection

Using heterodyne detection the signal will be detected as a beat betweeen the probe and local oscillator beams, and therefore, the relative phase between the two beams is constantly changing. Unlike homodyne detection, this means both quadratures will be sampled at once, instead of one quadrature at a time.

To confirm that detection system was shot-noise-limited, the variance in the local oscillator beam was measured with local oscillator power. The variance was measured at the expected beat frequency of ASE and RASE, 12.6 and 7.0 MHz respectively, shown in Figure 4.5. In both cases, the variance was shown to increase linearly until a power of the local oscillator beam 2 mW, where the measurement saturated. Therefore, to amplify the quadrature measurements maximally, the local oscillator beam power was set to just below the saturation point of the two signals. This was chosen as 1.8 mW for all measurements performed in this thesis.

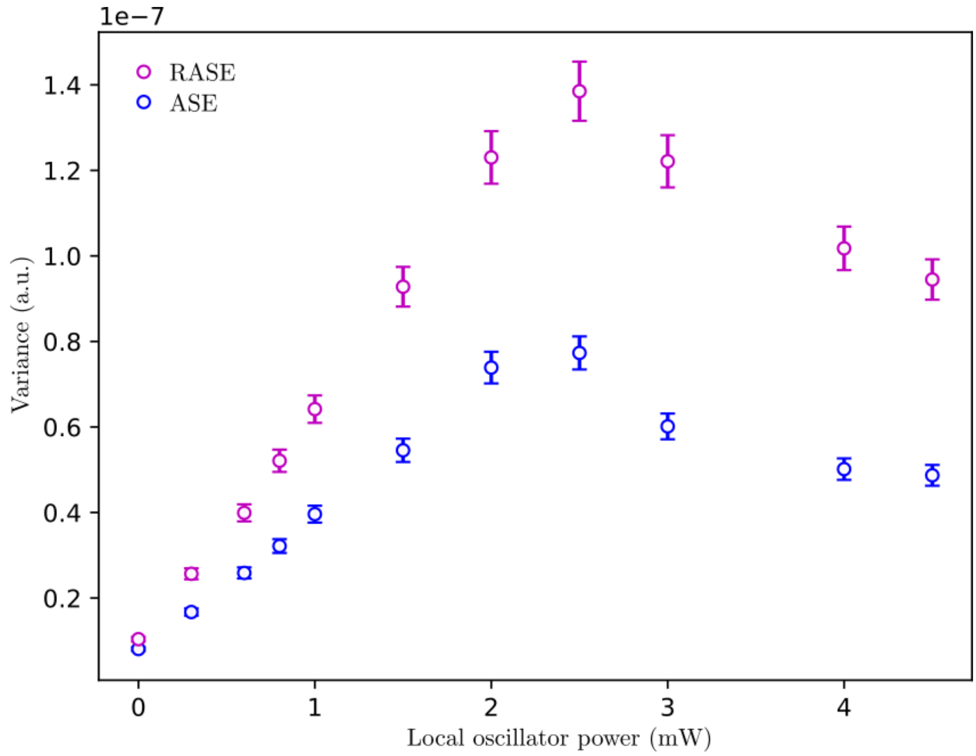

Figure 4.5: Variance in the photocurrent i_{AB} with local oscillator power using heterodyne detection. The relationship is characterized with the beat frequency set to the expected beat frequency of ASE and RASE, 12.6 and 7 MHz respectively.

4.4.3 Phase Correction

Because heterodyne detection is phase sensitive, the phase offset between the local oscillator and probe beam should be controlled. This was accomplished by clocking the RF sources for the probe and local oscillator beams together. It was also necessary to clock the data acquisition system with the two RF sources.

It was shown by Ferguson that the phase was stable over a single shot of the experiment to less than 1°. In addition, in the same collection window the phase noise on the laser was also less than 1° [73].

However, the phase offset varied randomly between shots, requiring digital phase correction in post-processing. The phase correction used in this experiment was implemented by Ferguson, and more information can be found in [73]. In general, two phase reference pulses were added to the end of the experiment pulse sequence (see §6.1.3), at the expected beat frequency of ASE and RASE, which was 12.6 and 7 MHz respectively. This was used to correct for the global phase drift of the interferometer and for a timing jitter introduced by the difference in clock frequency between the RF oscillators and the oscilloscope.

4.5 Experiment Loss

The inseparability criterion is dependent on the signal loss in the experiment (see §3.4). Therefore, to model the inseparability criterion, and compare to the experimental result, all sources of experimental loss must be accounted for.

There are two main sources of loss in the RASE experiment: beamsplitters and an imperfect overlap, between signal and local oscillator beams, at the detection system. Reflections from optical surfaces will also contribute to experimental loss and was minimized by using anti-reflection coated optics.

The beam area overlap at the detectors can be quantified by measuring the visibility v of the detection system. The visibility was measured by decreasing the local oscillator power to match the probe, and measuring the beat at the expected beat-frequency of ASE, which was 12.6 MHz. The visibility is related to the amplitude of the measured beat by

$$v = \frac{V_{max} - V_{min}}{V_{max} + V_{min}}, \tag{4.9}$$

where V_{max} and V_{min} are the maximum and minimum voltage of the beat, the visibility at the ASE detection frequency was measured as 90%. The beam area overlap was quantified using the relationship between the measured visibility, and the intensity of the probe I_{pr} and local oscillator I_{lo} beams:

$$v = \frac{2\sqrt{I_{lo} I_{pr}}}{I_{lo} + I_{pr}}, \tag{4.10}$$

which states that when intensity of the probe and oscillator beams are the same the visibility will be 100%. Therefore, to calculate the beam overlap the local oscillator intensity was set to 1 and the probe was varied from 0 to 1. In Figure 4.6 a beam overlap of 40% is shown to correspond to a visibility of 90%.

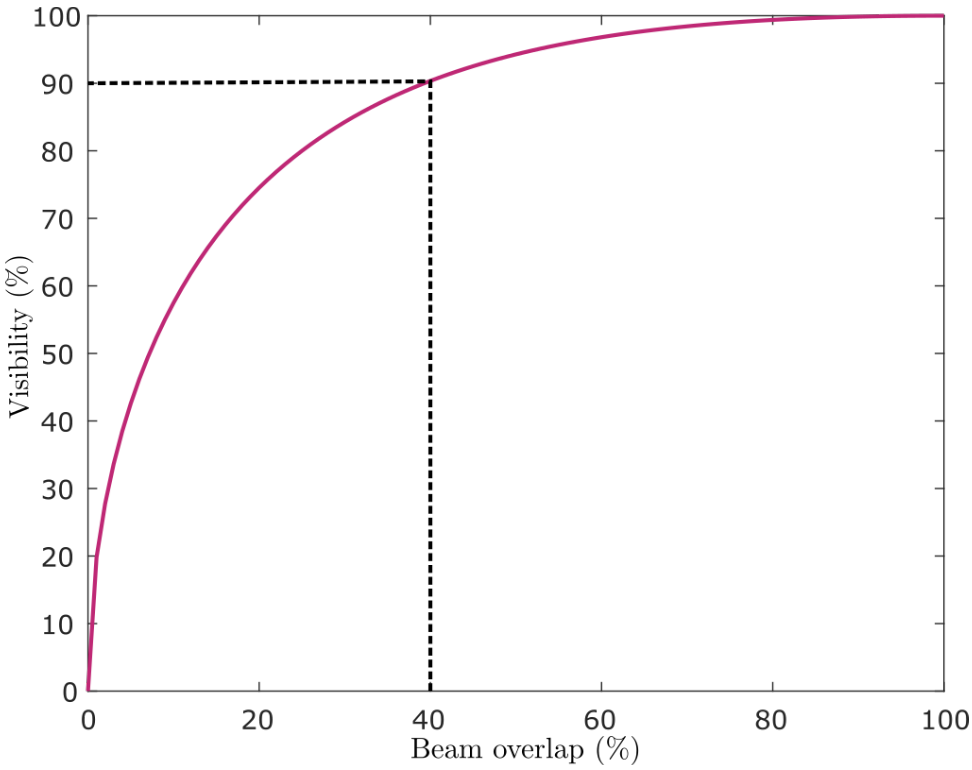

Figure 4.6: Relationship between the visibility of the detection system and overlap between local oscillator and probe beams at the detector. The experimental visibility was measured to be 90% which corresponds to a beam overlap of 40%.

The beam area overlap was included in the calculation of external loss parameter l. Along with this, loss was also introduced when the signal passed through two beam splitters: 55/45 (R/T) at the signal fiber collection port, and 50/50 at the detection system. Therefore, in total, the loss parameter for the RASE experiment was $l = 0.5 \times 0.55 \times 0.4 = 0.11$, i.e. 89% signal loss. This level of loss was incorporated in the modeling of the inseparability criterion in §3.4 and Chapter 7, as well the model for the gain dependency of the ASE quadrature variance in §5.4.

4.6 Summary

In the RASE experiment, the rare-earth ion-doped crystal Pr:YSO was held close to liquid helium temperature to fully leverage the coherence properties of the material. This was achieved using an exchange-gas-cooling 'bucket' cryostat. The optical transitions between the hyperfine levels of the crystal were then addressed by frequency modulating a dye laser tuned to 605.977 nm. The emitted fields were measured using heterodyne detection system, which was shot-noise-limited at the beat-frequency of the two signals. Lastly, the level of loss in the RASE experiment was shown to be 89%, which translates to loss parameter of $l = 0.11$.

Chapter 5

Gain Dependency of Amplified Spontaneous Emission

In Chapter 3 a repeater protocol based on rephased amplified spontaneous emission (RASE) was introduced. This was a promising approach to a building a repeater because RASE integrates two key components: an entangled light source and quantum memory.

For RASE to perform at the efficiency level required for a repeater, exceeding 90%, the protocol must operate at an optical depth of 2.5 (see §3.4.2). However, at these large optical densities the assumptions built into this result are expected to break down. For example, one assumption is that the signal loss in the experiment is constant with optical depth. However, as the crystal becomes more optically dense the control pulses will become more distorted, creating a source of gain dependent loss. When distortion is significant, the efficiency performance of RASE will begin to deteriorate, instead of improve, with optical depth (see §3.4.2 for a full discussion). Therefore, in order for RASE to operate at the large optical densities required for a repeater, the RASE experiment must be designed to correct the effects of mode distortions. To implement a correction technique, an in-depth understanding of how and when mode distortions become significant is required.

The average ASE quadrature variance $\langle \hat{X}_1^2 \rangle$ is purely dependent on the optical depth and sources of loss in the experiment (see Eq. (3.11)). Comparing the experimental gain dependency to the theoretical model should, therefore, give a good indication of when gain dependent loss, and therefore mode distortions, become significant in the RASE experiment. The effect of any gain dependent loss, of course, will be the experimental result deviating the the theoretical curve.

At present, the theoretical gain dependency of the average ASE quadrature variance has not been verified experimentally [73]. Instead, the ASE quadrature variance was shown to correspond to 50% of the gain predicted by the model. A spatial mode mismatch in the RASE experiment was proposed as the reason for this discrepancy (discussed in detail in §3.5). This claim is evaluated in this chapter, by deliberately engineering a spatial mode mismatch inside the crystal (see §5.1).

The ASE signal, and corresponding gain created on the ASE transition, were then measured individually, i.e. using different pulse sequences, for a matched and mismatched spatial mode condition. The pulse sequence used to directly probe the gain on the ASE transition, and the method used to calculate the gain, is illustrated in §5.2.1. Similarly, the pulse sequence used to measure the ASE signal is illustrated in §5.2.2. The method used to calculate the average ASE quadrature variance from the ASE signal is then outlined in §5.3. Finally, the experimental gain dependency of the average ASE quadrature variance, for the matched and mismatched condition, are compared to the theoretical model in §5.4. Using this approach, the matched result is used as a control to confirm that any deviation from the theoretical result is the effect of a spatial mode mismatch.

5.1 Beam Matching Configurations

In the RASE experiment the probe beam passed through the crystal twice. On the first pass the beam was focused on the mirror below the crystal. The reflected beam then followed the same path to the top of the cryostat (see §4.2). The beams were 'matched' spatially if they passed through the same area of the crystal on both passes.

The beams were deliberately mismatched to test whether this affected the gain dependency of the ASE quadrature variance. This mismatch was engineered by displacing the waist of the incoming beam from the mirror. The percentage area overlap between the incoming and outgoing beam was then quantified by measuring the beam diameters, d_i and d_o respectively, at the top of the cryostat.

The beams were deliberately mismatched to test whether this affected the gain dependency of the ASE quadrature variance. This mismatch was engineered by displacing the waist of the incoming beam from the mirror. The percentage area overlap between the incoming and outgoing beam was then quantified by measuring the beam diameters, d_i and d_o respectively, at the top of the cryostat.

The beam diameter was measured using a knife-edge technique, taking the distance between 10% and 90% of the maximum beam power. When the two beams were matched in the crystal, the diameter of the input and output beams were equal, d_i=d_o=500$\pm$10 μm. When the two beams were mismatched in the crystal, the diameter of the output beam was 200 μm larger than the diameter of the input beam.

The percentage area overlap of the two beams, inside the crystal, was calculated using Gaussian beam optics and the schematic in Figure 5.1. The matched case is shown in (a), where the waist of the incoming beam w_i is positioned on the mirror. In this case the beam area overlap inside the crystal is 100%. The mismatched case is shown in (b), where the waist of the incoming beam is displaced above the mirror by Δm.

Using the schematic in Figure 5.1, a 200 μm difference in beam diameter at the top of the cryostat, $d_o - d_i$, was found to correspond to a 12 $\pm$ 2 mm displacement in the mirror from the waist of the incoming beam. The refractive index of the crystal was not accounted for in this calculation, being that for yttrium orthosilicate this value is close to one. Knowing this displacement, the diameter of the output beam at the crystal can be calculated. This calculation requires the distance between the mirror and the crystal Δc to be accounted for, which was 3$\pm$1 mm. This gave an output beam which was 1.7 times larger than the diameter of the input beam at the crystal, which translates to a beam-area overlap of 35 $\pm$ 10%.

With the mismatched case known to correspond to the beam-area overlap of 35%, the effect this mismatch has on gain dependency of the ASE quadrature variance can now be assessed. To confirm whether a deviation from the theoretical dependency (see §3.4.2) is the result of a spatial mode mismatch, the matched case, with a beam-area overlap of 100%, is used as a control.

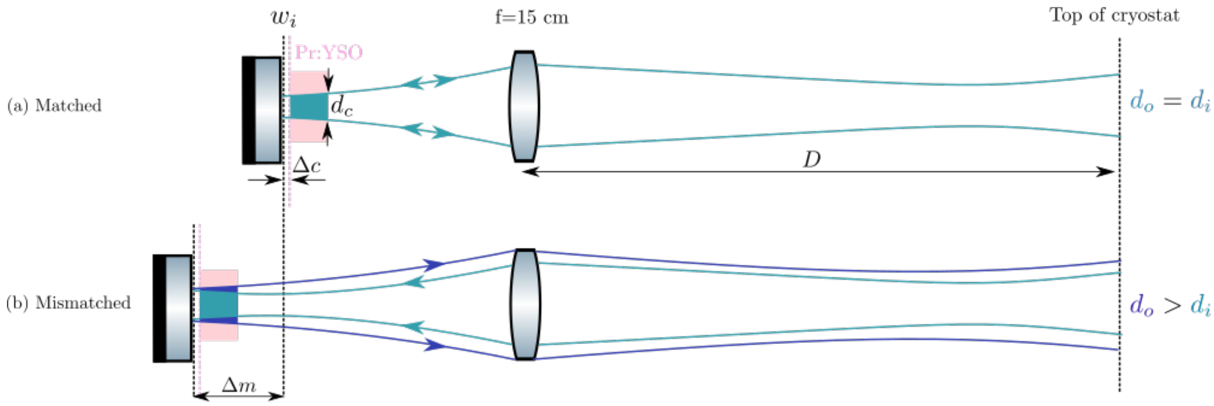

Figure 5.1: Schematic (not to scale) used to calculate the percentage area beam overlap, between the two passes of the beam, at the crystal. The percentage beam area overlap is the ratio of the beam diameter at the crystal squared d_c^2, which is assumed constant across the length of the crystal, for the ingoing and outgoing beams. To calculate d_c the diameter of the ingoing and outgoing beams, d_i and d_o respectively, were measured at the top of the cryostat. The distance from lens, held in the sample rod (see §4.1), to where the beams were characterized above the cryostat D was 1 meter, note that in this region the beam is not expected to be collimated. The distance D was measured from outside the sample rod and had an associated uncertainty of 10 cm. The 'matched' beam configuration is shown in (a), where the mirror is positioned at the waist of the incoming beam w_i, and therefore d_c is the same for both beam passes. The 'mismatched' configuration is shown in (b), where the mirror is displaced from the waist of the incoming beam by Δm, and therefore d_c is different for each pass of the beam. In the experiment d_o was measured larger than d_i, and therefore, the mirror is shown displaced below the incoming beam waist. In both cases the crystal is displaced a distance Δc=3±1 mm above the mirror.

5.2 ASE and Gain Measurements

In this section, the pulse sequences used to measure the ASE signal, and corresponding gain created on the ASE transition, are outlined. For the gain measurement, the *average* gain across the ensemble is calculated using the method detailed in §5.2.1. The spectral profile of the ASE field is the compared for the mismatched and matched beam configurations (see §5.1) in §5.2.2.

5.2.1 Characterizing Gain

In the RASE protocol (see Chapter 3), an inverting pulse is used to create gain G on the ASE transition which heralds amplified spontaneous emission. In this work, the *average* gain of the ensemble was measured by constructing a gain profile.

The gain profile was constructed with the pulse sequence shown in Figure 5.2. The inversion pulse *inv* used for the direct gain measurement, and RASE experiment, were identical: the amplitude profile was shaped by convolving a top-hat and Gaussian function, the pulse was centered at frequency ω_{03} (see Figure 3.6), and chirped with a 300 kHz bandwidth for 8 μs duration.

Figure 5.2: Temporal pulse sequence used for the direct gain measurement. The ensemble was initialized in the ground state $|0\rangle$, using the ensemble preparation method outlined in §4.3. The amplitude profile of the inversion pulse *inv* was shaped by convolving a top-hat function with a Gaussian function. The inversion pulse was centered at frequency ω_{03} (see Figure 3.6), and chirped with a 300 kHz bandwidth for 8 μs duration. A delay time of a=3.5 μs was included before the probe, which was applied at ω_{13} for duration of b=10 μs. To construct the gain profile the probe was stepped in $\pm$50 kHz increments around ω_{13}.

The delay time a, and probe pulse duration b, were chosen such that the gain was probed in the same temporal window that ASE is detected over in the RASE experiment (see §6.1.3). Therefore, the weak probe was applied for 10 μs, following a 3.5 μs delay time.

To create the gain profile the probe frequency was stepped in $\pm$ 50 kHz increments around the ASE transition frequency ω_{13}. A measurement of the background gain, i.e. with the inversion pulse amplitude set to zero, was taken with the probe frequency set to ω_{13}. For each probe frequency the peak gain was normalized to the background gain value.

Next, the gain profile was windowed to ensure the gain was calculated in the same window as the ASE variance. This required the gain profile to be multiplied with an Fourier transform of an apodizing function. For more details on the windowing process see §6.2.

The gain profile was then integrated over to give the average gain of the ensemble. To follow convention, the optical depth value αL is quoted instead of gain for all results.

A series of gain profiles, created with different intensity inversion pulses are integrated over in Figure 5.3, and the resulting optical depth values are shown. The series is compared for the (a) matched and (b) mismatched beam conditions described in §5.1. The comparison shows that the gain profile is independent of the beam matching condition. Most notably, for both conditions the profile remained centered at 12.55 MHz $\pm$ 20 kHz and the measurement saturated when the optical depth exceeded 2.5. However, a +20 kHz shift is observed is observed in the center of the profile, with increasing optical depth, for only the mismatched case.

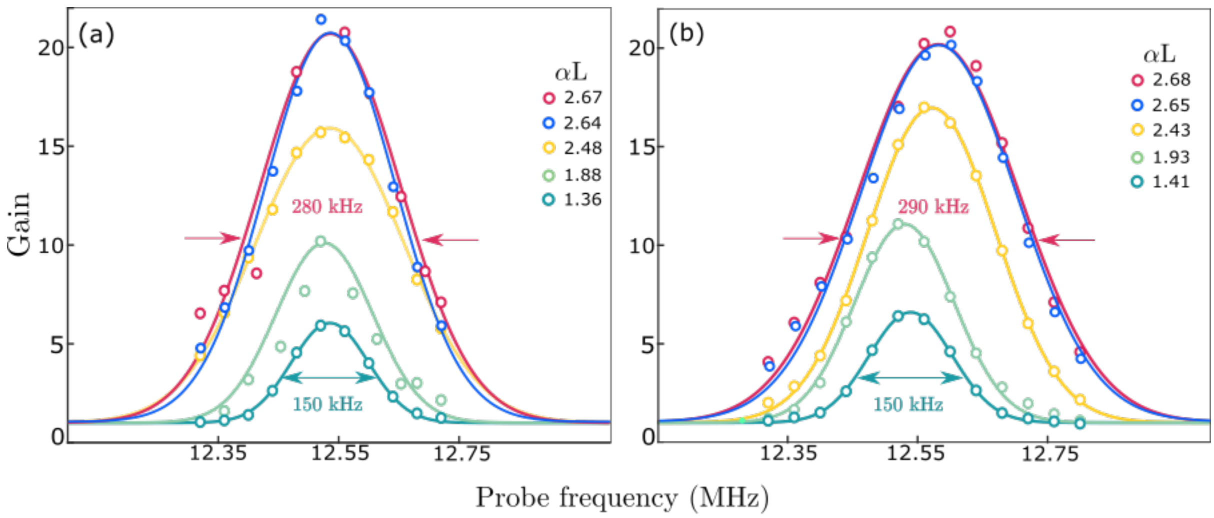

Figure 5.3: A series of gain profiles are integrated over to give the *average* optical depth values αL, each with $\pm$ 2% uncertainty, of the ASE transition for the ensemble. The series is shown using the (a) matched and (b) mismatched beam conditions described in §5.1.

The relationship between inversion pulse intensity and optical depth is shown in Figure 5.4. The measurement is sensitive to changes in the intensity of the inversion pulse, i.e the dependency is linear, until the optical depth exceeds 2.5. Therefore, the optical depth measurement can be performed in two distinct regimes: linear and saturated.

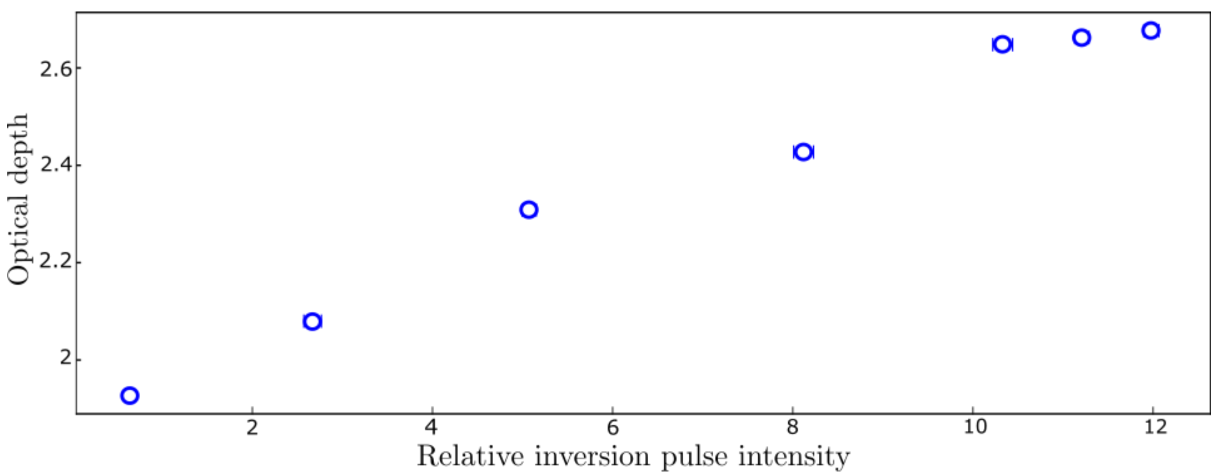

Figure 5.4: The relationship between the *average* optical depth of the ensemble αL and the relative intensity of the inversion pulse. The intensity of the inversion pulse was calculated from the Fourier transform of the pulse after the pulse was electronically filtered. The intensity values are, therefore, much smaller than the applied pulse. The intensity of the inversion pulse is not shown below an optical depth of 1.9, because at this point the beat was below the background noise.

5.2.2 Characterizing ASE

The ASE signal was measured using the complete RASE pulse sequence (see §6.1.3). For simplicity, only the portion of the RASE sequence relevant to the ASE measurement is shown in Figure 5.5.

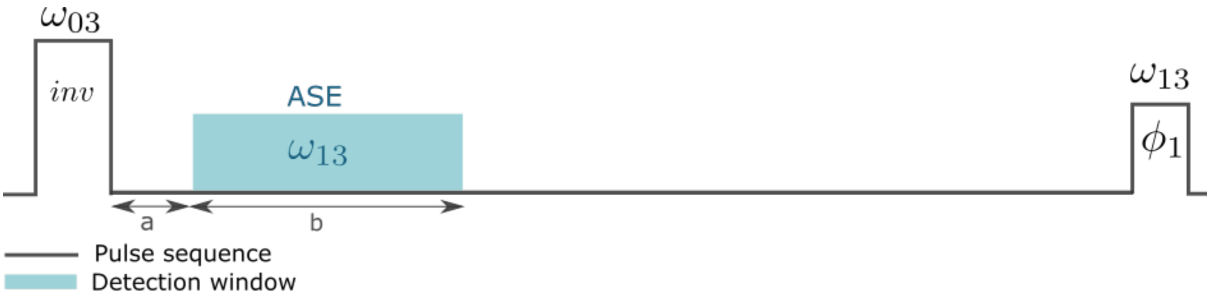

Figure 5.5: The portion of the temporal RASE pulse sequence (see Figure 6.5) relevant to the ASE measurement. The ensemble was initialized in the ground state $|0\rangle$ using the preparation sequence outlined in §4.3. A vacuum window of 100 μs was assigned before the sequence (not shown). The amplitude profile of the inversion pulse inv was shaped by convolving a top-hat and Gaussian function. The inversion pulse was centered at ω_{03} (see Figure 3.6) and chirped with a 300 kHz bandwidth for 8 μs duration. A delay time of a=3.5 μs was included before the ASE detection window of duration b=10 μs. The phase reference pulse ϕ_1 was at ω_{13} for 3 μs duration, with a pulse area of roughly $\frac{\pi}{10}$.

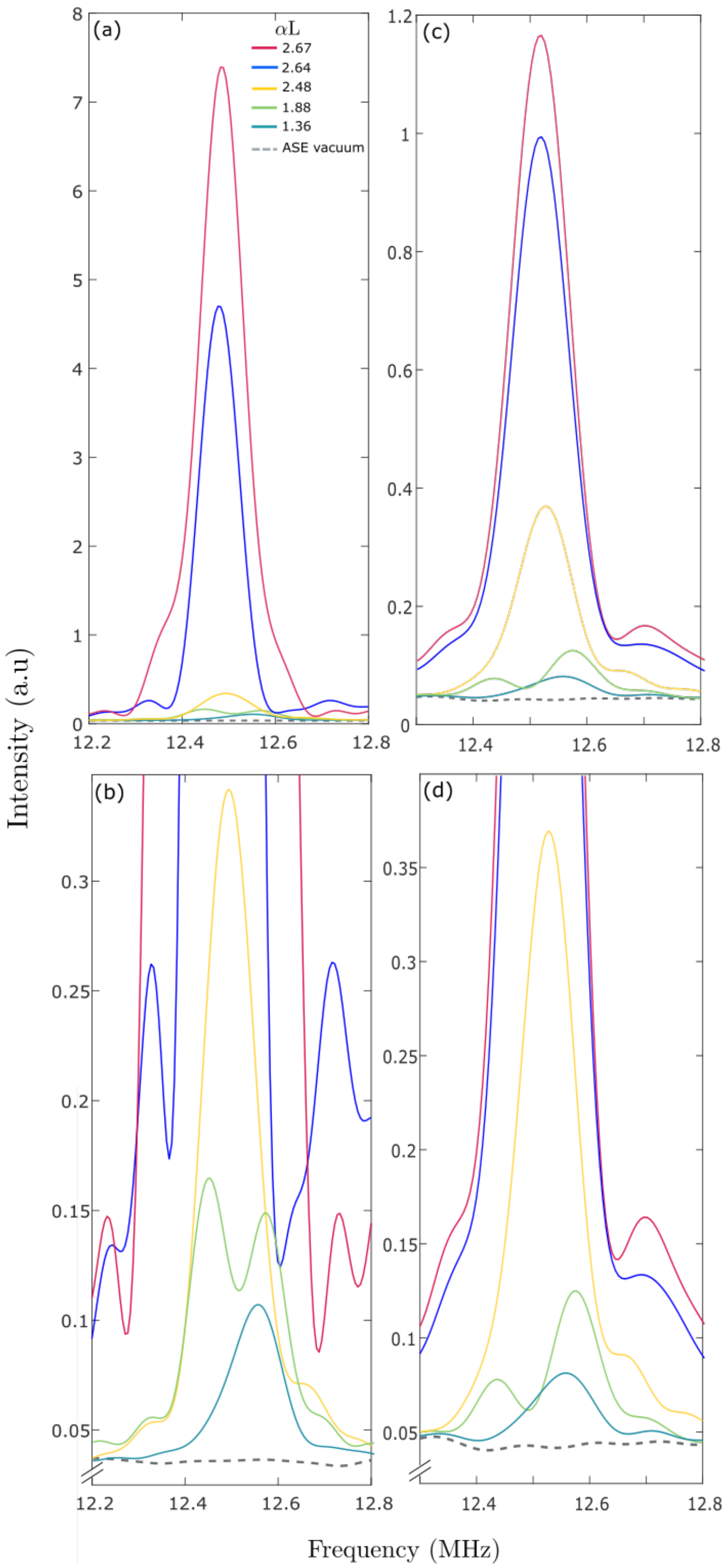

Figure 5.6: The frequency spectrum in the ASE detection window which is an average of 1,000 repetitions of the experiment (note the different y-axes). The ASE spectrum in the vacuum window is shown as a reference. The vacuum level was different for the matched and mismatched conditions because the measurements were taken on different days. A series of spectra are shown for the (a,b) matched and (c,d) mismatched beam conditions outlined in §5.1. The quoted optical depth values correspond to the gain measurements shown in Figure 5.3, and have an uncertainty of ± 2% from the fitting of the gain profile.

The frequency spectrum of the ASE detection window is shown in Figure 5.6, where an ASE signal is observed close to the expected beat frequency of 12.6 MHz. The amplitude profile of the feature is shown for a series of optical depths. The spectra the average of 1,000 repetitions of the experiment where, for this level of averaging, the lowest optical depth the ASE peak could be resolved was 1.4. The series is compared for the matched beam condition, in (a,b), and the mismatched beam condition, in (c,d) (see §5.1). The comparison shows that when the gain measurement was in the linear response regime, i.e. the optical depth was less than 2.5, the intensity profile was independent of the beam matching. In this regime the feature remains centered at roughly 12.5 MHz, and some distortion occurs when optical depth is 1.88.

However, when the gain measurement was in the saturated response regime, i.e. the optical depth was greater than 2.5, the intensity profile of the ASE feature was dependent on the beam matching. In this case the peak intensity of the ASE feature was much greater for the matched beam condition.

Next, the quadrature values are calculated to confirm that this signal, which is observed at the expected beat frequency of ASE, is the result of spontaneous emission.

5.3 Characterizing ASE Quadrature Values

The ASE signal was integrated over the detection window to give an *average* value for the quadratures. The values are not expected to average to zero on time scales which are comparable to the inverse of the gain profile full width half maximum (FWHM) (this assumption is evaluated in §7). Therefore, the duration of detection window is matched to this value. In §5.2.1 the gain profile bandwidth was shown to increase with optical depth, and therefore the duration of the shaped ASE window will decrease with optical depth.

An apodizing function was used to shape the ASE window (see §6.2 for details). The shaped ASE window was then spectrally filtered with a 500 kHz bandwidth Gaussian function, centered at 12.55 MHz. After filtering, the ASE window was numerically homodyned at 12.55 MHz, and a phase correction was applied (see §4.4.3).

For a spontaneous emission event, both the amplitude $\hat{x}$, and phase $\hat{p}$ quadratures, should average to zero over many repetitions of the experiment. This is in contrast with a coherent event, which will have a well defined phase. To confirm the signal observed at the $\sim$12.6 MHz (see §5.2.2) is the result of amplified spontaneous emission, the average of the quadrature values in the ASE detection window, $\hat{x}_1$ and $\hat{p}_1$, are calculated. This measurement was taken at an optical depth of 0.8, and was the average of 15,000 repetitions of the experiment. Both quadratures are shown to average to zero in Figure 5.7 (a), indicating that the observed signal is the result of amplified spontaneous emission.

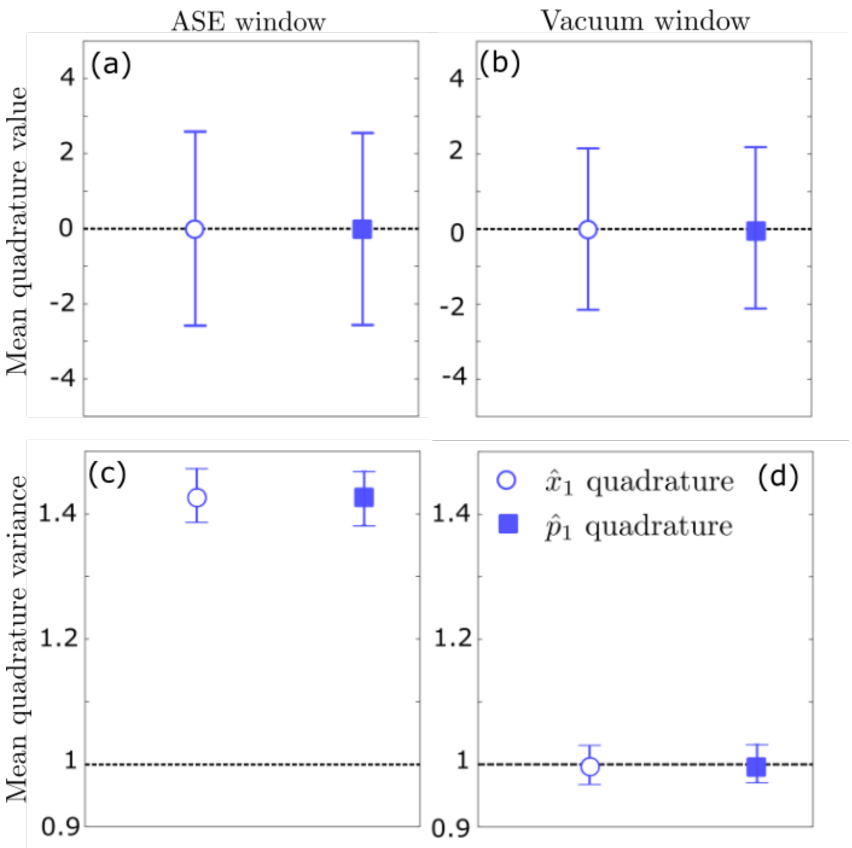

Figure 5.7: Statistics of the RASE amplitude $\hat{x}_1$, and phase $\hat{p}_1$, quadrature values. This measurement was performed at an optical depth of 0.8, and was the average of 15,000 repetitions of the experiment. The mean of the quadrature values, when digitally homodyned at the observed ASE beat frequency, which was 12.55 MHz, are shown in (a) the ASE window, and (b) the vacuum window (see §6.2 for details). In both windows, the variance in the quadrature values was normalized to the quadrature variance in the vacuum window, and are shown for (c) the ASE window and (d) the vacuum window.

For comparison, the quadrature values are calculated in the vacuum window (see §6.2 for details). The average amplitude and phase quadrature values, after being digitally homodyned at the expected ASE beat frequency, are shown in Figure 5.7 (b). Similar to the ASE window, the two quadratures average to zero.

In both windows, the variance in the quadrature values was normalized to the variance in the vacuum window. In Figure 5.7 (d) the quadrature variance in the vacuum window is confirmed to be one. While, in Figure 5.7 (c), the quadrature variance in the ASE window is confirmed to be larger than the vacuum level. With the quadrature variance in the ASE window larger than in the vacuum, the next step is to assess the gain dependency.

5.4 The Gain Dependency of the ASE Quadrature Variance

The amplitude and phase quadrature variances have the same gain dependency (see Eq. (3.10)). Therefore, in this section, the experimental gain dependency is assessed using an average of the variances $\langle \hat{X}_1^2 \rangle$ (see Eq. (3.11)).

To confirm whether a spatial mode mismatch inside the crystal affects this dependency, the result is compared for the matched and mistmatched beam conditions outlined in §5.1. The two results are also compared to the theoretical dependency (see Eq. (3.11)), which incorporates the 89% signal loss expected in the experiment (see §4.5).

The gain dependency of the ASE quadrature variance, using the matched and mismatched beam conditions, are shown in Figure 5.8. In Figure 5.8 (a) the variance is shown to follow the theoretical model reasonably well for both configurations until the optical depth approaches 2.5. It should be noted, however, that the experimental result is slightly larger than the theory between an optical depth of 1 and 1.7 using the matched configuration. When the optical depth is increased beyond 2.5 the experimental result is larger than the theory for both beam conditions. In this regime, values for the variance were larger using the matched condition compared to unmatched, shown in Figure 5.8 (b).

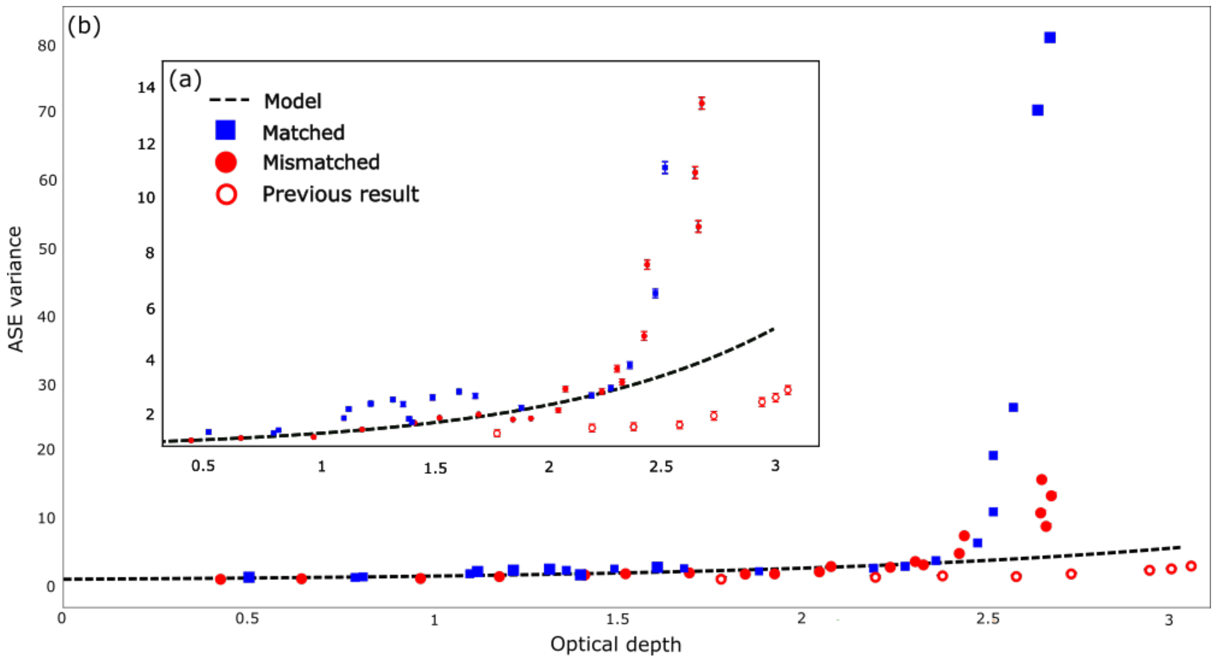

Figure 5.8: The optical depth dependency of the average ASE quadrature variance $\langle \hat{X}_1^2 \rangle$ (see §3.4.2). The dependency is compared for the matched and mismatched beam conditions, outlined in §5.1. For comparison, the previous result observed by Ferguson is included [73]. The theoretical curve is calculated using Eq. (3.11) with l=0.11 (see §4.5).

For both beam matching conditions the result is distinctly different from what Ferguson observed [73], which is included in Figure 5.8, and discussed in §3.5. Although the beam-area overlap used by Ferguson cannot be known precisely, it is unlikely it was less than the 35% used for the mismatched beam condition in this work. This would suggest that a spatial mode mismatch cannot explain why Ferguson's result doesn't agree with the model. However, given that the general trend seems similar, Ferguson's results could be explained if the optical depth measurement was incorrect.

A deviation from the theoretical model is expected as mode distortions become significant at large optical densities (see §3.4.2). The effect of mode distortions on the gain measurement is illustrated in Figure 5.9 (a). In this measurement the ASE event is stimulated by the input beam, and is emitted into a single output mode. At low gain, this couples efficiently into the collection fiber mode, and therefore measurement of optical depth scaled linearly with the intensity of the inversion pulse. At high gain, the output mode is distorted from the collection mode, and only a portion is collected. The effect is that the measurement saturates when the optical depth exceeds 2.5.

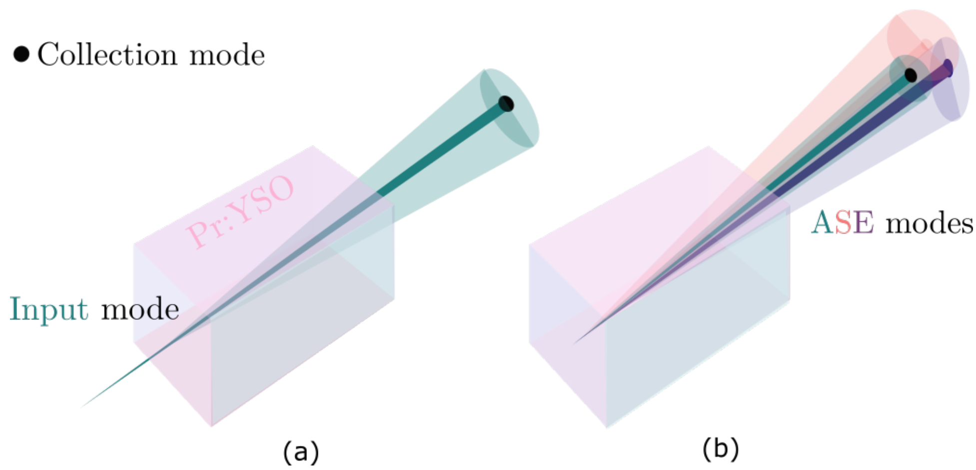

Figure 5.9: Illustration of the mode amplification and collection in the direct gain and ASE measurements. For the (a) gain measurement the input mode is defined by the probe beam. At low gain, the input is amplified and coupled into the collection fiber. At high gain, the amplified mode is distorted and only a portion is collected, therefore, the observed signal will saturate. For the (b) ASE measurement an infinite number of input modes exist, which are defined by the vacuum modes which couple to the crystal. At low gain, an ASE mode will exist that matches the collection mode. At high gain, additional ASE modes will be distorted into the collection mode, therefore, the observed signal will increase despite the distortions.

This is dissimilar to the ASE measurement, which is illustrated in Figure 5.9 (b). Because the experiment is performed in free-space, ASE will be emitted into a collection of modes, which are defined by the vacuum modes which couple to the crystal. At low gain, a single

ASE mode is matched with the collection mode. When the gain increases, other modes are distorted into the collection fiber, this results in the observed ASE signal increasing despite the distortion. This increase was observed in both the intensity of the spectral ASE signal (see §5.2.2) and the signal variance.

5.5 Summary

In this chapter the gain dependency of amplified spontaneous emission (ASE) was characterized for two different beam matching conditions. A mismatched configuration with 35% beam area overlap, and a matched configuration with 100% beam area overlap at the crystal. The gain dependency of the average ASE quadrature variance was shown to be independent of the beam matching condition, and consistent with the theoretical model, until an optical depth of 2.5. When the optical depth exceeded this value, the result deviated from the model, which is consistent with mode distortions being a source of gain dependent signal loss (see §3.4.2).

Chapter 6

Efficiency of Rephased Amplified Spontaneous Emission

To be a viable technology, a repeater must demonstrate efficiencies which exceed 90% (see §1.6). To achieve this efficiency level, the rephased amplified spontaneous emission protocol must operate at optical depths exceeding 2.5 (see §3.4.2).

In Chapter 5 the gain dependency of amplified spontaneous emission was measured. The ASE quadrature variance $\langle \hat{X}_1^2 \rangle$ was verified to follow the theoretical model until an optical depth of 2.5. Beyond this, however, the variance increased rapidly, which is consistent with the control pulses becoming spatially distorted (see §5.4).

These distortions are expected to have a larger effect on the rephased signal, when compared to ASE, because the rephased signal is dependent on a larger number of control pulses. Therefore, the efficiency performance of RASE is expected to deteriorate, instead of improve, with optical depth. The goal of this chapter was to pinpoint exactly when this effect is observed in the efficiency performance of RASE.

A powerful tool to characterize the efficiency performance of RASE, using the signal spectrum, is the four level echo (see §2.4.4). This is because the intensity of the optical echo is spectrally much larger than the small quantum signals of the RASE experiment. The standard four level echo, however, is an amplification of the input pulse (see §2.4.3), and therefore, will be inconsistent with the efficiency performance of RASE. This is verified over a range of optical depths in §6.1.2. For the four level echo to be consistent with the efficiency performance of RASE the ensemble must be inverted before the pulse sequence. In §6.1.4 the *inverted* four level echo is shown to be consistent with the efficiency performance of RASE. In the first instance, the signal spectrum is used as a straightforward way to ballpark the efficiency performance of RASE in §6.1.3. Using the signal variances, however, the efficiency can be calculated at small optical depths, where signals are below the background spectral noise.

The method used to calculate the variance in the signals is detailed in §6.2. Finally, a comparison between the two efficiency calculation methods, using the spectrum and variances, will indicate whether the RASE is performing at the quantum level. In §6.3 the two results are shown to be consistent, which suggests that very little classical noise is scattered into the RASE mode in the rephasing process (see §3.4 for details).

6.1 Investigating the Spectral RASE Efficiency with Optical Depth

A powerful diagnostic tool, which can be used to enhance our understanding of RASE, is the four level echo. This is because the large optical echo makes the spectral efficiency much easier to characterize. For example, averaging over 300 repetitions of the echo experiment, the signal was resolved in the spectrum until an optical depth of 0.3. In comparison, averaging over 1,000 repetitions of the RASE experiment, the RASE signal was resolved until an optical depth of 1.4

There are several key differences between the four level echo pulse sequence, and RASE pulse sequence. Firstly, the ensemble was prepared in the ground state $|1\rangle$ before the echo sequence (see §4.3). Secondly, a $\frac{\pi}{2}$ pulse was then used to initialize a coherence between the $|1\rangle$ and $|3\rangle$ states. In contrast, the ensemble was prepared in ground state $|0\rangle$ before the RASE sequence. Detection of amplified spontaneous emission, following an inverting pulse, initialized coherence between the $|1\rangle$ and $|3\rangle$ states in RASE.

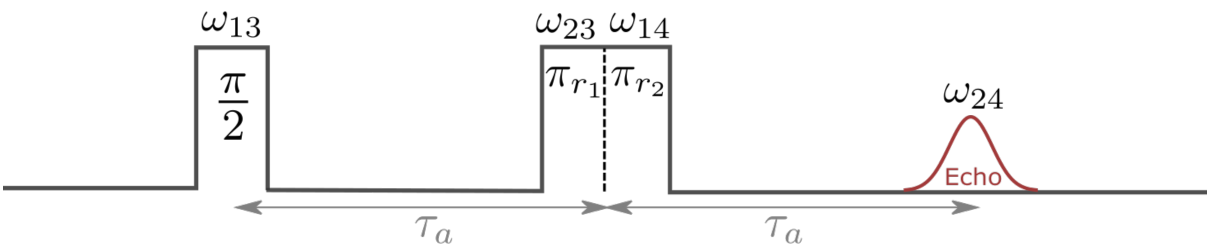

Figure 6.1: The pulse sequence used for the four level echo measurements, where the frequencies correspond to the optical transitions between the ground and excited hyperfine levels (see Figure 3.6). For these measurements the total delay time T was equal to $2\tau_a$.

The four level echo pulse sequence is shown in Figure 6.1, where the pulse frequencies correspond to the energy level structure given in Figure 3.6. The delay time between the $\frac{\pi}{2}$ pulse and the first rephasing pulse π_{r1} was τ_a. The optical echo was observed a time τ_a after the second rephasing pulse π_{r2}. Therefore, the total delay time T of the four level echo experiment was $2\tau_a$. The magnetic field in the lab changed daily and, therefore, the duration of the rephasing pulses, π_{r1} and π_{r2}, had to be optimized daily. Typically, π_{r1} had a duration of 1.7 μs and π_{r2} had a duration of 2.4 μs.

To compare the four level echo efficiency results with RASE, which used a different delay time, the efficiency results were extrapolated back to zero-delay time. This was done with a scaling factor calculated from the measurement of the four level optical decay time.

6.1.1 Measuring the Optical Decay time of the Four-level Echo

The optical decay time of the four level echo T^{4LE} was measured using the pulse sequence shown in Figure 6.1. To calculate the optical decay time, the echo intensity I was measured with increasing delay time T between the input $\frac{\pi}{2}$ pulse and echo. When the delay time was less than 80 μs the echo decay was exponential, shown in Figure 6.2. The exponential relationship between echo intensity and delay time is given by

$$I(T) = e^{-2T/T^{4LE}}. \tag{6.1}$$

Using this relationship in the exponential region, the four level optical decay time was calculated as 59.2 ± 1.4 μs.

In Figure 6.2 the decay of the optical echo is shown to be non-exponential when the delay time is greater than 80 μs. This is because the effects of any inhomogeneity which are not common to the two rephasing pulses are not rephased in the four level echo (see §2.4.4). Therefore, additional decoherence is introduced when these effects are given long enough to accumulate.

Therefore, the experimental delay times for the proceeding experiments are chosen to be within the exponential regime of the optical decay curve. The reasons for this are two-fold: firstly, so the efficiency results which used different delay times can be compared; secondly, to minimize the affects of any inhomogeneity which is uncommon to the two rephasing pulse transitions.

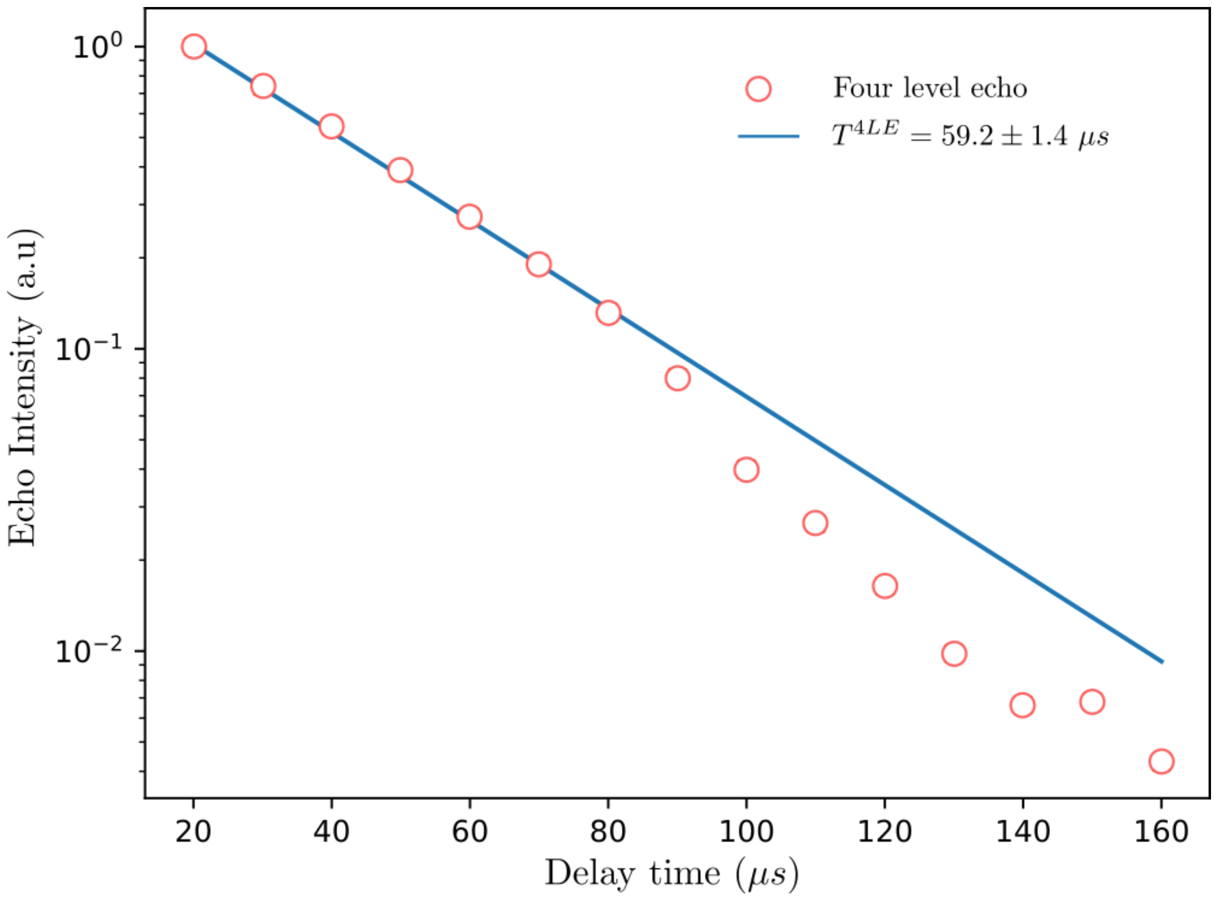

Figure 6.2: Measurement of the optical decay time of the four level echo T^{4LE} performed on the center of the absorption line for 0.005% Pr:YSO. Note that error bars are smaller than the marker size. The decay time was calculated by fitting the region T <80 μs, where the decay in echo intensity I with delay time T is purely exponential.

6.1.2 Characterizing the Efficiency of the Four-level Echo

In §2.4.3 the two level echo was adapted to perform in the gain regime relevant to quantum memory. This required replacing the strong $\frac{\pi}{2}$ pulse with a weak input pulse, such that the state was only slightly perturbed from the pole of the Bloch sphere. Therefore, to make a direct comparison to RASE, the efficiency performance of the four level echo is characterized using a weak input pulse.

To characterize the efficiency of the four level echo, the procedure developed by Beavan was used [52]. This involved creating an absorptive feature in the ground state $|1\rangle$ (see §4.3), which was spectrally much narrower than the input pulse.

The absorptive profile of the ensemble, with and without the ground state feature, is shown in Figure 6.3. The prepared feature was 200 kHz wide, and maximally absorbed the 2 MHz wide input pulse at a beat frequency of 12.6 MHz. Following the rephasing sequence, an echo was then observed at 7 MHz. In contrast, when no feature was prepared, the input pulse was completely transmitted and no echo was observed.

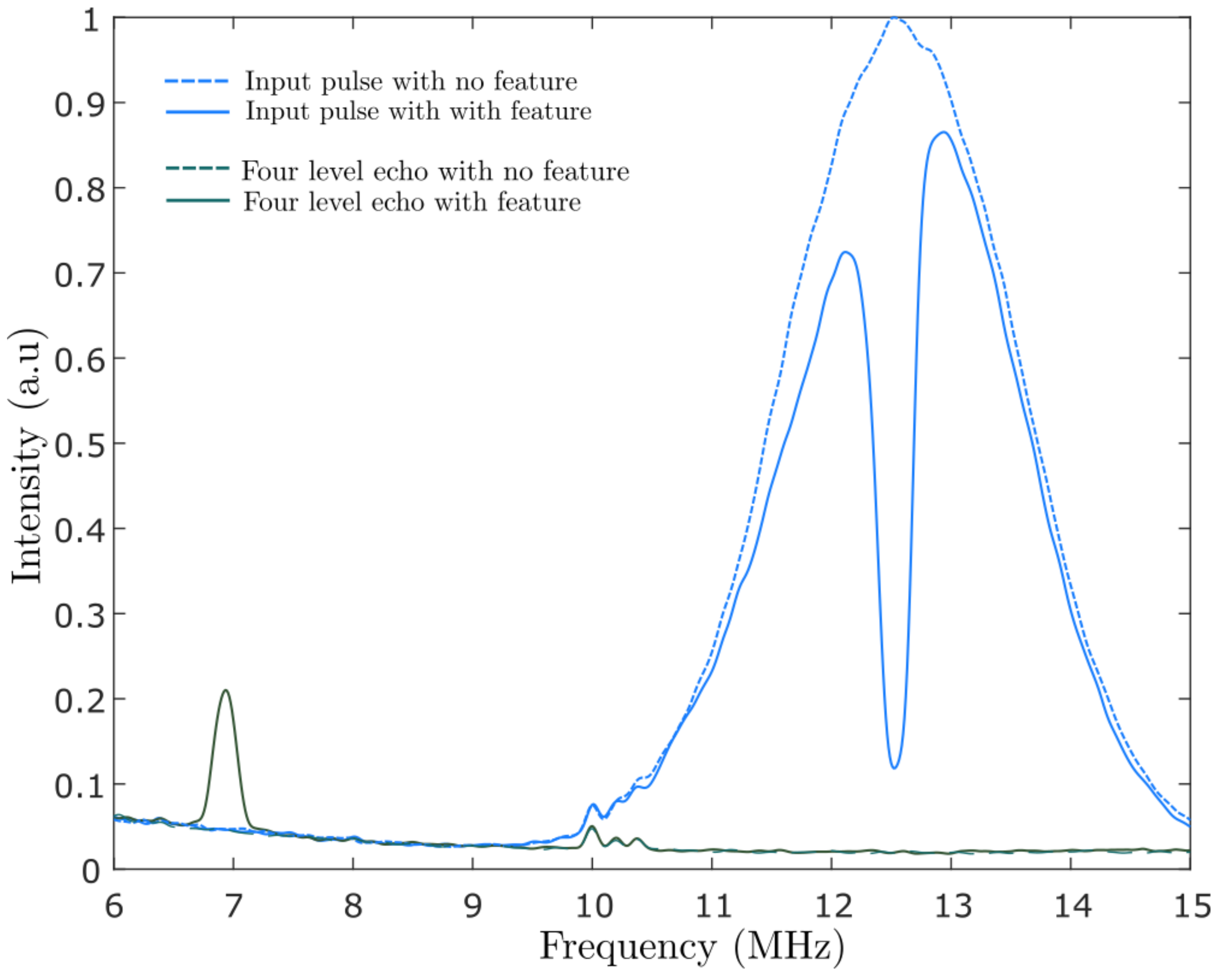

Figure 6.3: The absorptive profile of an ensemble, using the four level echo, with and without a feature prepared in the ground state $|1\rangle$. The profile was used to calculate the efficiency of the four level echo, where this measurement corresponds to an optical depth of 1.6 (see §5.2.1). The spectrum was the average of 300 repetitions of the experiment, and was normalized to when the input pulse was completely transmitted.

The steps taken to calculate the echo efficiency from the spectrum are described for the result in Figure 6.3, and summarized in Table 6.1. The echo intensity was calculated by subtracting off background (when no feature had been created) from the peak intensity of the echo in the spectrum. The frequency dependent gain of the detectors was accounted for using a scaling factor, which was calculated from the shot-noise limited background (see §4.4). Comparing the noise-floor at the echo frequency, 7 MHz, and input pulse frequency, 12.6 MHz, the detectors were 2.3 times more sensitive at the echo frequency. Therefore, the final value for the echo intensity was 0.07.

The spectrum in Figure 6.3 was normalized to when the input pulse was maximally transmitted. Therefore, an echo intensity of 0.07 corresponds to an efficiency result where 100% of the input pulse has been absorbed. For this measurement 88.2% of the input pulse was absorbed, therefore, the efficiency is a scaled up slightly to 8%.

The efficiency of the four level echo, using a delay time of 60 μs, is mapped for a series of optical depths in Figure 6.4 (a). The dependency is linear until an optical depth of 1.2, where the efficiency reaches 8 %.

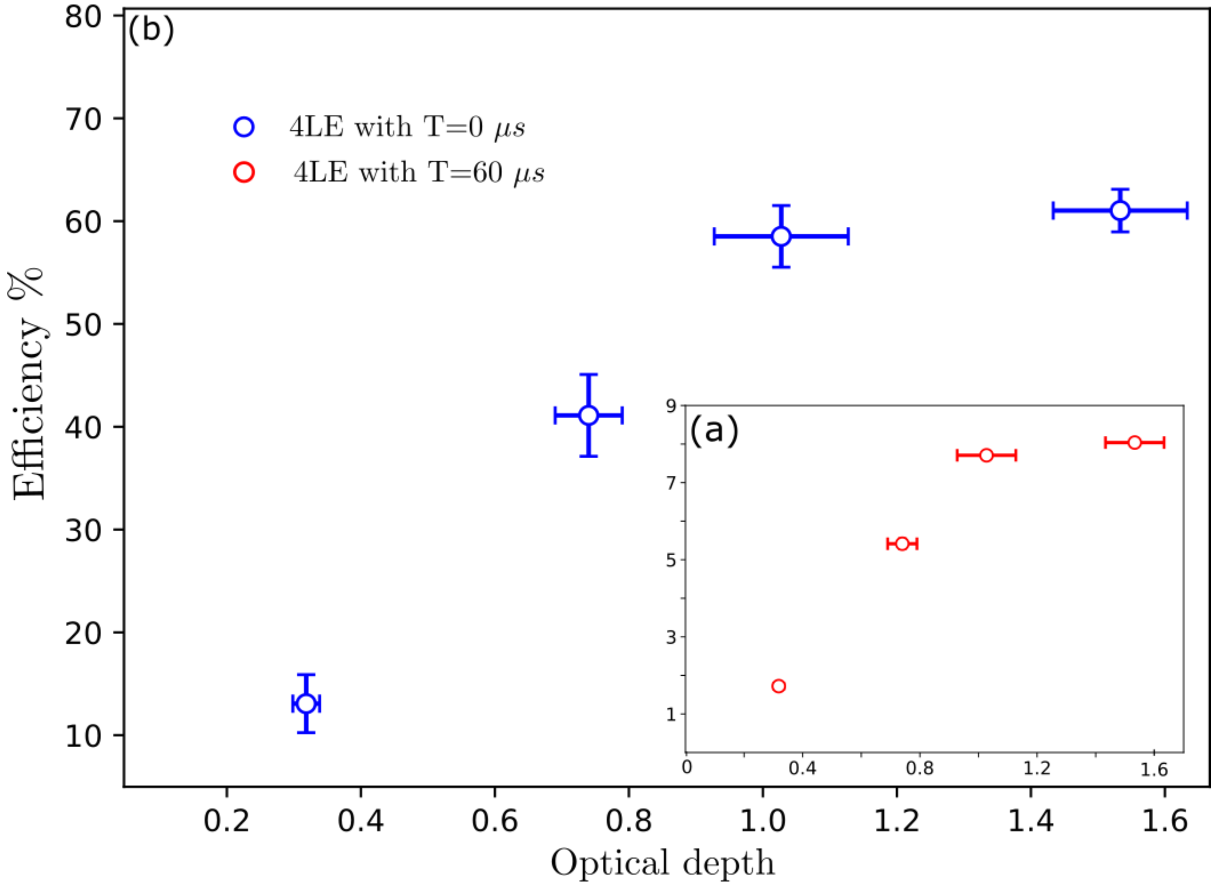

Figure 6.4: The efficiency of four level echo with optical depth (see §5.2.1), where T is the delay time between the input pulse and the echo, which was equal to $2\tau_a$. The results are shown for (a) the delay time used in the experiment, which was 60 μs (note that the vertical error bars are smaller than the marker size) and (b) scaled to zero-delay time.

To make a comparison to the RASE efficiency results in §6.1.3, which used a different delay time, the echo results are scaled. Because a delay time of 60 μs is in the exponential regime of the optical decay curve (see §6.1.1), the results can be extrapolated back to zero-delay time with a simple scaling factor

$$s = e^{-2\times T/T^{4LE}}, \tag{6.2}$$

where T is the delay time between the input pulse and the echo, and T^{4LE} is the four level echo optical decay time. The optical decay time was measured in §6.1.1 as 59.2 μs, and therefore the scaling factor was 0.13. An efficiency of 8% will, therefore, translate to an efficiency of 61% at zero-delay time.

Four level echo	
Input pulse absorption (± 2%)	88.2%
Echo intensity (± 2%)	0.07 a.u
Echo efficiency for 100% absorption (±2%)	7%
Echo efficiency for 88.2% absorption (±2%)	8%
Delay time	60 μs
Scale factor (± 2%)	0.13
Scaled echo efficiency (± 3%)	61.5%

Table 6.1: Summary of the key steps taken to calculate the four level echo efficiency, extrapolated back to zero-delay time. Values are taken from the absorptive spectrum shown in Figure 6.3 which was measured at an optical depth of 1.6.

The four level echo efficiency, which are scaled back to zero-delay time, are shown in Figure 6.4 (b). The efficiency increases linearly until an optical depth of 1, and then saturates at 60%. This is a similar result to what Ferguson observed, which was an efficiency performance of 60% at an optical depth of 1.6 [73].

6.1.3 Calculating the Spectral Efficiency of RASE

In the first instance, the spectral RASE efficiency can be used to make a direct comparison to the efficiency of the four level echo. The full RASE pulse sequence is shown in Figure 6.5, where the ensemble has been initialized in the ground state $|0\rangle$ prior to the sequence (see §4.3). In addition, a large vacuum window of 100 μs duration is assigned before the pulse sequence. A delay was included before the ASE and RASE detection windows, following the strong control pulses, to give the detector electronics time to recover from saturation. The delay time a after the inversion pulse was 3.5 μs, and delay time c after the second rephasing pulse was 5 μs. The delay time c was larger than a because the rephasing pulses were much more intense than the inverting pulse.

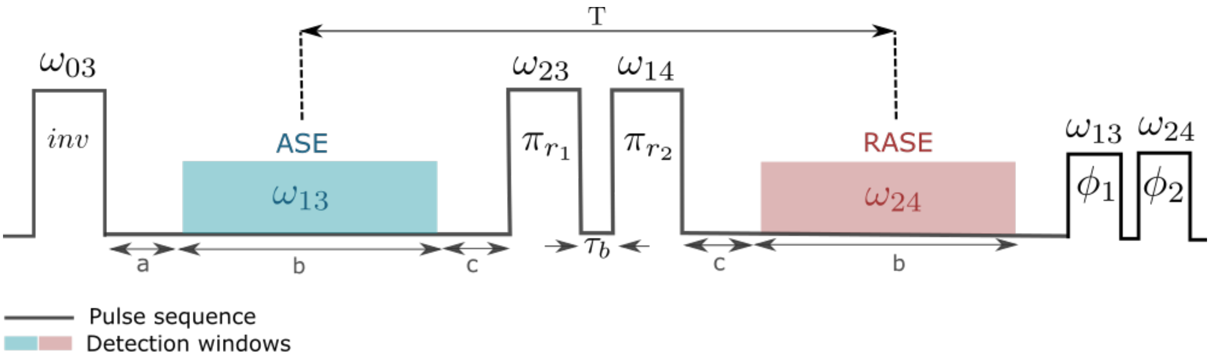

Figure 6.5: The temporal pulse sequence, delays and signal detection windows used for the RASE experiment. A large 100 μs vacuum window was assigned before the sequence begins (not shown). The delay times used in the experiment were a=3.5 μs, b=10 μs, c=5 μs, and $\tau_b = 5$ μs. The total delay time T was approximated as 25 μs. The amplitude profile of the inversion pulse *inv* was shaped with the convolution of a Gaussian and top-hat function. The rephasing pulses, π_{r_1} and π_{r_2}, had a Gaussian amplitude profile. The amplitude profile of the reference pulses, ϕ_1 and ϕ_2, were square.

The ASE and RASE signals were detected in over two windows of duration b, which was equal to 10 μs. The expected beat frequency of the ASE and RASE signals were f_A=12.6 and f_R=7 MHz respectively, which is defined by the hyperfine structure of Pr:YSO (see Figure 2.2). The ASE and RASE detection windows must be time symmetric around the center of the two rephasing pulses, therefore, a delay time of c was included after the ASE detection window. For all RASE measurements the delay between the first and second rephasing pulse τ_b was 5 μs.

The amplitude profile of the inversion pulse *inv* was shaped by convolving a top-hat and Gaussian function, and was chirped with a 300 kHz bandwidth for a 8μs duration. The amplitude profile of the rephasing pulses were Gaussian, and the durations, which were optimized day-to-day, were typically π_{r1}=1.7 μs and π_{r2}=2.5 μs. Two phase reference pulses, ϕ_1 and ϕ_2, were applied at the end of the sequence. These were at the ASE and RASE beat frequency, and necessary for the digital phase correction in post-processing (see §4.4.3). The amplitude profile of the reference pulses were square, with a 3 μs duration and a pulse area of roughly $\frac{\pi}{10}$.

To scale back to zero-delay time, and make a comparison with the four level echo efficiency result (see §6.1.2), the total delay time T of the RASE experiment must be approximated. This is an approximation because the ASE and RASE signals are detected over windows of duration b. In contrast, the four level echo has a well defined delay time of $2\tau_a$, between the input pulse and the optical echo. In this work, the RASE delay time was taken from the center of the two detection windows, and therefore, was equal to 25 μs. The center of the window was chosen because ASE signal will decay over the window [73], however, any emission at the end of the window is more likely to be rephased than at the start. The hyperfine delay time τ_b was also accounted for, because the hyperfine dephasing should be negligible compared to the optical decay.

The frequency spectrum of the three detection windows (vacuum, ASE and RASE) is shown in Figure 6.6. In the ASE window a large signal is visible at the expected frequency of 12.55 MHz, which is not present in the ASE vacuum window. In the RASE window a small signal is visible at the expected frequency of 6.95 MHz, which is not present in the RASE vacuum window. The ASE and RASE vacuum windows were created by digitally homodyning the vacuum window, where the signals were observed in the spectrum, in post-processing.

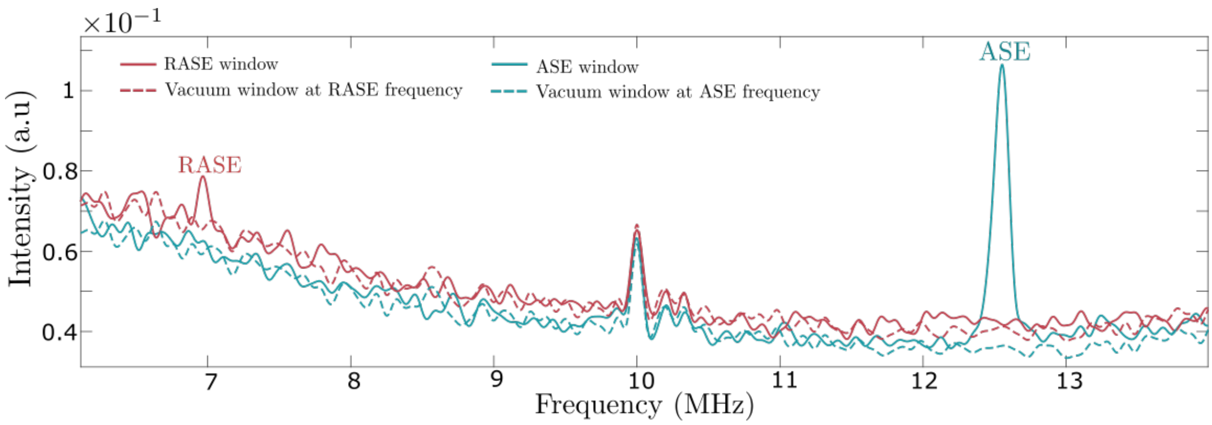

Figure 6.6: Spectrum of the vacuum, ASE, and RASE detection windows, corresponding to an optical depth of 1.4 (see §5.2.1). The vacuum window was digitally homodyned in post-processing where the ASE and RASE signals are observed in the spectrum, and therefore, two traces are shown. The time-trace was balanced in post-processing, and the spectrum is an average of 1,000 repetitions of the experiment.

The amplitude profile of the RASE spectral feature is characterized with optical gain in Figure 6.7 (a). The spectrum was an average of 1,000 repetitions of the experiment, where, for this level of averaging, the lowest optical depth the RASE peak could be resolved at was 1.4. At this optical depth a small Gaussian signal was observed at 6.96 MHz. When the gain was increased, the peak drifted to 6.9 MHz and became distorted.

To make a comparison with the gain dependency of the RASE spectral feature, the ASE spectral feature (characterized in §5.2.2) is shown in Figure 6.7 (b) and (c). In both cases a distortion occurs at an optical depth of ∼1.9. As the gain was increased further this distortion disappeared in the ASE signal. This was not the case for RASE signal, where the distortion reappeared once the gain measurement had saturated.

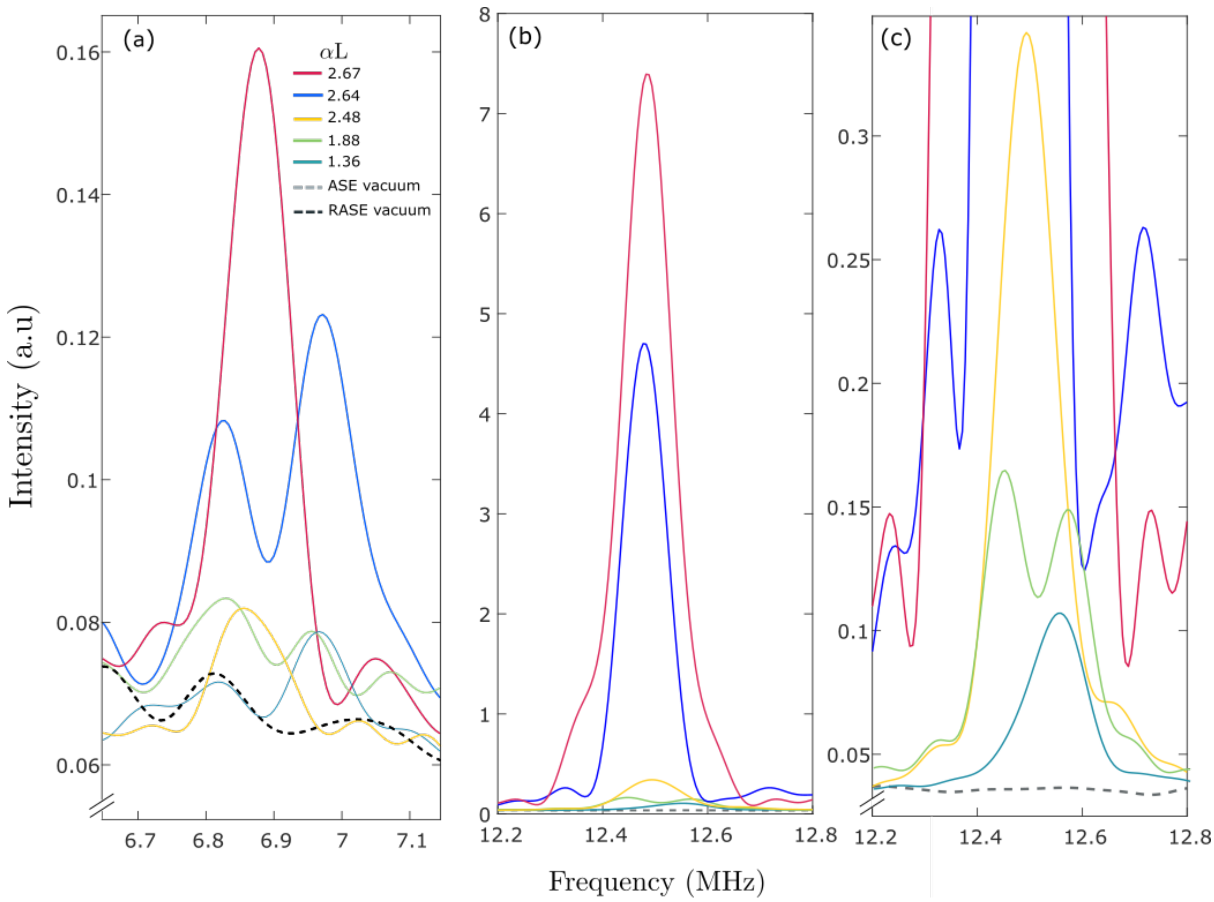

Figure 6.7: The intensity spectra for the (a) RASE signal and (b,c) ASE signal (see Figure 5.6) with optical depth. Both spectra are an average of 1,000 repetitions of the RASE experiment. The quoted optical depth values correspond to the gain measurements shown in Figure 5.3, and have an uncertainty of ± 2%.

The spectral efficiency was calculated from the ratio of the ASE and RASE spectral peak intensities. For both spectral peaks the intensity was calculated by subtracting off the background at the respective signal frequency. The frequency dependent gain was also taken into account, which was at the same level as the four level echo measurement (see §6.1.2).

The experimental RASE efficiency with optical depth is shown in Figure 6.8 (a). The efficiency is maximized at 7% at an optical depth of 1.4, and then steadily decays close to zero at an optical depth of 2.7. The RASE efficiency result is scaled to zero-delay time, and compared to the four level echo efficiency (see §6.1.2) in Figure 6.8 (b). Comparing the two results, the efficiency of the four level echo is consistently larger than RASE.

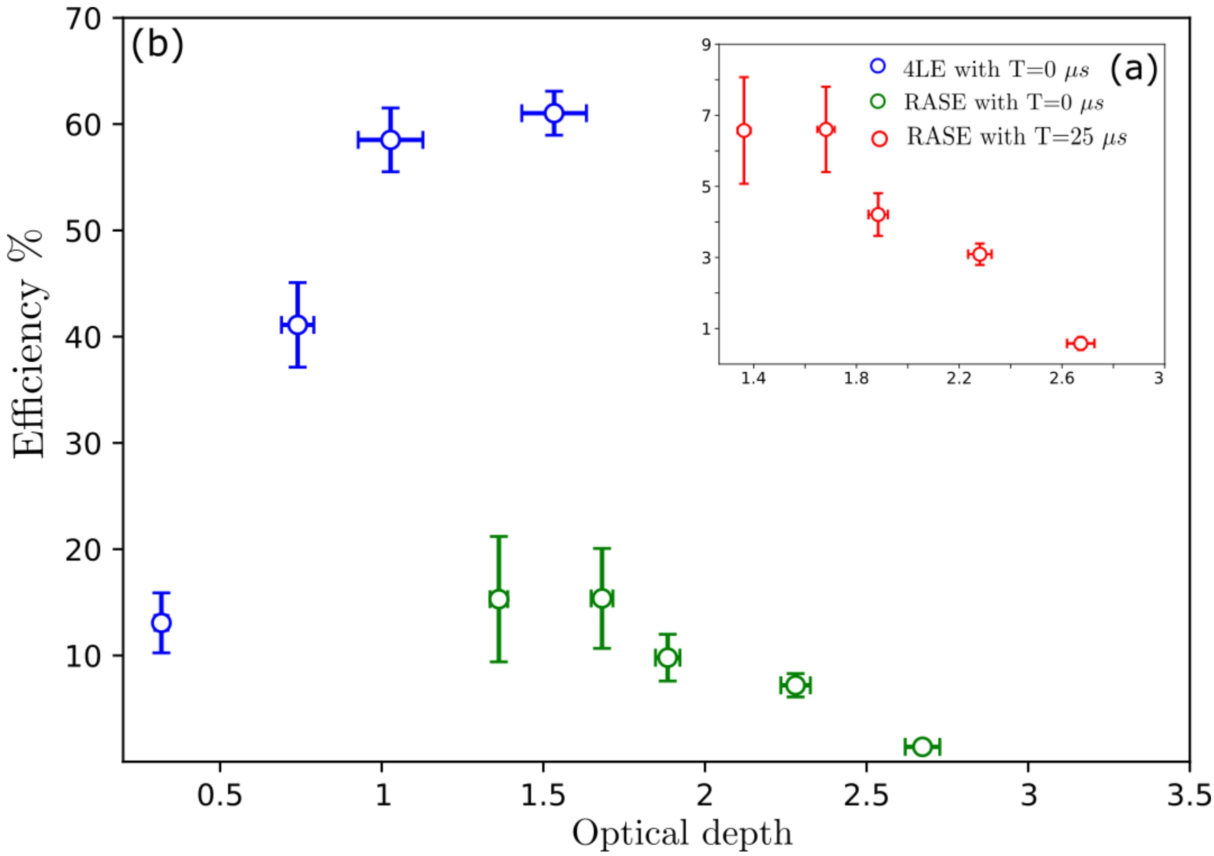

Figure 6.8: RASE efficiency with optical depth (see §5.2.1) calculated from the ratio spectral peaks, taking into account the frequency dependent gain of the detectors. The efficiency is shown for the (a) experimental result with delay time T=25 μs and (b) when scaled back to zero delay time. The scaled four level efficiency result (see §6.1.2) is also included.

To illustrate why the efficiency performance of the four level echo protocol is inconsistent with the RASE result, an energy level representation of the two protocols is compared in Figure 6.9. In the echo protocol, shown in (a), the input state is amplified by the gain on the echo transition. Therefore, the efficiency performance can exceed 100% [99, 100]. This is not possible with the RASE protocol, shown in (b), where the maximum efficiency possible is 100%.

The four level echo is, therefore, fundamentally different from the RASE protocol because the final echo can be larger than the input state. A closer analog to the RASE protocol is the inverted four level echo.

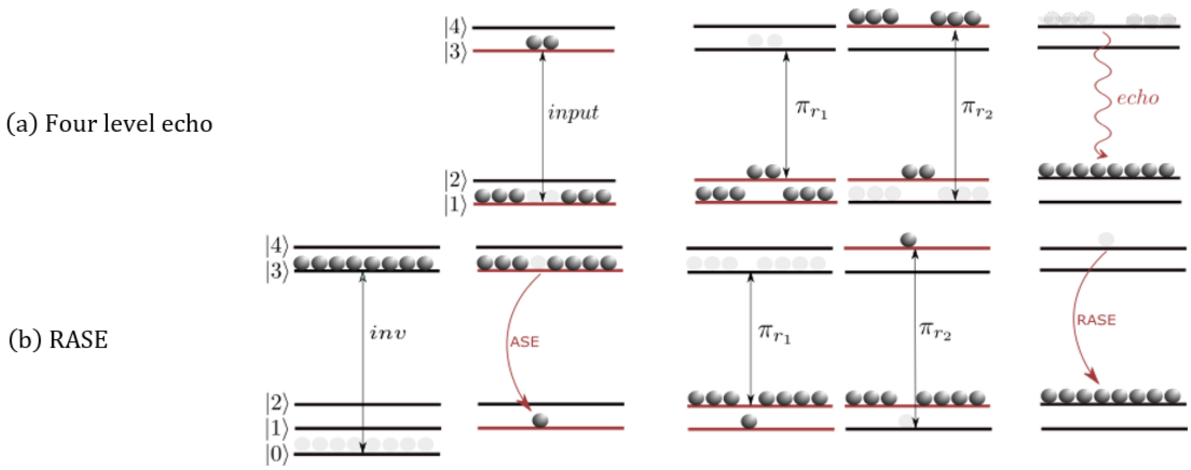

Figure 6.9: Energy level representation of the (a) four level echo protocol and (b) RASE protocol.

6.1.4 Characterizing the Efficiency of the Inverted Four-level Echo

A closer analog to the RASE protocol, when compared to the four level echo, is the inverted four level echo. To illustrate why, an energy level representation of the two pulse sequences are compared in Figure 6.10. The inverted four level echo is shown in (a), where the ensemble is initialized in a predominately excited state following an inverting pulse. The effect of this inversion is that the echo is created from a predominately ground state ensemble, and therefore, the efficiency cannot exceed 100%.

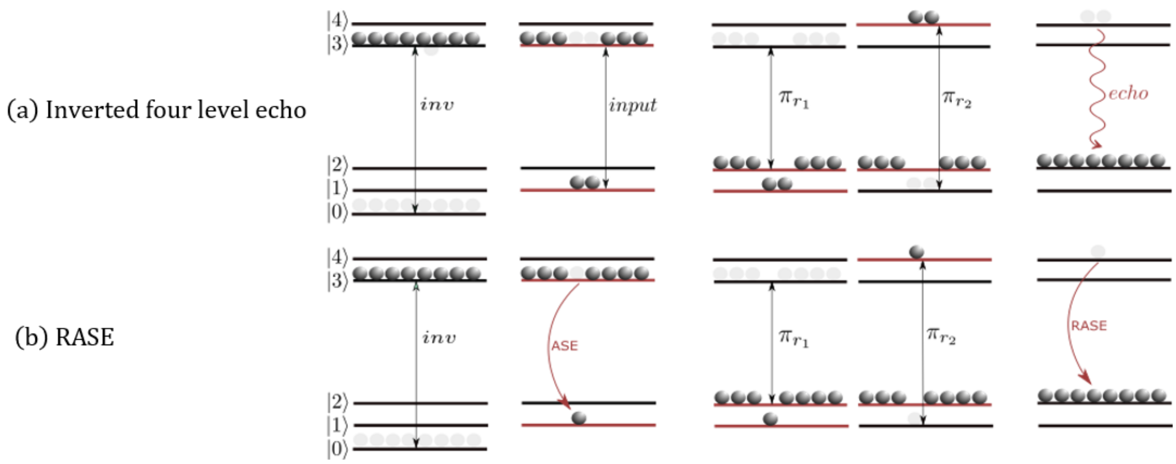

Figure 6.10: Energy level representation of the (a) inverted four level echo protocol and (b) RASE protocol.

The pulse sequence used for the inverted four level echo measurements is shown in Figure 6.11. Prior to the sequence, the ensemble was prepared in $|0\rangle$. An excited state was then prepared in $|3\rangle$, with an inversion pulse identical to in the RASE sequence. A weak input pulse was then applied on the $|1\rangle \rightarrow |3\rangle$ transition, which creates a predominately excited state ensemble. This is in contrast to the four level echo, where the ensemble was in a predominately ground state. The same sequence of rephasing pulses is then applied as in four level echo.

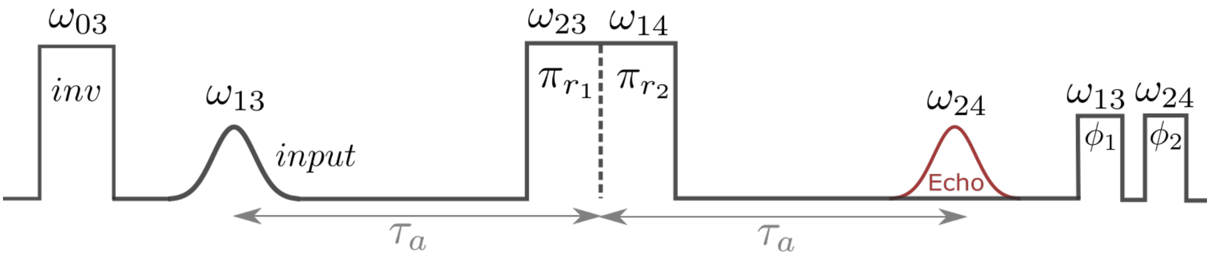

Figure 6.11: The pulse sequence used for inverted four level echo measurements, where the total delay time T is equal to $2\tau_a$, and the pulse frequencies correspond to the energy levels given in Figure 3.6.

The same phase correction method used for RASE was included in the inverted four level echo analysis (see §4.4). This was required two phase reference pulses, ϕ_1 and ϕ_2 (see §6.1.3 for details), to be included at the end of the pulse sequence. This was necessary because the intensity of the inverted four level echo was much smaller than the four level echo.

The emission profile of the ensemble, with and without the excited state feature, is shown in Figure 6.12. When the 200 kHz wide feature is prepared in the excited state, the 2 MHz wide input pulse was maximally amplified at 12.6 MHz. In this case, the input pulse was amplified by a factor of 8 on resonance. Following the rephasing sequence, an echo was then observed at 7 MHz. In contrast, when no feature was created in the excited state, the input pulse is completely transmitted and no echo is observed.

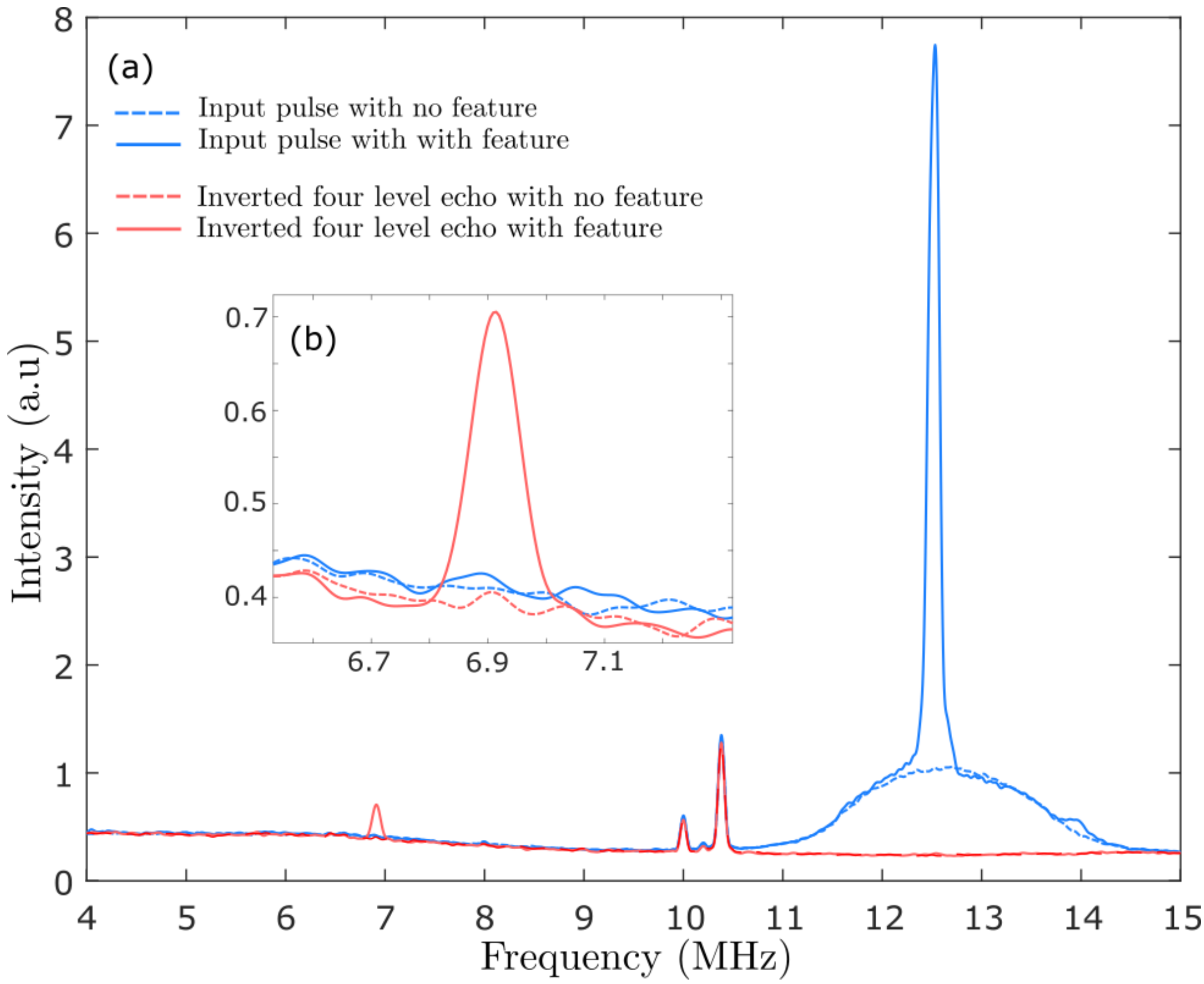

Figure 6.12: The emission profile of the ensemble, using the inverted four level echo, with and without a feature prepared in the excited state $|3\rangle$. The profile was used to calculate the efficiency of the inverted four level echo, where this measurement corresponds to an optical depth of 1.4 (see §5.2.1). The spectrum was an average of 3,000 repetitions of the experiment, and was normalized to when the input pulse was completely transmitted. The amplified input pulse is shown in (a), and the resultant echo is shown in (b).

The efficiency of the inverted four level echo was calculated using the spectrum. The background at the input and echo frequency was subtracted off to calculate the signal intensities. The frequency dependent gain of the detectors was also accounted for in the calculation (see §6.1.2) which, for this measurement, was 1.8 times more sensitive at the echo frequency.

The efficiency of the inverted four level echo, with experiment delay time of 60 μs, is shown in Figure 6.13 (a). The efficiency was maximum at an optical depth of 1, and decreased when the optical depth was increased further. The efficiency of the inverted echo was scaled to zero-delay time, and compared to the four level echo and RASE in (b). In this comparison, the efficiency of the inverted four level echo is shown to be consistent with RASE.

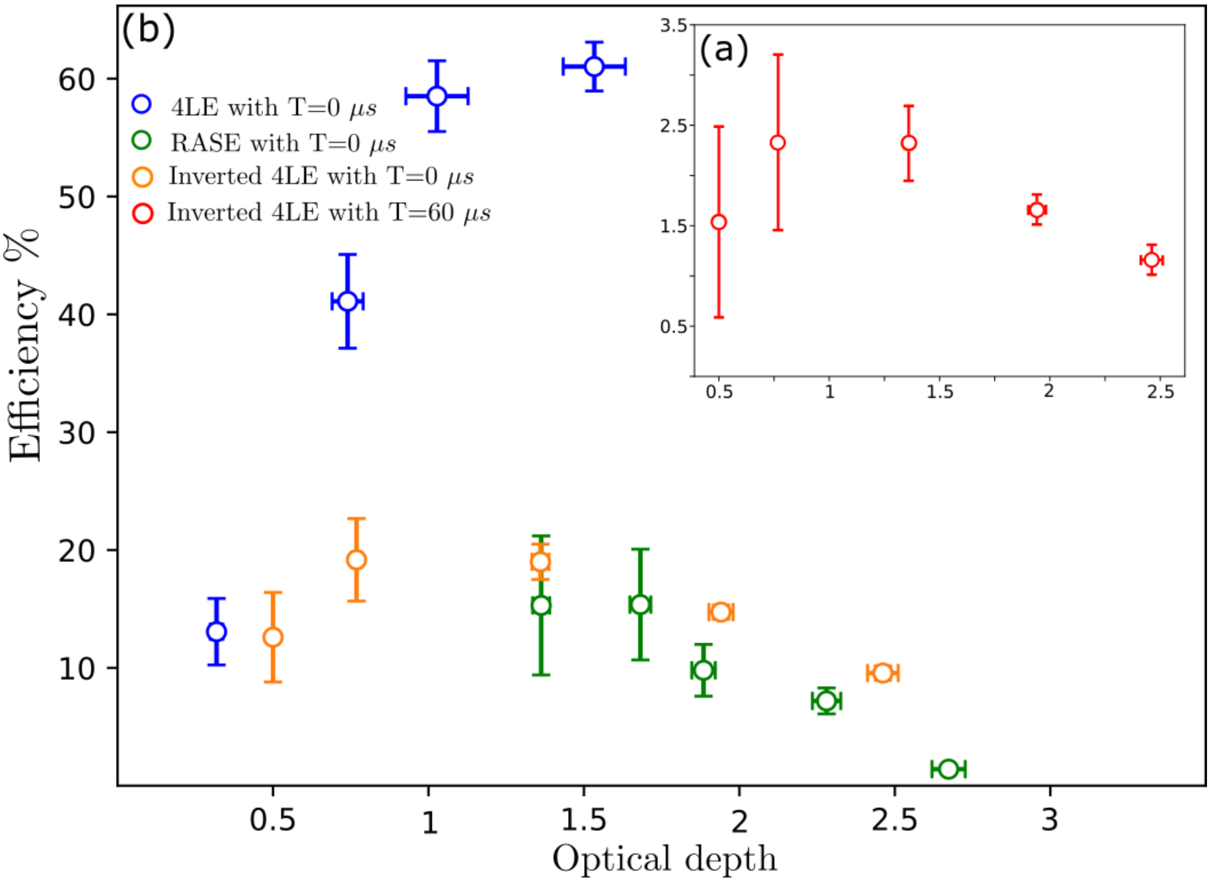

Figure 6.13: The inverted four level efficiency with optical depth (see §5.2.1) is shown in (a) for the experimental delay time of T=60 μs and (b) for the result scaled to zero-delay time. The scaled RASE efficiency result (see §6.1.2) and scaled weak input four level echo result (see §6.1.3) are also included.

6.2 Characterizing RASE Quadrature Variance

The quadrature values, for a single run of the experiment, were calculated by integrating over the signal detection windows. The values are not expected to average to zero on time scales which are comparable to the inverse of the gain profile full width half maximum (FWHM) (this assumption is evaluated in Chapter 7). Therefore, to calculate the quadrature values, the duration of the signal windows are shaped to match the inverse of the gain profile FWHM. Because the FWHM of the gain profile increased with optical depth (see §5.2.1), the duration of the shaped temporal windows decreased with optical depth.

The duration of the signal windows was adjusted with an apodizing function, which was the convolution of a top-hat function, of variable duration T_h, and a 500 kHz bandwidth Gaussian function. The shape of the signal detection windows, when the top-hat function was varied from 3 μs to 9 μs, is shown in Figure 6.14. The relationship between the choice of top-hat function, used to shape the window, and the measured optical depth is shown in

Figure 6.15.

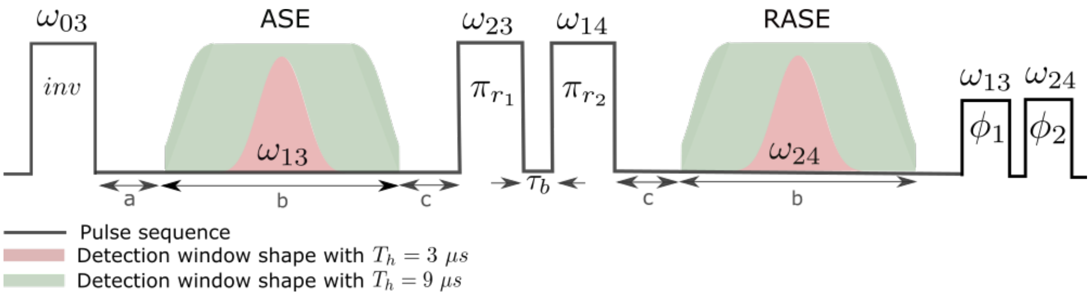

Figure 6.14: The temporal pulse sequence for the RASE experiment (identical to the pulse sequence in §6.5), where the ASE and RASE windows have been shaped to calculate the quadrature values. A large 100 μs vacuum window is also assigned before the sequence begins (not shown). To shape the detection windows of duration b, they were multiplied with an apodizing function. This function was created by convolving a top-hat function with a 500 kHz bandwidth Gaussian function. The duration of the shaped windows was varied by changing top-hat function duration T_h, which ranged from 3 μs to 9 μs.

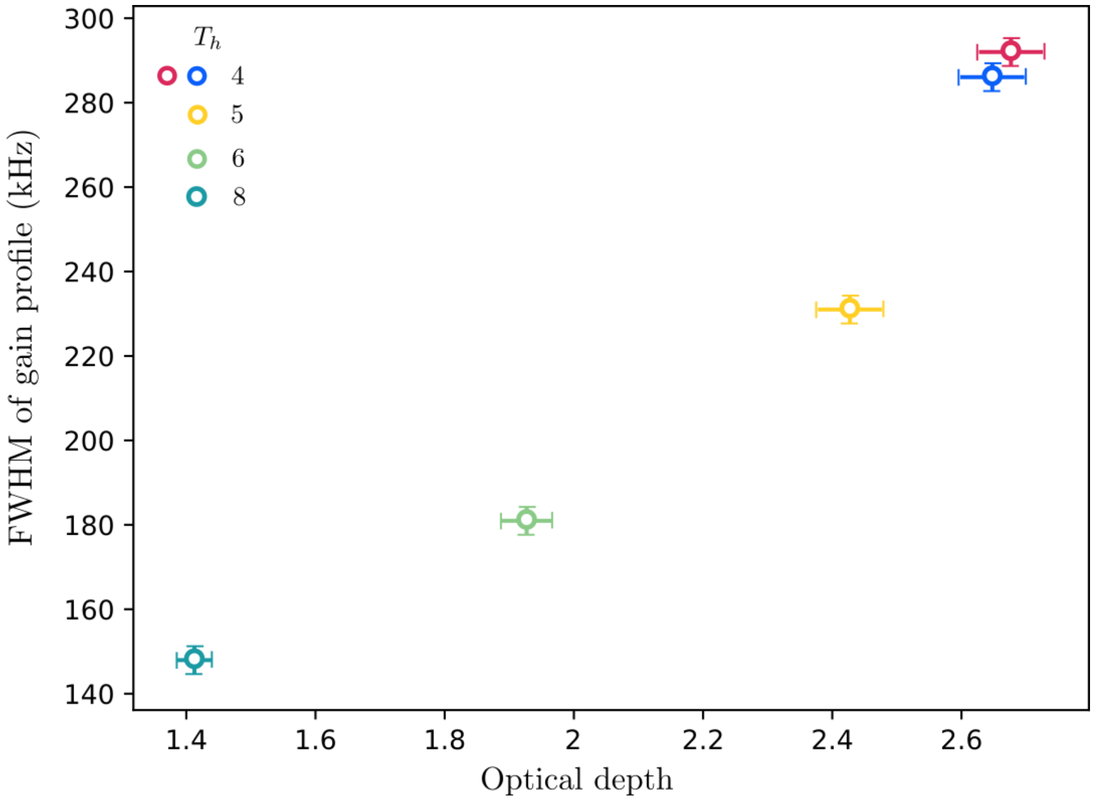

Figure 6.15: Relationship between the duration of the top-hat function T_h (μs), which is varied between 4 and 8 μs to shape the ASE window, and the measured optical depth of the ensemble. The quoted optical depth values correspond to the gain measurements shown in Figure 5.3.

After the temporal detection window was shaped, the windows were spectrally filtered. The spectral filter was a 500 kHz bandwidth Gaussian function, which, unless specified otherwise, was centered at f_A=12.55 and f_R=6.95 MHz for the ASE and RASE window respectively.

The signals were then digitally homodyned, where the signals were observed in the spectrum, and phase corrected (see §4.4.3) in post-processing. An *average* value for the both amplitude and phase quadrature was calculated by integrating over the shaped ASE and RASE windows.

To determine if the signal at the expected beat-frequency of the RASE is the result of spontaneous emission, the measured quadrature values are averaged over many repetitions of the experiment (see §5.3 for details). In the RASE window, the average amplitude and phase quadrature values, for 15,000 repetitions of the experiment, are shown to be zero in Figure 6.16 (a). This strongly suggests that the spectral feature observed at expected beat frequency of RASE is the result of spontaneous emission.

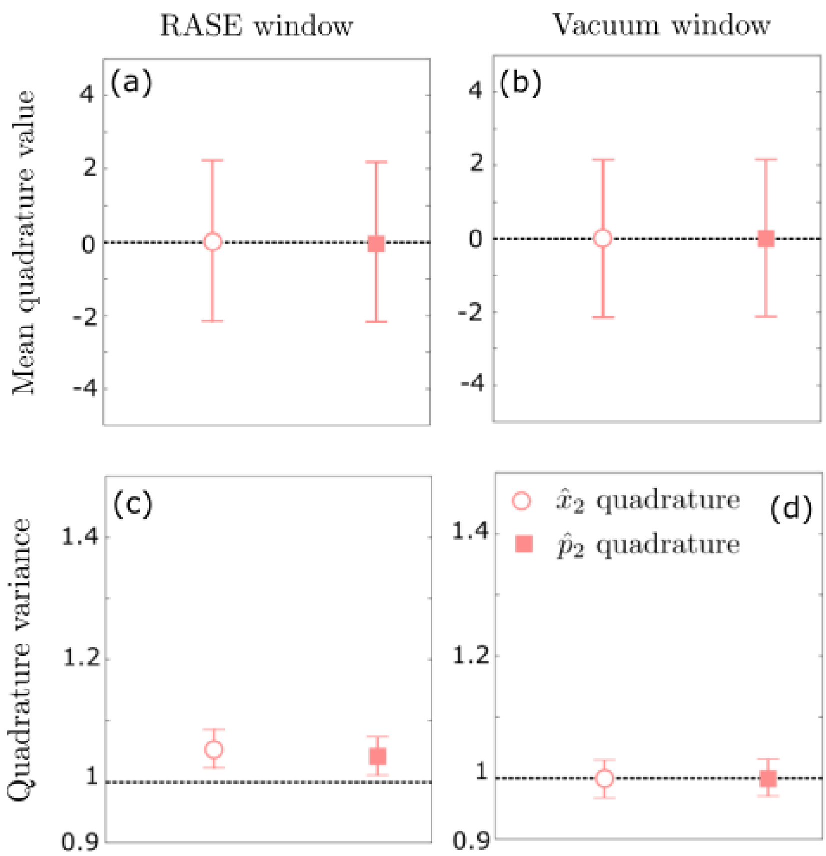

Figure 6.16: Statistics of RASE amplitude $\hat{x}_2$ and phase $\hat{p}_2$ quadrature values, averaged over 15,000 runs of the experiment. The mean of the quadrature values when digitally homodyned at the observed RASE beat frequency, which was 6.95 MHz, are shown in the (a) RASE window, and (b) vacuum window. The variance in the quadrature values in both windows was normalized to the quadrature variance in the vacuum window, and shown for the (c) RASE window and (d) vacuum window. The corresponding analysis of the ASE quadrature values was performed in §5.3.

The 100 μs vacuum window was split into ten sub-windows of 10 μs duration, i.e. ten sub-windows of duration equal to the signal windows. The quadrature values of the vacuum were an average of the values in the sub-windows.

In the vacuum window, the average amplitude and phase quadrature values, when digitally homodyned at the observed RASE beat frequency are shown to be zero in Figure 6.16 (b).

In both windows, the variance in the quadrature values was normalized to the variance in the vacuum window. In Figure 6.16 (d) the quadrature variance in the vacuum window is confirmed to be one. While, in Figure 6.16 (c), the quadrature variance in the RASE window is confirmed to be greater than the vacuum level.

6.3 Calculating the RASE Efficiency from the Ratio of Signal Variances

In §6.1.3 a direct comparison with the inverted four level echo efficiency was achieved with spectral RASE efficiency. However, this comparison was restricted above an optical depth of 1.4. To characterize the efficiency of RASE at smaller optical depths, the ratio of quadrature variances can be used.

To calculate the RASE efficiency from the signal variances, an average of the amplitude and phase quadrature variances are used for the ASE and RASE fields, $\langle \hat{X}_1^2 \rangle$ and $\langle \hat{X}_2^2 \rangle$ respectively. The gain dependency of the RASE variance is compared to the gain dependency of the ASE variance in Figure 6.17. When the ASE variance is well above the model, at an optical depth of 2.7, the RASE variance is also well above the vacuum level.

To calculate the RASE efficiency from the ratio of signal variances η_v, the vacuum level must be subtracted. Because the vacuum level, at the ASE and RASE frequency, was normalized to 1 the efficiency is equal to

$$\eta_v = \frac{\langle \hat{X}_2^2 \rangle - 1}{\langle \hat{X}_1^2 \rangle - 1}, \tag{6.3}$$

where X_i is the average of the amplitude $\hat{x}$ and phase $\hat{p}$ quadratures, and i=1,2 for the ASE and RASE respectively.

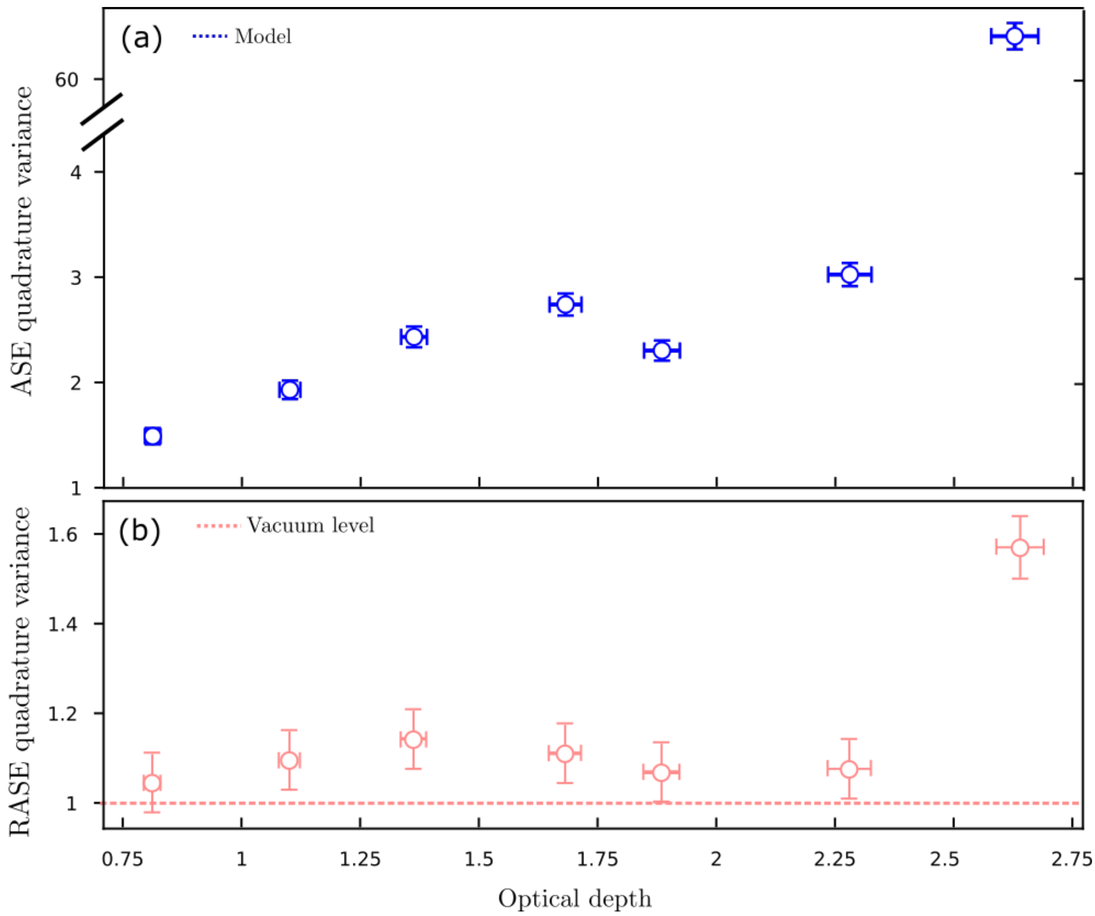

Figure 6.17: Gain dependency of the average (a) ASE quadrature variance $\langle \hat{X}_1^1 \rangle$ compared to the theoretical model (see §3.4.2). The gain dependency of the average (b) RASE quadrature variance $\langle \hat{X}_2^2 \rangle$.

The RASE efficiency, calculated from the signal variances η_v, is shown to be consistent with the spectral result η_s in Figure 6.18.

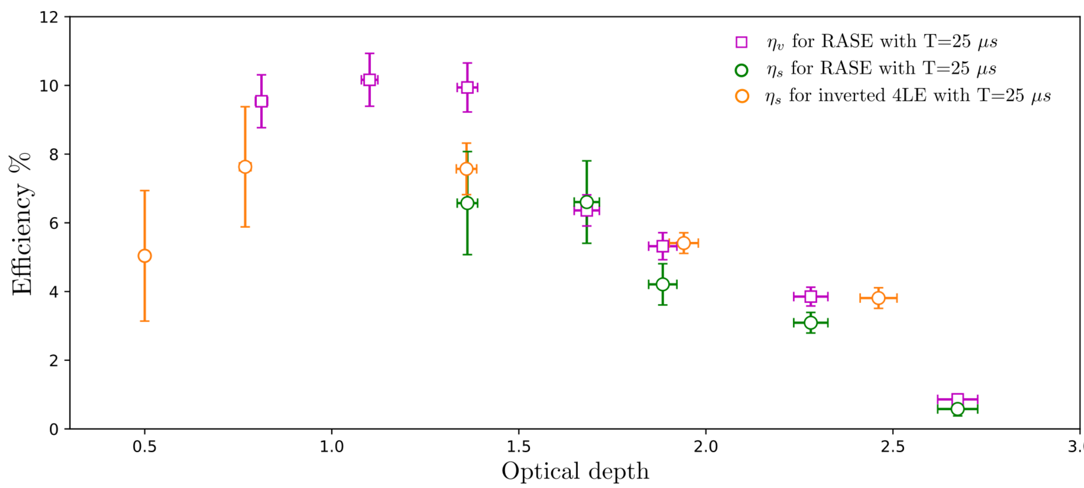

Figure 6.18: RASE efficiency with optical depth (see §5.2.1), calculated from the signal variances η_v and spectral signals η_s. To compared the inverted four level echo (4LE) result, calculated from the ratio of spectral peaks, is scaled to the RASE delay time (T=25 μs) to make a comparison.

In this chapter, the efficiency of RASE was characterized with optical depth using two independent methods: taking the ratio of spectral signal intensities, and taking the ratio of signal variances. Using these two methods, the effect of classical noise, which may be scattered into the RASE mode in the rephasing process (see §3.4.1) will be treated differently. Using the spectrum, the classical noise which varies between each run of the experiment, will be averaged out. In contrast, the efficiency calculation using the signal variances is more susceptible to noise, where any scattered noise will inflate the apparent efficiency. Because the two results agree, this indicates that the rephasing process is occurring *close* to the quantum level (this claim is evaluated more precisely in §7).

According to the theory, the efficiency performance of RASE should consistently improve with optical depth (see §3.4.2). However, experimentally the efficiency was observed to deteriorate when the optical depth exceeded 1. A possible mechanism to explain this is the distortion of the control pulse spatial modes, which will become more significant as the crystal becomes more optically dense.

To investigate the effects of mode distortions, the gain dependency of the ASE variance was measured in Chapter 5. The ASE variance was observed to follow the model until an optical depth of 2.5, after which it began to increase rapidly. This result is consistent with the effects of control pulse distortions becoming significant at large optical densities (see §5.4). However, the RASE mode is dependent on a larger number of control pulses, and therefore, in this chapter effects of mode distortions are observed at a much smaller optical depth of 1.

The RASE protocol is required to operate at a minimum optical depth of 2.5 in order to achieve efficiencies required for a real-world quantum repeater (see §3.4.2). However, in this chapter it was shown that when the optical depth exceeded 1, the efficiency performance began to deteriorate. If a spatial mode distortion is the reason for the performance deterioration, then it will be necessary to adjust the collection modes for the ASE and RASE fields independently. In this work, the RASE experiment was performed in free-space, and therefore, the ASE field is emitted in an infinite number of modes (see §5.4 for details). This makes it difficult to understand how the emitted ASE modes map to the emitted RASE modes, and correct for any distortions. In contrast, if ASE was emitted into one precisely defined mode, the experiment could be designed such that the single emitted RASE mode efficiently coupled into the collection fiber at an optical depth exceeding 2.5.

6.4 Summary

In this chapter, the efficiency of the inverted four level echo was shown to be consistent with RASE for a range of optical depths. In the first instance, both were calculated using the spectral signals. In the second instance, the RASE efficiency was re-calculated using the signal variances. Using both approaches, the efficiency of RASE with optical depth was shown to be similar. This result suggests that the rephasing process, in the RASE protocol, is operating *very close* to the quantum level. This claim is evaluated more precisely in Chapter 7, by comparing the theoretical and experimental inseparability curves. Finally, the efficiency of RASE was shown to deteriorate at an optical depth of 1. This is consistent the RASE modes being more strongly affected, when compared to the ASE modes (see §5.4), by distortions in the control pulses. This suggests, that for RASE to operate at the optical depths required for a repeater protocol, which should exceed 2.5, these distortions must be corrected for.

Chapter 7

The Inseparability Criterion

The main feature which separates a trusted node network from a quantum repeater network is how information is stored in the distribution process. For a quantum repeater, the non-classical nature of the information is maintained throughout the storage phase. A quantum repeater, which is based on rephased amplified spontaneous emission, stores information on the collective state of an ensemble of rare-earth ions. When amplified spontaneous emission (ASE) is detected the state is heralded into a superposition state of any atom having decayed. Because the coherence times in rare earth ions are long, information about this state can be read out as a second light field, after a controlled delay time. As a consequence, the two emitted fields of light will be entangled with each other (see §3.1). In this thesis, the inseparability criterion was chosen to assess whether the emitted fields are non-classically correlated, i.e. entangled. Therefore, the quadrature variances of the ASE and RASE fields must be determined over a *time* window where we expect to observe a correlation (see §3.3).

For a single run of the experiment, the two signal windows are integrated over giving an *average* value for the ASE and RASE quadratures (both amplitude and phase). In Chapter 5 and Chapter 6, the window duration was matched by the inverse of the gain profile full width half maximum (G_{FWHM}) (see §6.2 for details). This window was chosen because, on time scales comparable to this, the quadrature values are not expected to average to zero. However, if the window is too large, quantum correlations will be washed-out, and classical correlations are likely to dominate.

In this chapter, the assumption that a window duration which is *matched* to G_{FWHM} maximizes the non-classical correlation between the ASE and RASE fields is assessed. This was evaluated by reducing the window duration from the matched condition and characterizing the inseparability criterion. This was done in two optical depth regimes: a low optical depth regime, 0.8; and a medium optical depth regime, 1.6. In both cases, the non-classical result was maximized when the matched condition was roughly halved (i.e. $\sim \frac{G_{FWHM}}{2}$).

7.1 Low Optical Depth Regime

At an optical depth of 0.8, the duration of the time window was matched to the inverse of the gain profile FWHM using a 9 μs duration top-hat function T_h (see §6.2 for details). In Figure 7.1 the duration of the top-hat function was reduced, and the position of the inseparability curve minimum was recorded. Matching the window to the inverse of the gain profile FWHM, i.e. using T_h=9 μs, the correlation was classical. Reducing the top-hat duration to 5 μs the confidence level in a non-classical result was maximized at 2.2σ. This result was an average over first 8,600 repetitions of the experiment, which was a subgroup of the complete 15,000. The subgroup was averaged over, instead of the complete set, because non-classical result was observed to improve. Because the complete set was collected over several hours, this was most likely the effect of an alignment drift in the experiment.

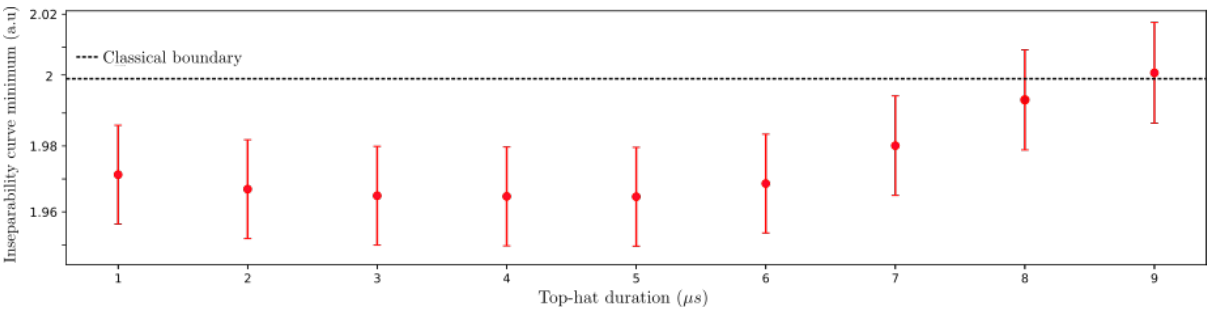

Figure 7.1: The position of the inseparability curve minimum for varying duration time windows. The duration of the windows was changed by adjusting the duration of the top-hat function T_h (see §6.2 for details). For these measurements the frequency filter was centered at the ASE and RASE spectral peak frequencies, f_A=12.55 and f_R=6.95 MHz respectively (see §6.2). The results are an average over 8,600 repetitions of the experiment, and shown with a 1σ confidence level.

In Figure 7.2 (a), the experimental and theoretical inseparability curves are compared using two different time windows to calculate the quadrature values. Firstly, when the duration of the window was *matched* the inverse of the gain profile FWHM, i.e. using T_h=9 μs; and secondly, when the duration of the window *optimized* the non-classical confidence level, i.e. using T_h=5 μs. Using the *matched* window the two curves were inconsistent, with the theory predicting a non-classical result. Using the *optimized* window, the two results were consistent, both giving a non-classical result with a 2.2σ confidence level.

In Chapter 6 the efficiency of RASE was calculated by matching the window duration to the inverse of the gain profile FWHM. Recalculating the efficiency using a time window which maximized the non-classical result, i.e. using T_h=5 μs, the result was reduced by 28%, summarized in Table 7.1.

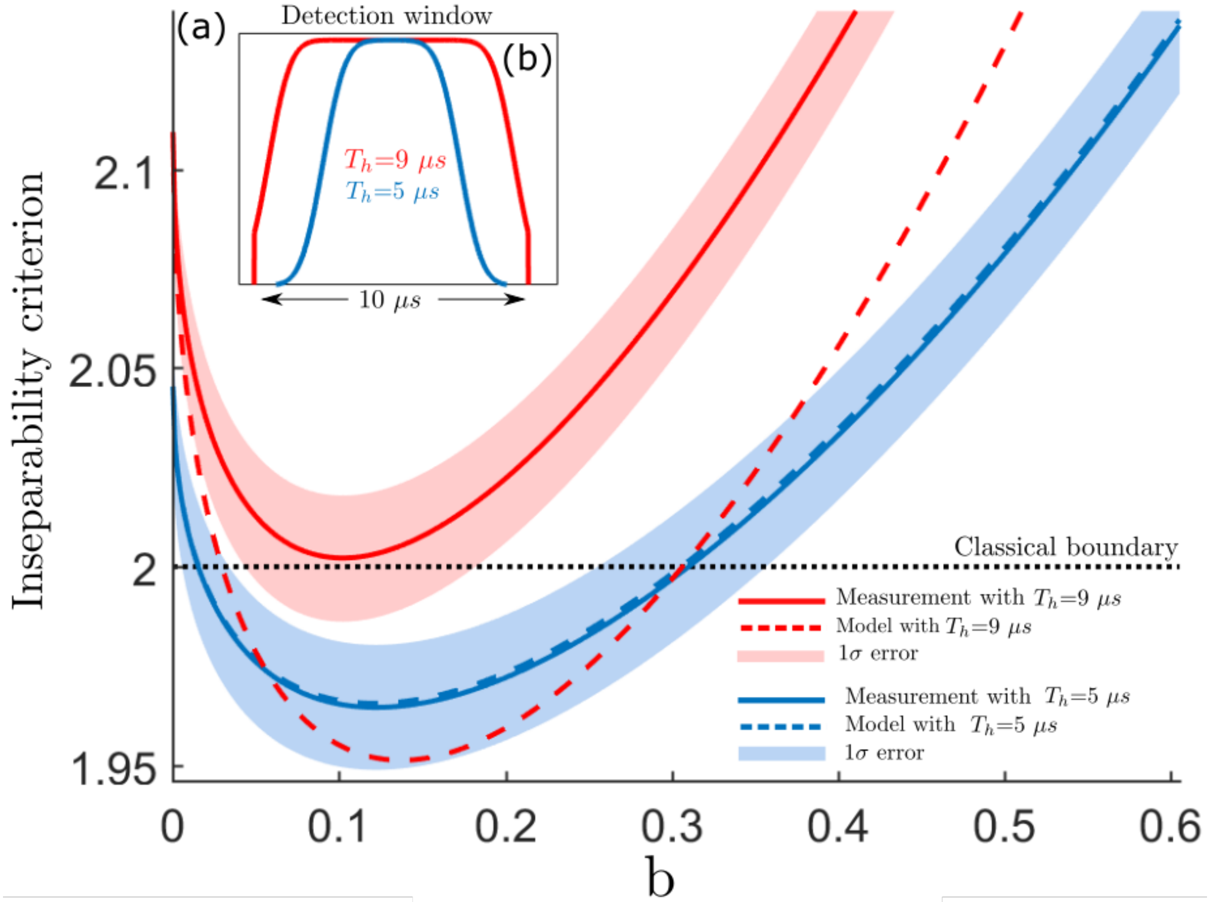

Figure 7.2: (a) Experimental and theoretical inseparability curves with the weighting parameter b, where different duration time windows have been used to calculate the quadrature values. The time window was changed by adjusting the duration of the top-hat function T_h (see §6.2 for details). The experimental and theoretical curves are shown for: a time window which was matched to the inverse of the gain profile FWHM, which used T_h=9 μs; and a time window which maximized the confidence level in a non-classical result, which used T_h=5 μs. The experimental results are an average over 8,600 repetitions of the experiment, and the frequency filter was centered at the ASE and RASE spectral peak frequencies: f_A=12.55 and f_R=6.95 MHz respectively. The shape of the time windows are shown in (b).

	Matched	Optimized
T_h (μs)	9	5
η_v(%)	11.6 $\pm$ 0.3	8.3 $\pm$ 0.2
Confidence	-0.14σ	2.21σ

Table 7.1: Properties of RASE using two different duration time windows to calculate the quadrature values. The time window was changed by adjusting the duration of the top-hat function T_h (see §6.2 for details). The comparison was made using a time window which is *matched* to the inverse of the gain profile FWHM, which used T_h=9 μs; and a time window which maximized the confidence level in a non-classical result, which used T_h=5 μs. Note that a negative confidence level indicates that the inseparability minimum is above the classical boundary (equal to 2). The properties compared are the efficiency of RASE, calculated from the signal variances η_v (see §6.3), and the confidence level in a non-classical result. The results were an average over 8,600 repetitions of the experiment, and center of the spectral filters are set to where the spectral peaks were observed, f_A=12.55 and f_R=6.95 MHz for ASE and RASE respectively.

7.2 Medium Optical Depth Regime

At an optical depth of 1.6, the duration of the time window was matched to the inverse of the gain profile FWHM using a 7 μs duration top-hat function T_h (see §6.2 for details). In Figure 7.3 the duration of the top-hat function was reduced, and the position of the inseparability curve minimum was recorded. Matching the window duration to the inverse of the gain profile FWHM, i.e. using T_h = 7 μs, the correlation was classical. Reducing the window duration, the confidence level in a non-classical result was maximized at 1.3σ, when a top-hat duration of 3 μs was used.

In Figure 7.4 (a), the experimental and theoretical inseparability curves are compared using two different time windows to calculate the quadrature values. Firstly, when the duration of the window was *matched* to the inverse of the gain profile FWHM, i.e. using T_h = 7 μs; and secondly, when the duration of the window *optimized* the non-classical confidence level, i.e. using T_h = 3 μs. Using a *matched* window, the two curves are inconsistent, with the theory predicting a non-classical result. Using the *optimized* window, the two results are consistent, both giving a non-classical result with a 1.3σ confidence level.

In Chapter 6 the efficiency of RASE was calculated using a window duration which matched the inverse of the gain profile FWHM. Recalculating the efficiency using the time window which maximized the non-classical result, i.e. using T_h = 3 μs, the result was reduced by 54%, summarized in Table 7.2

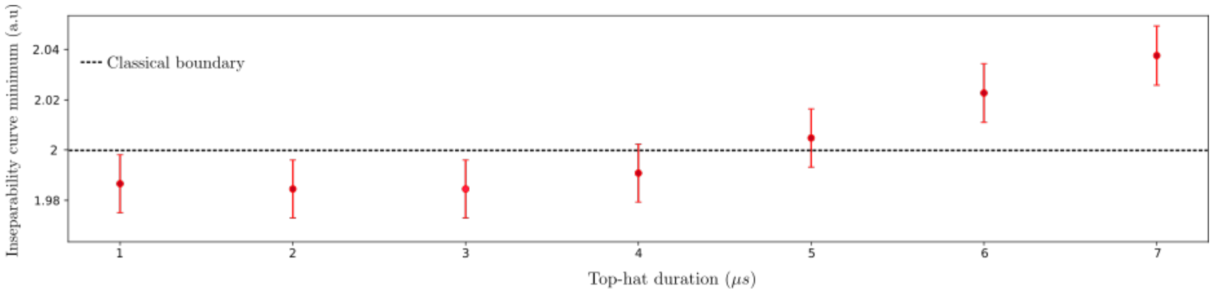

Figure 7.3: The position of the inseparability curve minimum for varying duration time windows. The duration of the windows was changed by adjusting the duration of the top-hat function T_h (see §6.2 for details). For these measurements the frequency filter was centered at the ASE and RASE spectral peak frequencies, f_A = 12.51 and f_R = 6.91 MHz respectively (see §6.2). The results are an average over 15,000 repetitions of the experiment, and shown with a 1σ confidence level.

	Matched	Optimized
T_h (μs)	7	3
η_v (%)	6.8 ± 0.1	3.1 ± 0.1
Confidence	-3.11σ	1.27σ

Table 7.2: Properties of RASE when different time windows are used to calculate the quadrature values. The time window was changed by adjusting the duration of the top-hat function T_h (see §6.2 for details). A comparison is made using a time window which is *matched* to the inverse of the gain profile FWHM, which used T_h = 7 μs; and a time window which maximized the confidence level in a non-classical result, which used T_h = 3 μs. Note that a negative confidence level indicates that the inseparability minimum is above the classical boundary (equal to 2). The properties compared are the efficiency of RASE, calculated from the signal variances η_v (see §6.3), and the confidence level in a non-classical result. The results were an average over 15,000 repetitions of the experiment, and center of the spectral filters are set to where the spectral peaks were observed, f_A = 12.51 and f_R = 6.91 MHz for ASE and RASE respectively.

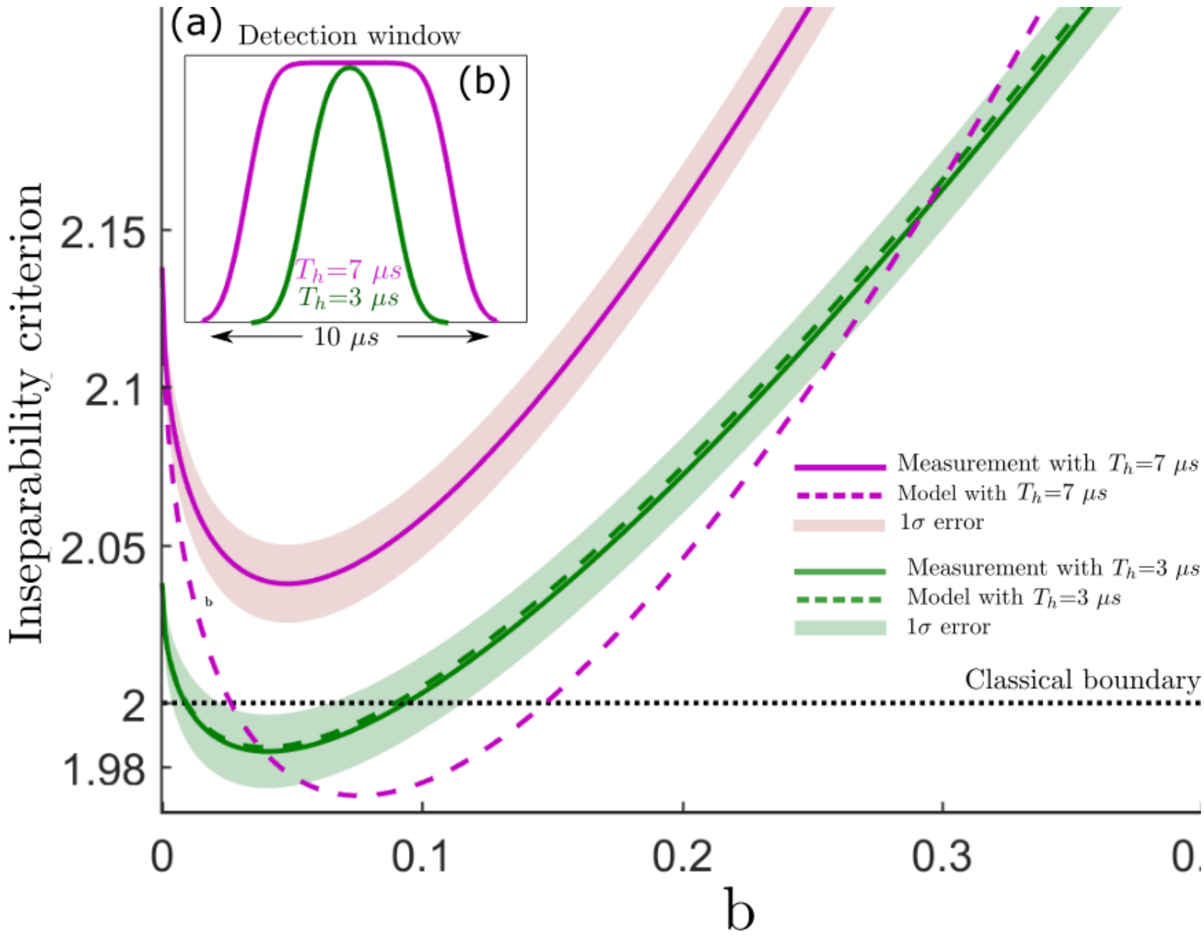

Figure 7.4: Experimental and theoretical inseparability curves with the weighting parameter b, where different duration time windows have been used to calculate the quadrature values. The time window was changed by adjusting the duration of the top-hat function T_h (see §6.2 for details). The experimental and theoretical curves are shown for: a time window which was matched to the inverse of the gain profile FWHM, which used $T_h = 7\ \mu s$; and a time window which maximized the confidence level in a non-classical result, which used $T_h = 3\ \mu s$. The experimental results are an average over 15,000 repetitions of the experiment, and the frequency filter was centered at the ASE and RASE spectral peak frequencies: $f_A = 12.51$ and $f_R = 6.91$ MHz respectively. The shape of the time windows are shown in (b).

In Chapter 6 the RASE efficiency was calculated using two methods: using the signal variances η_v, and using signal spectrum η_s. The consistency between the two results suggested that *very little* classical noise was scattered into the RASE experiment. However, using the inseparability criterion is a more precise way to characterize the level of classical noise in the experiment.

In this chapter, the inseperability curve was shown to be dependent on the duration of the time window used to calculate the quadrature values. This dependency was similar both an optical depth of 0.8 and 1.6. When the duration of the temporal window was matched to the inverse of the gain profile FWHM (which was the method used in Chapter 5 and Chapter 6), the correlation was classical, and not consistent with the theory. When the window duration was roughly halved, a non-classical correlation was observed which was consistent with the theory. In addition, decreasing the temporal window lead to a decrease in the calculated RASE efficiency η_v.

This result is consistent with the theory that classical noise will be introduced into the experiment via scattering into the RASE modes (see §3.4). Altogether, this suggests that classical noise, on the RASE modes, can be filtered out by careful selection of the time window used to calculate the quadrature values. In this thesis the time window remained centered in the 10 μs long detection windows. In future work, the the non-classical correlation could be improved by displacing the time windows closer to the rephasing pulses, illustrated in Figure 7.5.

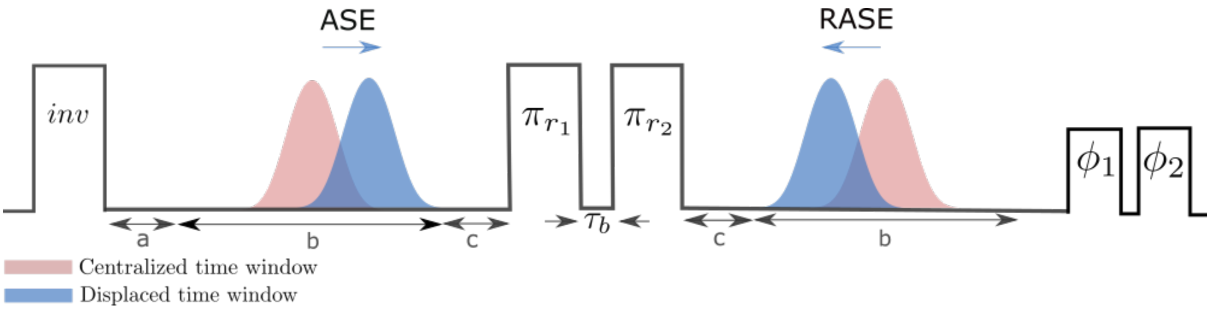

Figure 7.5: The temporal pulse sequence, delays and signal detection windows used for RASE experiment. To calculate the quadrature values of the ASE and RASE fields, the detection windows were shaped and integrated over. For all calculations in this thesis, shaped windows were centralized in the detection windows of duration b. In future work, the windows could be symmetrically displaced to investigate the effect this has on the ASE and RASE field correlation.

7.3 Summary

In this chapter, the assumption that a window duration, which is *matched* to the inverse of the gain profile full width half maximum (G_{FWHM}), will maximize the non-classical correlation between the ASE and RASE fields was evaluated. This assumption was used in Chapter 6, to calculate the RASE efficiency from the signal variances, with the result suggesting that *very little* classical noise was present in the RASE experiment. In this chapter, the inseparability criterion was used to evaluate the level of classical noise more precisely. Using the inseparability curve, the non-classical result was maximized when the window duration was roughly halved from the matched condition (i.e. $\sim \frac{G_{FWHM}}{2}$). Recalculating the RASE efficiency with the reduced window suggested that the method used in Chapter 6 slightly overestimated the efficiency results. In addition, the overestimation was shown to be gain dependent, increasing from 28% to 54% between an optical depth of 0.8 and 1.6. Overall, the result suggests that to reliably calculate the RASE efficiency, from the signal variances, a window duration much shorter than the inverse of the gain profile FWHM must be used.

Chapter 8

Conclusion

In this thesis the efficiency of a quantum memory, in a rare-earth ion-doped crystal, was characterized for quantum repeater applications. The approach taken here was to use a memory protocol which incorporates an entangled light source using rephased amplified spontaneous emission (RASE).

In RASE, a two level atomic ensemble is inverted to create optical gain. This gain amplifies the vacuum fluctuations inside the crystal and generates amplified spontaneous emission (ASE). Detection of the emitted field heralds the ensemble into a state which is entangled with ASE. Because the coherence times in rare-earth ion-doped crystals are long, the entanglement can be read out as a second optical field, after a controlled delay time.

In this thesis, the efficiency of RASE was investigated with optical depth. In the regime where the two fields were entangled, the efficiency was maximized at 8.3% when the optical depth was 0.8. However, beyond an optical depth of 1, the efficiency began to deteriorate. This is not consistent with the theory, which predicts that the efficiency of RASE should consistently improve with optical depth. The theory also suggests that at an optical depth of 2.5, an efficiency of 90% should be achieved; which is the threshold efficiency for a quantum repeater. Experimentally, however, at this optical depth, the efficiency of RASE was observed to be effectively zero. Therefore, currently as the RASE protocol stands, it does not meet the efficiency requirements for quantum repeater applications.

In this thesis, I proposed that the mechanism limiting the efficiency of RASE, with optical depth, was the spatial distortion of the control pulses. The outcome of this work, therefore, is that in order for RASE to operate efficiently at an optical depth of 2.5, the experiment must be designed to correct for the effects of these distortions.

Bibliography

1. K. R. Ferguson, S. E. Beavan, J. J. Longdell, and M. J. Sellars, "Generation of Light with Multimode Time-Delayed Entanglement Using Storage in a Solid-State Spin-Wave Quantum Memory," *Physical Review Letters*, vol. 117, no. 2, 2016. (cited on pages vii, 14, 47, and 48)

2. S. Singh, *The Code Book: The Science of Secrecy from Ancient Egyptto Quantum Cryptography*. New York: Anchor Books, 2000. (cited on page 1)

3. A. Hiltgen, T. Kramp, and T. Weigold, "Secure Internet banking authentication," *IEEE Security & Privacy Magazine*, vol. 4, no. 2, pp. 21–29, 2006. (cited on page 1)

4. V. B. Liwandouw and A. D. Wowor, "The Existence Of Cryptography: A Study On Instant Messaging," *Procedia Computer Science*, vol. 124, pp. 721–727, 2017. (cited on page 1)

5. H. Feistel, "Cryptography and Computer Privacy," *Scientific American*, vol. 228, no. 5, pp. 15–23, 1973. (cited on page 1)

6. W. Diffie, "The first ten years of public-key cryptography," *Proceedings of the IEEE*, vol. 76, no. 5, pp. 560–577, 1988. (cited on page 1)

7. W. Diffie and M. Hellman, "New directions in cryptography," *IEEE Transactions on Information Theory*, vol. 22, no. 6, pp. 644–654, 1976. (cited on page 1)

8. R. L. Rivest, A. Shamir, and L. Adleman, "A Method for Obtaining Digital Signatures and Public-key Cryptosystems," *Commun. ACM*, vol. 21, no. 2, pp. 120–126, 1978. (cited on page 2)

9. M. Gardner, "MATHEMATICAL GAMES," *Scientific American*, vol. 222, no. 6, pp. 132–140, 1970. (cited on page 2)

10. D. Atkins, M. Graff, A. K. Lenstra, and P. C. Leyland, "The magic words are squeamish ossifrage," in *Advances in Cryptology — ASIACRYPT'94* (J. Pieprzyk and R. Safavi-Naini, eds.), Lecture Notes in Computer Science, pp. 261–277, Springer Berlin Heidelberg, 1995. (cited on page 2)

11. C. H. Bennett, G. Brassard, C. Crépeau, R. Jozsa, A. Peres, and W. K. Wootters, "Teleporting an unknown quantum state via dual classical and Einstein-Podolsky-Rosen channels," *Physical Review Letters*, vol. 70, no. 13, pp. 1895–1899, 1993. (cited on page 2)

12. P. M. Ledingham, W. R. Naylor, J. J. Longdell, S. E. Beavan, and M. J. Sellars, "Nonclassical photon streams using rephased amplified spontaneous emission," *Physical Review A*, vol. 81, no. 1, 2010. (cited on pages 2, 13, 37, and 38)

13. A. Einstein, B. Podolsky, and N. Rosen, "Can Quantum-Mechanical Description of Physical Reality Be Considered Complete?," *Physical Review*, vol. 47, pp. 777–780, 1935. (cited on pages 3 and 41)

14. J. Bell, "ON THE EINSTEIN PODOLSKY ROSEN PARADOX," *Physics (Long Island City, N.Y.)*, vol. 1, no. 3, pp. 195–290, 1964. (cited on page 3)

15. M. Giustina, M. A. M. Versteegh, S. Wengerowsky, J. Handsteiner, A. Hochrainer, K. Phelan, F. Steinlechner, J. Kofler, J.-Å. Larsson, C. Abellán, W. Amaya, V. Pruneri, M. W. Mitchell, J. Beyer, T. Gerrits, A. E. Lita, L. K. Shalm, S. W. Nam, T. Scheidl, R. Ursin, B. Wittmann, and A. Zeilinger, "Significant-loophole-free test of Bell's theorem with entangled photons," *Physical Review Letters*, vol. 115, no. 25, 2015. (cited on page 3)

16. C. H. Bennett and G. Brassard, "Quantum cryptography: Public key distribution and coin tossing," *Theoretical Computer Science*, vol. 560, pp. 7–11, 2014. (cited on page 4)

17. A. K. Ekert, "Quantum cryptography based on Bell's theorem," *Physical Review Letters*, vol. 67, no. 6, pp. 661–663, 1991. (cited on page 4)

18. D. Bruß, "Optimal Eavesdropping in Quantum Cryptography with Six States," *Physical Review Letters*, vol. 81, no. 14, pp. 3018–3021, 1998. (cited on page 4)

19. C. H. Bennett, F. Bessette, G. Brassard, L. Salvail, and J. Smolin, "Experimental quantum cryptography," *Journal of Cryptology*, vol. 5, no. 1, pp. 3–28, 1992. (cited on page 4)

20. A. K. Ekert, J. G. Rarity, P. R. Tapster, and G. Massimo Palma, "Practical quantum cryptography based on two-photon interferometry," *Physical Review Letters*, vol. 69, no. 9, pp. 1293–1295, 1992. (cited on page 4)

21. N. Gisin, G. Ribordy, W. Tittel, and H. Zbinden, "Quantum cryptography," *Reviews of Modern Physics*, vol. 74, no. 1, pp. 145–195, 2002. (cited on page 4)

22. B. Korzh, C. C. W. Lim, R. Houlmann, N. Gisin, M. J. Li, D. Nolan, B. Sanguinetti, R. Thew, and H. Zbinden, "Provably secure and practical quantum key distribution over 307 km of optical fibre," *Nature Photonics*, vol. 9, no. 3, p. 163, 2015. (cited on page 5)

23. N. Sangouard, C. Simon, H. de Riedmatten, and N. Gisin, "Quantum repeaters based on atomic ensembles and linear optics," *Reviews of Modern Physics*, vol. 83, no. 1, pp. 33–80, 2011. (cited on pages 5, 8, 12, and 14)

24. M. Peev, C. Pacher, R. Alléaume, C. Barreiro, J. Bouda, W. Boxleitner, T. Debuisschert, E. Diamanti, M. Dianati, J. F. Dynes, S. Fasel, S. Fossier, M. Fürst, J.-D. Gautier, O. Gay, N. Gisin, P. Grangier, A. Happe, Y. Hasani, M. Hentschel, H. Hübel, G. Humer, T. Länger, M. Legré, R. Lieger, J. Lodewyck, T. Lorünser, N. Lütkenhaus, A. Marhold, T. Matyus, O. Maurhart, L. Monat, S. Nauerth, J.-B. Page, A. Poppe, E. Querasser, G. Ribordy, S. Robyr, L. Salvail, A. W. Sharpe, A. J. Shields, D. Stucki, M. Suda, C. Tamas, T. Themel, R. T. Thew, Y. Thoma, A. Treiber, P. Trinkler, R. Tualle-Brouri, F. Vannel, N. Walenta, H. Weier, H. Weinfurter, I. Wimberger, Z. L. Yuan, H. Zbinden, and A. Zeilinger, "The SECOQC quantum key distribution network in Vienna," *New Journal of Physics*, vol. 11, no. 7, p. 075001, 2009. (cited on page 5)

25. S. Wang, W. Chen, Z.-Q. Yin, H.-W. Li, D.-Y. He, Y.-H. Li, Z. Zhou, X.-T. Song, F.-Y. Li, D. Wang, H. Chen, Y.-G. Han, J.-Z. Huang, J.-F. Guo, P.-L. Hao, M. Li, C.-M. Zhang, D. Liu, W.-Y. Liang, C.-H. Miao, P. Wu, G.-C. Guo, and Z.-F. Han, "Field and long-term demonstration of a wide area quantum key distribution network," *Optics Express*, vol. 22, no. 18, pp. 21739–21756, 2014. (cited on page 5)

26. S.-K. Liao, W.-Q. Cai, J. Handsteiner, B. Liu, J. Yin, L. Zhang, D. Rauch, M. Fink, J.-G. Ren, W.-Y. Liu, Y. Li, Q. Shen, Y. Cao, F.-Z. Li, J.-F. Wang, Y.-M. Huang, L. Deng, T. Xi, L. Ma, T. Hu, L. Li, N.-L. Liu, F. Koidl, P. Wang, Y.-A. Chen, X.-B. Wang, M. Steindorfer, G. Kirchner, C.-Y. Lu, R. Shu, R. Ursin, T. Scheidl, C.-Z. Peng, J.-Y. Wang, A. Zeilinger, and J.-W. Pan, "Satellite-Relayed Intercontinental Quantum Network," *Physical Review Letters*, vol. 120, no. 3, p. 030501, 2018. (cited on page 5)

27. M. D. Lukin, "Colloquium : Trapping and manipulating photon states in atomic ensembles," *Reviews of Modern Physics*, vol. 75, no. 2, pp. 457–472, 2003. (cited on page 6)

28. W. Tittel, M. Afzelius, R. L. Cone, T. Chanelière, S. Kröll, S. A. Moiseev, and M. Sellars, "Photon-Echo Quantum Memory," *arXiv:0810.0172 [quant-ph]*, 2008. (cited on page 6)

29. B. Huttner, N. Imoto, N. Gisin, and T. Mor, "Quantum cryptography with coherent states," *Physical Review A*, vol. 51, no. 3, pp. 1863–1869, 1995. (cited on page 6)

30. G. Brassard, N. Lütkenhaus, T. Mor, and B. C. Sanders, "Limitations on Practical Quantum Cryptography," *Physical Review Letters*, vol. 85, no. 6, pp. 1330–1333, 2000. (cited on page 6)

31. M. E. Reimer and C. Cher, "The quest for a perfect single-photon source," *Nature Photonics*, vol. 13, no. 11, pp. 734–736, 2019. (cited on page 6)

32. C. K. Hong and L. Mandel, "Experimental realization of a localized one-photon state," *Physical Review Letters*, vol. 56, no. 1, pp. 58–60, 1986. (cited on page 6)

33. L.-M. Duan, M. D. Lukin, J. I. Cirac, and P. Zoller, "Long-distance quantum communication with atomic ensembles and linear optics," *Nature*, vol. 414, no. 6862, pp. 413–418, 2001. (cited on page 7)

34. L. Jiang, J. M. Taylor, and M. D. Lukin, "Fast and robust approach to long-distance quantum communication with atomic ensembles," *Physical Review A*, vol. 76, no. 1, 2007. (cited on page 7)

35. Z.-B. Chen, B. Zhao, Y.-A. Chen, J. Schmiedmayer, and J.-W. Pan, "Fault-tolerant quantum repeater with atomic ensembles and linear optics," *Physical Review A*, vol. 76, no. 2, 2007. (cited on page 7)

36. J. Simon, H. Tanji, J. K. Thompson, and V. Vuletić, "Interfacing Collective Atomic Excitations and Single Photons," *Physical Review Letters*, vol. 98, no. 18, 2007. (cited on page 7)

37. N. Sangouard, C. Simon, J. Minář, H. Zbinden, H. de Riedmatten, and N. Gisin, "Long-distance entanglement distribution with single-photon sources," *Physical Review A*, vol. 76, no. 5, 2007. (cited on page 7)

38. C. Simon, M. Afzelius, J. Appel, A. Boyer de la Giroday, S. J. Dewhurst, N. Gisin, C. Y. Hu, F. Jelezko, S. Kröll, J. H. Müller, J. Nunn, E. S. Polzik, J. G. Rarity, H. De Riedmatten, W. Rosenfeld, A. J. Shields, N. Sköld, R. M. Stevenson, R. Thew, I. A. Walmsley, M. C. Weber, H. Weinfurter, J. Wrachtrup, and R. J. Young, "Quantum memories: A review based on the European integrated project "Qubit Applications (QAP)"," *The European Physical Journal D*, vol. 58, no. 1, pp. 1–22, 2010. (cited on page 8)

39. B. Albrecht, P. Farrera, G. Heinze, M. Cristiani, and H. de Riedmatten, "Controlled Rephasing of Single Collective Spin Excitations in a Cold Atomic Quantum Memory," *Physical Review Letters*, vol. 115, no. 16, p. 160501, 2015. (cited on pages 8 and 14)

40. A. I. Lvovsky, B. C. Sanders, and W. Tittel, "Optical quantum memory," *Nature Photonics*, vol. 3, no. 12, p. nphoton.2009.231, 2009. (cited on page 8)

41. S. E. Harris, J. E. Field, and A. Imamoğlu, "Nonlinear optical processes using electromagnetically induced transparency," *Physical Review Letters*, vol. 64, no. 10, pp. 1107–1110, 1990. (cited on page 9)

42. M. Nilsson and S. Kröll, "Solid state quantum memory using complete absorption and re-emission of photons by tailored and externally controlled inhomogeneous absorption profiles," *Optics Communications*, vol. 247, no. 4, pp. 393–403, 2005. (cited on page 9)

43. M. Afzelius, C. Simon, H. de Riedmatten, and N. Gisin, "Multimode quantum memory based on atomic frequency combs," *Physical Review A*, vol. 79, no. 5, 2009. (cited on pages 9 and 30)

44. D. L. McAuslan, P. M. Ledingham, W. R. Naylor, S. E. Beavan, M. P. Hedges, M. J. Sellars, and J. J. Longdell, "Photon-echo quantum memories in inhomogeneously broadened two-level atoms," *Physical Review A*, vol. 84, no. 2, 2011. (cited on pages 9 and 30)

45. V. Damon, M. Bonarota, A. Louchet-Chauvet, T. Chanelière, and J.-L. L. Gouët, "Revival of silenced echo and quantum memory for light," *New Journal of Physics*, vol. 13, no. 9, p. 093031, 2011. (cited on pages 9 and 30)

46. J. Fekete, D. Rieländer, M. Cristiani, and H. de Riedmatten, "Ultranarrow-Band Photon-Pair Source Compatible with Solid State Quantum Memories and Telecommunication Networks," *Physical Review Letters*, vol. 110, no. 22, 2013. (cited on page 9)

47. S. E. Beavan, M. P. Hedges, and M. J. Sellars, "Demonstration of Photon-Echo Rephasing of Spontaneous Emission," *Physical Review Letters*, vol. 109, no. 9, 2012. (cited on pages 9, 30, 32, and 47)

48. H.-J. Briegel, W. Dür, J. I. Cirac, and P. Zoller, "Quantum repeaters: The role of imperfect local operations in quantum communication," *Physical Review Letters*, vol. 81, no. 26, p. 5932, 1998. (cited on page 10)

49. C. Cabrillo, J. I. Cirac, P. García-Fernández, and P. Zoller, "Creation of entangled states of distant atoms by interference," *Physical Review A*, vol. 59, no. 2, pp. 1025–1033, 1999. (cited on page 10)

50. S. Bose, P. L. Knight, M. B. Plenio, and V. Vedral, "Proposal for Teleportation of an Atomic State via Cavity Decay," *Physical Review Letters*, vol. 83, no. 24, pp. 5158–5161, 1999. (cited on page 10)

51. M. Żukowski, A. Zeilinger, M. A. Horne, and A. K. Ekert, ""Event-ready-detectors" Bell experiment via entanglement swapping," *Physical Review Letters*, vol. 71, no. 26, pp. 4287–4290, 1993. (cited on page 10)

52. S. E. Beavan, *Photon-Echo Rephasing of Spontaneous Emission from an Ensemble of Rare-Earth Ions*. PhD Thesis, The Australian National University, 2012. (cited on pages 12, 41, and 82)

53. E. Saglamyurek, M. Grimau Puigibert, Q. Zhou, L. Giner, F. Marsili, V. B. Verma, S. Woo Nam, L. Oesterling, D. Nippa, D. Oblak, and W. Tittel, "A multiplexed light-matter interface for fibre-based quantum networks," *Nature Communications*, vol. 7, p. 11202, 2016. (cited on page 12)

54. O. A. Collins, S. D. Jenkins, A. Kuzmich, and T. A. B. Kennedy, "Multiplexed Memory-Insensitive Quantum Repeaters," *Physical Review Letters*, vol. 98, no. 6, 2007. (cited on page 12)

55. C. Simon, H. de Riedmatten, M. Afzelius, N. Sangouard, H. Zbinden, and N. Gisin, "Quantum Repeaters with Photon Pair Sources and Multimode Memories," *Physical Review Letters*, vol. 98, no. 19, 2007. (cited on page 12)

56. M. Rančić, M. P. Hedges, R. L. Ahlefeldt, and M. J. Sellars, "Coherence time of over a second in a telecom-compatible quantum memory storage material," *Nature Physics*, vol. 14, no. 1, pp. 50–54, 2018. (cited on page 13)

57. M. Zhong, M. P. Hedges, R. L. Ahlefeldt, J. G. Bartholomew, S. E. Beavan, S. M. Wittig, J. J. Longdell, and M. J. Sellars, "Optically addressable nuclear spins in a solid with a six-hour coherence time," *Nature*, vol. 517, no. 7533, pp. 177–180, 2015. (cited on page 13)

58. F. Kaneda, F. Xu, J. Chapman, and P. G. Kwiat, "Quantum-memory-assisted multi-photon generation for efficient quantum information processing," *Optica*, vol. 4, no. 9, p. 1034, 2017. (cited on page 14)

59. F. Bussières, C. Clausen, A. Tiranov, B. Korzh, V. B. Verma, S. W. Nam, F. Marsili, A. Ferrier, P. Goldner, H. Herrmann, C. Silberhorn, W. Sohler, M. Afzelius, and N. Gisin, "Quantum teleportation from a telecom-wavelength photon to a solid-state quantum memory," *Nature Photonics*, vol. 8, no. 10, pp. 775–778, 2014. (cited on page 14)

60. M. P. Hedges, J. J. Longdell, Y. Li, and M. J. Sellars, "Efficient quantum memory for light," *Nature*, vol. 465, no. 7301, pp. 1052–1056, 2010. (cited on page 14)

61. A. E. Lita, A. J. Miller, and S. W. Nam, "Counting near-infrared single-photons with 95% efficiency," *Optics Express*, vol. 16, no. 5, p. 3032, 2008. (cited on page 14)

62. C. Laplane, P. Jobez, J. Etesse, N. Gisin, and M. Afzelius, "Multimode and Long-Lived Quantum Correlations Between Photons and Spins in a Crystal," *Physical Review Letters*, vol. 118, no. 21, 2017. (cited on page 14)

63. A. Seri, A. Lenhard, D. Rieländer, M. Gündoğan, P. M. Ledingham, M. Mazzera, and H. de Riedmatten, "Quantum Correlations between Single Telecom Photons and a Multimode On-Demand Solid-State Quantum Memory," *Physical Review X*, vol. 7, no. 2, p. 021028, 2017. (cited on page 14)

64. M. Hosseini, B. M. Sparkes, G. Campbell, P. K. Lam, and B. C. Buchler, "High efficiency coherent optical memory with warm rubidium vapour," *Nature Communications*, vol. 2, p. 174, 2011. (cited on page 14)

65. R. N. Stevenson, M. R. Hush, A. R. R. Carvalho, S. E. Beavan, M. J. Sellars, and J. J. Hope, "Single photon production by rephased amplified spontaneous emission," *New Journal of Physics*, vol. 16, no. 3, p. 033042, 2014. (cited on pages 14 and 19)

66. M. Kucuker and K. Kuchta, "Biomining – Biotechnological Systems for the Extraction and Recovery of Metals from Secondary Sources," *Global NEST Journal*, 2018. (cited on page 15)

67. R. Ahlefeldt, *Evaluation of a Stoichiometric Rare Earth Crystal for Quantum Computing*. PhD Thesis, The Australian National University, 2013. (cited on page 16)

68. A. J. Freeman and R. E. Watson, "Theoretical Investigation of Some Magnetic and Spectroscopic Properties of Rare-Earth Ions," *Physical Review*, vol. 127, no. 6, pp. 2058–2075, 1962. (cited on page 16)

69. R. W. Equall, R. L. Cone, and R. M. Macfarlane, "Homogeneous broadening and hyperfine structure of optical transitions in Pr^{3+}: Y_2SiO_5," *Physical Review B*, vol. 52, no. 6, p. 3963, 1995. (cited on pages 16, 17, 18, 21, and 22)

70. G. Liu and B. Jacquier, eds., *Spectroscopic Properties of Rare Earths in Optical Materials*. Springer Series in Materials Science, Berlin Heidelberg: Springer-Verlag, 2005. (cited on pages 17, 18, and 20)

71. G. H. Dieke and H. M. Crosswhite, "The Spectra of the Doubly and Triply Ionized Rare Earths," *Applied Optics*, vol. 2, no. 7, p. 675, 1963. (cited on page 18)

72. M. Nilsson, L. Rippe, S. Kroll, R. Klieber, and D. Suter, "Hole-burning techniques for isolation and study of individual hyperfine transitions in inhomogeneously broadened solids demonstrated in Pr^{3+} : Y_2 SiO_5," *Physical Review B*, vol. 70, no. 21, 2004. (cited on pages 18 and 19)

73. K. R. Ferguson, *Generation and Storage of Optical Entanglement in a Solid State Spin-Wave Quantum Memory*. PhD Thesis, The Australian National University, 2016. (cited on pages 19, 34, 37, 38, 42, 43, 44, 48, 50, 54, 61, 65, 75, 76, 85, and 86)

74. S. E. Beavan, P. M. Ledingham, J. J. Longdell, and M. J. Sellars, "Photon echo without a free induction decay in a double-Λ system," *Optics Letters*, vol. 36, no. 7, p. 1272, 2011. (cited on pages 19, 33, and 34)

75. Y. S. Bai and R. Kachru, "Nonequilibrium resonant-phonon-induced excess photon-echo dephasing," *Physical Review B*, vol. 46, no. 21, pp. 13735–13738, 1992. (cited on page 20)

76. S. Kroll, E. Xu, and R. Kachru, "Influence of excited-state Pr^{3+} on the relaxation of the Pr^{3+}:$YAlO_3$ $3H_4$-$1D_2$ transition," *Physical Review. B, Condensed Matter*, vol. 44, no. 1, pp. 30–34, 1991. (cited on page 20)

77. R. M. Macfarlane, D. P. Burum, and R. M. Shelby, "New Determination of the Nuclear Magnetic Moment of Pr 141," *Physical Review Letters*, vol. 49, no. 9, pp. 636–639, 1982. (cited on page 21)

78. K. Holliday, M. Croci, E. Vauthey, and U. P. Wild, "Spectral hole burning and holography in an Pr^{3+} : Y_2 SiO_5 crystal," *Physical Review B*, vol. 47, no. 22, p. 14741, 1993. (cited on pages 21 and 22)

79. F. R. Graf, *Investigations of Spectral Dynamics in Rare Earth Ion Doped Crystals Using High Resolution Laser Techniques*. PhD Thesis, ETH Zurich, 1998. (cited on pages 21, 22, and 23)

80. A. V. Turukhin, V. S. Sudarshanam, M. S. Shahriar, J. A. Musser, B. S. Ham, and P. R. Hemmer, "Observation of Ultraslow and Stored Light Pulses in a Solid," *Physical Review Letters*, vol. 88, no. 2, 2001. (cited on pages 21 and 22)

81. E. Fraval, M. J. Sellars, and J. J. Longdell, "Method of extending hyperfine coherence times in Pr^{3+} : Y_2 SiO_5," *Physical Review Letters*, vol. 92, no. 7, 2004. (cited on page 21)

82. J. J. Longdell, A. L. Alexander, and M. J. Sellars, "Characterization of the hyperfine interaction in europium-doped yttrium orthosilicate and europium chloride hexahydrate," *Physical Review B*, vol. 74, no. 19, 2006. (cited on pages 21 and 22)

83. S. E. Beavan, E. Fraval, M. J. Sellars, and J. J. Longdell, "Demonstration of the reduction of decoherent errors in a solid-state qubit using dynamic decoupling techniques," *Physical Review A*, vol. 80, no. 3, 2009. (cited on page 21)

84. E. Fraval, M. J. Sellars, and J. J. Longdell, "Dynamic Decoherence Control of a Solid-State Nuclear-Quadrupole Qubit," *Physical Review Letters*, vol. 95, no. 3, 2005. (cited on page 21)

85. G. Heinze, C. Hubrich, and T. Halfmann, "Stopped Light and Image Storage by Electromagnetically Induced Transparency up to the Regime of One Minute," *Physical Review Letters*, vol. 111, no. 3, 2013. (cited on pages 21 and 22)

86. F. Konz, Y. Sun, C. W. Thiel, R. L. Cone, R. W. Equall, R. L. Hutcheson, and R. M. Macfarlane, "Temperature and concentration dependence of optical dephasing, spectral-hole lifetime, and anisotropic absorption in Eu^{3+} : Y_2 SiO_5," *Physical Review B*, vol. 68, no. 8, 2003. (cited on page 22)

87. M. P. Hedges, *High Performance Solid State Quantum Memory*. PhD Thesis, The Australian National University, 2011. (cited on pages 22 and 23)

88. N. A. Kurnit, I. D. Abella, and S. R. Hartmann, "Observation of a Photon Echo," *Physical Review Letters*, vol. 13, no. 19, pp. 567–568, 1964. (cited on page 26)

89. T. W. Mossberg, "Time-domain frequency-selective optical data storage," *Optics Letters*, vol. 7, no. 2, pp. 77–79, 1982. (cited on pages 26 and 30)

90. S. A. Moiseev, V. F. Tarasov, and B. S. Ham, "Quantum memory photon echo-like techniques in solids," *Journal of Optics B: Quantum and Semiclassical Optics*, vol. 5, no. 4, pp. S497–S502, 2003. (cited on page 30)

91. J. Ruggiero, J.-L. L. Gouët, C. Simon, and T. Chanelière, "Why the two-pulse photon echo is not a good quantum memory protocol," *Physical Review A*, vol. 79, no. 5, 2009. (cited on page 32)

92. M. C. Berrington, *Extending the Storage Time of a Solid-State Quantum Memory*. Honours Thesis, The Australian National University, 2016. (cited on pages 34 and 55)

93. P. M. Ledingham, W. R. Naylor, and J. J. Longdell, "Experimental Realization of Light with Time-Separated Correlations by Rephasing Amplified Spontaneous Emission," *Physical Review Letters*, vol. 109, no. 9, 2012. (cited on pages 38 and 39)

94. L.-M. Duan, G. Giedke, J. I. Cirac, and P. Zoller, "Inseparability Criterion for Continuous Variable Systems," *PHYSICAL REVIEW LETTERS*, vol. 84, no. 12, p. 4, 2000. (cited on page 41)

95. W. P. Bowen, R. Schnabel, P. K. Lam, and T. C. Ralph, "Experimental investigation of criteria for continuous variable entanglement," *Physical Review Letters*, vol. 90, no. 4, p. 043601, 2003. (cited on page 41)

96. P. M. Ledingham, *Optical Rephasing Techniques with Rare Earth Ion Dopants for Applications in Quantum Information Science*. PhD Thesis, The University of Otago, 2011. (cited on pages 43 and 45)

97. M. J. Sellars, "Ultra-high resolution laser spectroscopy of rare earth doped solids," 1995. (cited on page 55)

98. "Quantum Noise: Basic Measurements and Techniques," in *A Guide to Experiments in Quantum Optics*, pp. 200–231, John Wiley & Sons, Ltd, 2008. (cited on page 58)

99. M. Azadeh, C. Sjaarda Cornish, W. R. Babbitt, and L. Tsang, "Efficient photon echoes in optically thick media," *Physical Review A*, vol. 57, no. 6, pp. 4662–4668, 1998. (cited on page 89)

100. C. S. Cornish, W. R. Babbitt, and L. Tsang, “Demonstration of highly efficient photon echoes,” *Optics Letters*, vol. 25, no. 17, pp. 1276–1278, 2000. (cited on page 89)